

Diese Dissertation haben begutachtet:

.....



DISSERTATION

Stability of nonlocal quantum correlations in neutral B-meson systems

ausgeführt zum Zwecke der Erlangung des akademischen Grades eines
Doktors der technischen Wissenschaften unter der Leitung von

Univ.Doiz. Dipl.-Ing. Dr.techn. Rudolf Frühwirth
Institut für Hochenergiephysik
der österreichischen Akademie der Wissenschaften

eingereicht an der Technischen Universität Wien
bei der Fakultät für Physik

von

Dipl.-Ing. Gerald Richter
Matrikelnummer: 9026078
Mollardgasse 21, 1060 Wien

Wien, im Dezember 2008

Kurzfassung

Die vorliegende Arbeit wurde am Institut für Hochenergiephysik (HEPHY) der Österreichischen Akademie der Wissenschaften im Rahmen der Belle Kollaboration ausgeführt.

Das Belle Experiment am Forschungszentrum KEK (Tsukuba, Japan) wurde konzipiert, um eine bestimmte Teilchenart (B Mesonen) zu erzeugen, und wird daher als “B-Fabrik” bezeichnet. Die primäre Zielsetzung des Experiments ist die Untersuchung der Verletzung einer grundlegenden Symmetrie (der CP-Symmetrie), die für den Überschuß von Materie gegenüber Antimaterie in unserem Universum verantwortlich ist.

Die erzeugten B_d^0 Mesonen sind massive Teilchen und werden in einem sogenannten verschränkten Quantenzustand erzeugt, der ungewöhnliche Eigenschaften zeigt, die nicht immer durch klassische Korrelationen reproduzierbar sind. Diese sogenannten nichtlokalen Phänomene wurden seit dem Beginn der Quantentheorie intensiv theoretisch, philosophisch und experimentell beleuchtet.

Der in der vorliegenden Arbeit untersuchte verschränkte Zustand ist ein Zweiteilchen-System und muss durch eine einzige Wellenfunktion beschrieben werden, die im Kollaps der Wellenfunktion, also wenn der verschränkte Zustand aufgelöst wird, in zwei separate Wellenfunktionen zerfällt. Dieser unstetige Übergang wirft einige Fragen auf, die nicht eindeutig beantwortbar sind.

Ein alternativer erweiternder Ansatz, die *Dekohärenztheorie*, macht diese Übergänge in gewisser Weise stetig, und führt die abnehmende Kohärenz (d.h. die nicht-lokale Korrelation von Erwartungswerten) in dem verschränkten Quantensystem auf die Wechselwirkung des betrachteten Quantensystems mit der umgebenden Umwelt zurück.

Die Zielsetzung der präsentierten Forschungsarbeit ist es, anhand eines massiven Quantensystems von Elementarteilchen, die Haltbarkeit des verschränkten Zustandes in dem sie erzeugt wurden, zu untersuchen. Ein theoretisches Modell der Dekohärenztheorie kommt zur Anwendung, um das

Verhalten des Systems zu beschreiben.

Das erste Kapitel gibt einen kurzen Abriss über den Hintergrund der Arbeit. In Kapitel 2 werden die physikalische Motivation und der theoretische Hintergrund der Forschungsfrage dargestellt. Das dritte Kapitel beschreibt den Aufbau des Belle Experiments. Kapitel 4 gibt eine genaue Darstellung der physikalischen Ereignisrekonstruktion, der Datenselektion und Vertexrekonstruktion. Das fünfte Kapitel beschreibt die sogenannte “Toy Montecarlo”, die zum Test der verwendeten Methoden implementiert wurde, und den Modellparameter Schätzalgorithmus. Kapitel 6 behandelt die Details der Datenrekonstruktion und der Behandlung von Untergrundereignissen. Das siebte Kapitel widmet sich den Resultaten und der Beschreibung der systematischen Fehler. Kapitel 8 gibt schließlich eine Zusammenfassung der erarbeiteten Ergebnisse.

Abstract

The work at hand has been carried out at the Institute of High Energy Physics (HEPHY) of the Austrian Academy of Sciences within the framework of the Belle Collaboration.

The Belle experiment at the KEK research center (Tsukuba, Japan) has been designed to produce a specific kind of particles (B mesons), and is therefore called a “B-factory”. The primary goal of the experiment is the investigation of the violation of a fundamental symmetry (the CP-symmetry), which is responsible for the surplus of matter compared to antimatter in our universe.

The generated B_d^0 mesons are massive particles which are produced in a so-called entangled quantum-state. This state displays unusual properties which are not always reproducible by classical correlations. Since the beginning of quantum theory these so-called nonlocal phenomena have been intensively studied from the theoretical, philosophical and experimental point of view.

The presented thesis investigates this entangled state, which is a two-particle system that must be described by one wave-function. When the entangled state is dissolved in the collapse of the wave-function, two separate wave-functions remain. This discontinuous transition results in some questions which cannot be answered definitely.

An alternative, expanding approach the *decoherence-theory* makes these transitions continuous in some respects. It relates the decreasing coherence (i.e. the non-local correlation of expectation values) in the examined quantum-system to the interactions of the quantum-system with its surrounding environment.

It is the goal of the presented research to study the stability of an entangled state on the basis of a massive quantum-system of elementary particles. A theoretical model of decoherence-theory is being employed to describe the systems behavior.

The first chapter gives a short summary on the background of the work. In

Chapter 2 the physical motivation and the theoretical background is outlined. The third chapter describes the setup of the Belle experiment. Chapter 4 gives a detailed description of the physical event-reconstruction, of the data-selection and the vertex-reconstruction. The fifth chapter covers the so-called “Toy Montecarlo”, which was implemented to test the applied methods. The model-parameter estimation algorithm is also explained. Chapter 6 deals with the details of the data reconstruction, and the treatment of background events. The seventh chapter focuses on the results and the description of systematic errors. Finally, in Chapter 8 a short summary on the achieved results is given.

Thanks

To my dear parents and my grandmother, my tutors and colleagues at the Institute of High Energy Physics (HEPHY) in Vienna. To my friends Peter Negrelli, Marcus Pernkopf, Wolfgang Waltenberger, and last but not least to Julia for support, friendship, help and far more.

The following persons are listed because without their help, failure would have been much closer than success.

Reinhold Bertlmann

Rudolf Frühwirth

Beatrix Hiesmayr

Manfred Jeitler

Winfried Mitaroff

Christoph Schwanda

Laurenz Widhalm

Contents

1	Introduction	1
2	Physics motivation	3
2.1	Some physics of B mesons	3
2.2	Time evolution	6
2.2.1	Beauty oscillation	7
2.2.2	Flavor asymmetry	8
2.3	Decoherence	10
2.3.1	Density matrix formalism	11
2.3.2	A decoherence model master equation	13
2.3.3	Entangled B mesons	14
2.3.4	Measuring decoherence	17
3	The Belle experiment	22
3.1	The KEKB Ring Collider	23
3.2	Description of the Belle Detector	27
3.2.1	Beam pipe	28
3.2.2	Extreme Forward Calorimeter	29
3.2.3	Silicon vertex detector	29
3.2.4	Central Drift Chamber	31
3.2.5	Aerogel Čerenkov Counter	34
3.2.6	Time-of-Flight and Trigger Scintillation Counters	35
3.2.7	Electromagnetic Calorimeter	36
3.2.8	Solenoid magnet	37
3.2.9	K_L and Muon Detector	37

3.3	Data acquisition and Trigger system	39
3.3.1	The L1 trigger	40
3.3.2	The L3 and L4 triggers	42
3.3.3	Data Acquisition	42
3.3.4	Data Processing	43
3.4	Software	44
3.4.1	Monte Carlo Event Generation	44
4	Event reconstruction	46
4.1	Data selection	46
4.2	Particle selection	47
4.3	Full reconstruction side	49
4.4	Partial reconstruction side	50
4.5	Decay time reconstruction	53
4.5.1	Vertex reconstruction	54
4.6	Resolution functions	56
4.6.1	Problem parametrisation	57
4.6.2	Model cuts	57
5	Toy Monte Carlo and fit method	59
5.1	Resolution functions	59
5.2	Event generation	60
5.3	Maximum Likelihood estimation	62
5.3.1	Properties	63
5.3.2	Variance	64
5.3.3	Application	65
5.4	Test set results	66
6	Data analysis	71
6.1	Resolution function modelling	71
6.2	MC event generation	72
6.2.1	EvtGen modifications	74
6.3	Signal components and background influences	75
6.3.1	Continuum background	76

6.3.2	Combinatorial background	78
6.3.3	Leptonic background and signal events	78
6.3.4	Other background	83
7	Results	84
7.1	Signal MC	84
7.2	Data fit result	87
7.3	Systematic errors	88
7.3.1	Fractional component fit	88
7.3.2	Resolution function variation	89
7.3.3	Bias correction	90
7.3.4	Overall systematic error	90
8	Conclusions	91
8.1	Final results	91
8.2	Outlook	92
A	Mathematical details	93
A.1	Decoherence model master equation	93
A.2	Entangled B mesons	94
A.3	EvtGen modifications	95
	Bibliography	97

Chapter 1

Introduction

Since the early days of quantum mechanics the evolution of this theoretical and experimental branch has been accompanied by intense discussions about the interpretation of the scientific evidence and the conceptual curiosities that arise from the confrontation with human's classically trained understanding of the world.

One of the periods that showed the conceptual differences most clearly was when in 1935 Einstein, Podolsky and Rosen (EPR) discussed a gedanken experiment, involving a specially prepared QM system of two particles, and arrived at the conclusion that the description of physical reality given by the quantum wave function cannot be complete. This suggested that there should be some further information hidden in so-called "hidden variables" which were responsible for the peculiar behavior of quantum mechanical systems. Niels Bohr, one of the founders of QM, held the opposite view and defended a strict interpretation, the Copenhagen Interpretation, of QM. This sparked a discussion, that went on for 30 years merely philosophically. For more on this topic see [1, 2].

Especially the concept of entangled quantum states was crucial in all these discussions. So, when in 1964 J.S Bell found a general scheme for testing QM against hidden variable theories, he concluded that a certain inequality which is always satisfied by hidden variable models, can be violated by QM.

The presented thesis is concerned with the detailed study of some funda-

mental quantum mechanical aspects of a massive meson system, namely the B^0 system. Similar studies [3, 4] have been done in another entangled massive particle system (the $K^0\bar{K}^0$ system). These studies had a slightly different focus and were confined by other experimental constraints. Nevertheless, they were in good agreement with QM predictions.

In the course of this study we will rely on the exhibited properties of quantum mechanical entanglement in the B^0 system, thus excluding the description by local realistic theories (LRT) as they have been proposed repeatedly over the time since the first “hidden variable” ideas have been issued by EPR. We will present a theoretical model to quantify decoherence effects, and describe the experimental procedure to verify this model with data provided by the Belle experiment, which is located in Tsukuba, Japan.

As opposed to previous studies on the B^0 system [5], this analysis is taking a further step with respect to the compliance with detailed theoretical proposals for the description of decoherence, and gives an upper boundary on the actual theoretical parameter describing the decoherence, instead of estimating possible decoherence by a phenomenological parameter. The presented study also allows for considering the full theoretical model investigated, without averaging over involved time parameters due to experimental constraints, as has been done in the previous study mentioned above. Its purpose is to pave the way for future studies, that can rely on more precise experimental data, as far as decay-vertex accuracy and therefore time resolutions of entangled B -meson lifetimes is concerned.

Chapter 2

Physics motivation

In the last years there has been increasing interest in using particle physics for the study of basic questions of quantum mechanics, such as possible deviations from the established quantum mechanical description of the microcosm. Quantum entanglement is one of the phenomena that efforts have been concentrated on. Suitable systems for investigations were mostly found in photonic states, and for the last few years in the entangled $K^0\bar{K}^0$ and $B^0\bar{B}^0$ states, being produced in e^+e^- collisions at the resonances Φ and $\Upsilon(4S)$, respectively. The states become macroscopically extended objects before they decay. Furthermore these entangled systems are important objects to test QM against local realistic theories (LRT). A previous study (CPLEAR) [3] has concentrated on these tests against LRT in the kaon system. Similar studies in the B -meson system [6] have been shown to be lacking the consideration of the full hilbert-space, which includes the decay products of the primary mesons [7]. This is due to the rapid decrease in time of the B -meson amplitudes, and the passive character of the flavor measurement.

2.1 Some physics of B mesons

A short summary on the properties of B mesons, especially the flavor characteristics of these particles will be given in the following. The interested reader is referred to more details on this topic in [8].

The particles of the system under consideration are pseudoscalar mesons with $J^{PC} = 1^{--}$. Their respective quark contents are $B_d^0 = (d\bar{b})$ and $\bar{B}_d^0 = (\bar{d}b)$. For the sake of brevity the index d will be dropped furthermore.

The neutral $B^0 - \bar{B}^0$ meson system can be studied under the aspects of two physically reasonable bases, which are accessible to measurements. Since quantum mechanics only provides for a set of rules to make probabilistic statements about the outcome of measurements, it depends on the type of measurement performed in the experiment as to which basis becomes relevant. This is in contrast to photon experiments, where the choice of bases is more arbitrary.

First, there is the basis that is directly observable at a B-factory, e.g. through semi-leptonic decay channels ($B^0 \rightarrow l^+\nu_l X^-$, $\bar{B}^0 \rightarrow l^-\bar{\nu}_l X^+$ with X^\pm being non-beauty states) identifying B^0 or \bar{B}^0 by either a positive or negative high-momentum lepton, respectively; this *flavor basis* with the beauty flavor operator \mathcal{B}

$$\begin{aligned}\mathcal{B}|B^0\rangle &= +|B^0\rangle \\ \mathcal{B}|\bar{B}^0\rangle &= -|\bar{B}^0\rangle\end{aligned}\tag{2.1}$$

defines the *beauty* (or *bottom*) *quantum number*, i.e. $B = +1(-1)$ for $B^0(\bar{B}^0)$. Due to weak interaction box-graphs (fig. 2.1) these mesons exhibit oscillations between the particle and anti-particle states. This is possible because the weak interaction does not conserve the beauty quantum number B , therefore processes with $\Delta B \neq 0$ are possible.

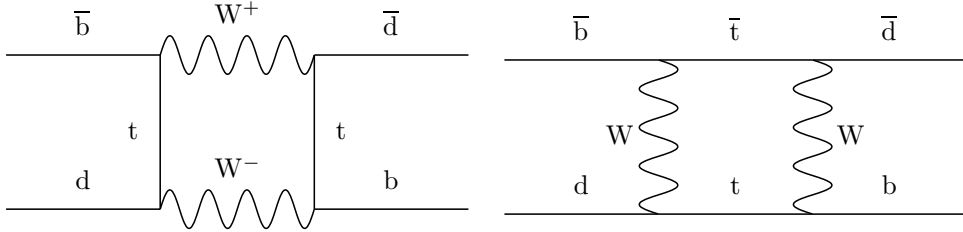


Figure 2.1: Dominant box diagrams for transitions $B_d^0 \rightarrow \bar{B}_d^0$.

These flavor eigenstates B^0 and \bar{B}^0 are related through the \mathcal{CP} transfor-

mation, which will introduce an arbitrary phase $2\xi_B$, which is by convention chosen to be $\xi_B = \pi/2$, yielding

$$\begin{aligned}\mathcal{CP} |B^0\rangle &= e^{2i\xi_B} |\bar{B}^0\rangle = -|\bar{B}^0\rangle \\ \mathcal{CP} |\bar{B}^0\rangle &= e^{-2i\xi_B} |B^0\rangle = -|B^0\rangle\end{aligned}\tag{2.2}$$

From this it follows that the linear combinations

$$\begin{aligned}|B_1^0\rangle &= \frac{1}{\sqrt{2}}(|B^0\rangle - |\bar{B}^0\rangle) \\ |B_2^0\rangle &= \frac{1}{\sqrt{2}}(|B^0\rangle + |\bar{B}^0\rangle)\end{aligned}\tag{2.3}$$

are the \mathcal{CP} eigenstates

$$\begin{aligned}\mathcal{CP} |B_1^0\rangle &= +|B_1^0\rangle \\ \mathcal{CP} |B_2^0\rangle &= -|B_2^0\rangle\end{aligned}$$

which can be observed via the decay products of e.g. $B \longrightarrow J/\Psi K_S^0$, and cannot be a flavor eigenstate because B^0 as well as \bar{B}^0 can decay to these same products.

If \mathcal{CP} were conserved, then $|B_1^0\rangle$ and $|B_2^0\rangle$ would also be mass eigenstates. Since this is not the case, in the *mass eigenbasis*, the two states (light and heavy mass) are given by the ansatz¹

$$\begin{aligned}|B_L\rangle &= p|B^0\rangle + q|\bar{B}^0\rangle \\ |B_H\rangle &= p|B^0\rangle - q|\bar{B}^0\rangle\end{aligned}\tag{2.4}$$

with complex coefficients p and q obeying the normalization condition $|p|^2 + |q|^2 = 1$.

¹Note that $|B_L\rangle$ and $|B_H\rangle$ are not orthogonal states, i.e. $\langle B_L|B_H\rangle \neq 0$.

2.2 Time evolution

The time evolution of the two-state B-meson system is best described by using the notion of an effective Hamiltonian. A generalized formulation of this approach can be found in [9]. Thus, the evolution of an arbitrary linear combination of the flavor eigenstates

$$a|B^0\rangle + b|\bar{B}^0\rangle \quad (2.5)$$

is governed by an effective Schrödinger equation. A special approximation (the Wigner-Weisskopf approximation) [10] allows to approximate the effective Hamiltonian by

$$i\frac{d}{dt}\begin{pmatrix} a \\ b \end{pmatrix} = H\begin{pmatrix} a \\ b \end{pmatrix} \equiv (M - \frac{i}{2}\Gamma)\begin{pmatrix} a \\ b \end{pmatrix} \quad (2.6)$$

Here M and Γ are Hermitian matrices, from which it follows that M_{ii}, Γ_{ii} are real, and $M_{21} = M_{12}^*$ and $\Gamma_{21} = \Gamma_{12}^*$. $\mathcal{CP}\mathcal{T}$ invariance ensures $H_{11} = H_{22}$, implying $M_{11} = M_{22}$, i.e. the masses of both flavor eigenstates are the same, and $\Gamma_{11} = \Gamma_{22}$, i.e. also their widths are the same. Diagonalization of $H \equiv (M - \frac{i}{2}\Gamma)$ yields the two mass eigenvalues of $|B_L\rangle$ and $|B_H\rangle$, denoted M_L and M_H and their widths Γ_L and Γ_H .

Therefore we arrive at a simple exponential evolution in time for the heavy and light mass eigenstates:²

$$\begin{aligned} |B_L(t)\rangle &= e^{-i\lambda_L t} |B_L(0)\rangle \\ |B_H(t)\rangle &= e^{-i\lambda_H t} |B_H(0)\rangle \end{aligned} \quad (2.7)$$

with the exponential parameters being the eigenvalues of H given by

$$\lambda_{H,L} = M_{H,L} - \frac{i}{2}\Gamma_{H,L} \quad (2.8)$$

²Although the situation is slightly different with kaons, these are the equivalents to the K_S^0 and K_L^0 states in the kaon system, where the mass difference Δm is very small and the lifetime difference $\Delta\Gamma$ rather big.

2.2.1 Beauty oscillation

For an initially pure $|B^0\rangle$ beam the time evolution can be obtained by inverting eqns. (2.4) and inserting eqn. (2.7), so with the definition

$$g_{\pm}(t) = e^{-i\lambda_L t} \pm e^{-i\lambda_H t} \quad (2.9)$$

we get

$$\begin{aligned} |B^0(t)\rangle &= \frac{1}{2p} [e^{-i\lambda_L t} |B_L(0)\rangle + e^{-i\lambda_H t} |B_H(0)\rangle] \\ &= \frac{1}{2p} [g_+(t)p |B^0\rangle + g_-(t)q |\bar{B}^0\rangle] \end{aligned} \quad (2.10)$$

Similarly for an antiparticle $|\bar{B}^0\rangle$ beam:

$$\begin{aligned} |\bar{B}^0(t)\rangle &= \frac{1}{2q} [e^{-i\lambda_L t} |B_L(0)\rangle - e^{-i\lambda_H t} |B_H(0)\rangle] \\ &= \frac{1}{2q} [g_-(t)p |B^0\rangle + g_+(t)q |\bar{B}^0\rangle] \end{aligned} \quad (2.11)$$

The next question is: what happens if we suppose we produce a pure B^0 beam, and ask for the probability to detect a B^0 at some later time t :

$$\begin{aligned} P(B^0 \longrightarrow B^0(t)) &\equiv |\langle B^0 | B^0(t) \rangle|^2 = \left| \frac{1}{2} g_+(t) \right|^2 \\ &= \frac{1}{4} [e^{-\Gamma_L t} + e^{-\Gamma_H t} + 2\mathcal{R}e(e^{i\Delta m t})e^{-\Gamma t}] \\ &= \frac{1}{4} [e^{-\Gamma_L t} + e^{-\Gamma_H t} + 2\cos(\Delta m t)e^{-\Gamma t}] \end{aligned} \quad (2.12)$$

where $\Gamma \equiv \frac{1}{2}(\Gamma_H + \Gamma_L)$ is the mean width of the two mass eigenstates.

Inversely, for the probability to find a \bar{B}^0 at some time t from an initial B^0 , we derive:

$$\begin{aligned} P(B^0 \longrightarrow \bar{B}^0(t)) &\equiv |\langle B^0 | \bar{B}^0(t) \rangle|^2 = \left| \frac{p}{2q} g_-(t) \right|^2 \\ &= \frac{|p|^2}{4|q|^2} [e^{-\Gamma_L t} + e^{-\Gamma_H t} - 2\cos(\Delta m t)e^{-\Gamma t}] \end{aligned} \quad (2.13)$$

After carrying out similar calculations for an initial \bar{B}^0 state, we arrive at the following equations:

$$P(B^0 \longrightarrow B^0(t)) = \frac{1}{4}[A + B] \quad (2.14)$$

$$P(B^0 \longrightarrow \bar{B}^0(t)) = \frac{1}{4} \frac{|p|^2}{|q|^2} [A - B] \quad (2.15)$$

$$P(\bar{B}^0 \longrightarrow \bar{B}^0(t)) = \frac{1}{4}[A + B] \quad (2.16)$$

$$P(\bar{B}^0 \longrightarrow B^0(t)) = \frac{1}{4} \frac{|q|^2}{|p|^2} [A - B] \quad (2.17)$$

with the abbreviations

$$A \equiv e^{-\Gamma_L t} + e^{-\Gamma_H t} \quad (2.18)$$

$$B \equiv 2 \cos(\Delta m t) e^{-\Gamma t}$$

2.2.2 Flavor asymmetry

We will neglect CP violation, since it is a rather small effect, the CP violation parameter

$$1 - \left| \frac{q}{p} \right|^2 \simeq \Im \left(\frac{\Gamma_{12}}{M_{12}} \right)$$

is expected to be $\approx \mathcal{O}(10^{-3})$ for the $B^0 \bar{B}^0$ system. Therefor we set $|q/p| = 1$, which lets us calculate an asymmetry of transition probabilities between same flavor (SF) and opposite flavor (OF) states for the single particle time evolutions:

$$A(t) \equiv \frac{SF - OF}{SF + OF} = \frac{\cos(\Delta m t)}{\cosh(\frac{\Delta \Gamma}{2} t)} = P_{SF} - P_{OF} \quad (2.19)$$

where we have defined the probabilities normalized in time as:

$$P_{SF} = \frac{SF}{SF + OF} \quad (2.20)$$

$$P_{OF} = \frac{OF}{SF + OF}$$

with

$$SF \equiv P(B^0 \longrightarrow B^0(t)) + P(\bar{B}^0 \longrightarrow \bar{B}^0(t))$$

$$OF \equiv P(B^0 \longrightarrow \bar{B}^0(t)) + P(\bar{B}^0 \longrightarrow B^0(t))$$

In equation (2.19) we have used the notations $\Delta\Gamma = \Gamma_H - \Gamma_L$ and $\Delta m = m_H - m_L$ and also set the very small value $\Delta\Gamma \approx 0$. This asymmetry has the advantage, that any decay time effects are cancelled out, so that the probabilities (2.20) to find the appropriate flavor correlations can be clearly seen as in figure 2.2.

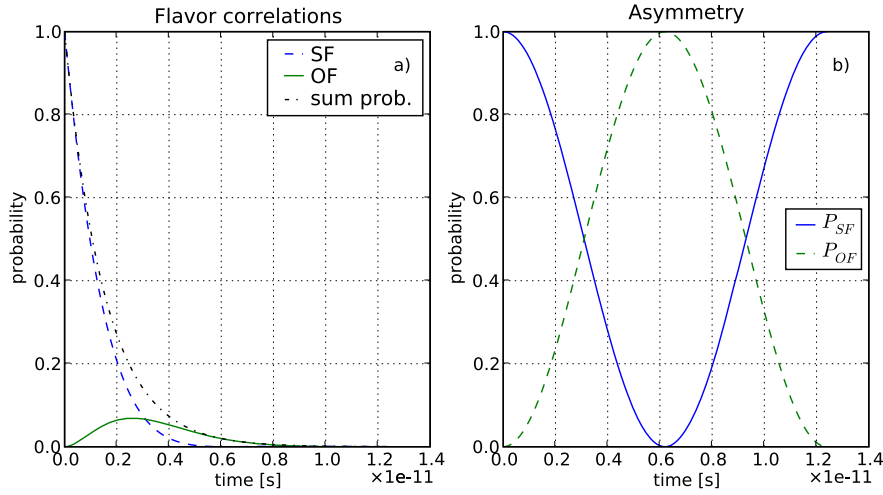


Figure 2.2: a) Single particle probabilities to find a B meson of the same (opposite) flavor in an initial beam of B^0 or \bar{B}^0 . The red line shows the exponential decay rate of the single particles, which dampens the absolute rate of particles to find. Due to this damping term, only about half a period of the flavor oscillation is visible. b) The probabilities here are not influenced by this decay rate because the components of the asymmetry term of expression (2.19) are shown.

2.3 Decoherence

Let us now consider the creation of an entangled 2-particle B meson state at the $\Upsilon(4S)$ resonance. Without premature decoherence, this entangled state will propagate until the first of the two mesons decays (fig. 2.3).

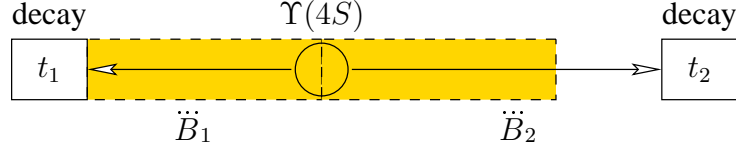


Figure 2.3: Exemplary decay of an $\Upsilon(4S)$ resonance into a $B^0 \bar{B}^0$ meson pair in the center of momentum system. The yellow box shows the region $t < t_1$ where none of the mesons has decayed and hence the entanglement is sustained. The \ddot{B}_1 and \ddot{B}_2 are the two flavor oscillating 1-meson subsystems, which the whole 2-particle system is composed of.

The entanglement arises from the specific features of the particles involved in the decay, so that the initial quantum number $B = 0$. Since the transition from $\Upsilon(4S) \rightarrow B^0 \bar{B}^0$ involves the strong interaction, which conserves the B quantum number, it results in a B -flavor anticorrelated pair of mesons to be produced. The described process (see figure 2.4) is also known as a “hadronisation process”.

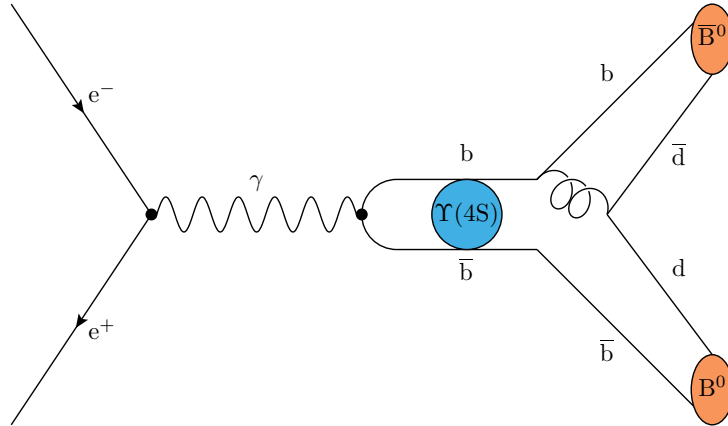


Figure 2.4: The transition $e^+ e^- \rightarrow \gamma \rightarrow \Upsilon(4S) \rightarrow B^0 \bar{B}^0$ in detail. The so called hadronisation takes place via gluon exchange.

We want to describe and measure possible premature decoherence in the

entangled state; decoherence will provide us with some information on the “quality” of the entanglement.

The concept of decoherence, which initially goes back to Furry and Schrödinger [11, 12] who have worked on first ideas of the so called “spontaneous factorization”, has come to be studied in detail again only in the last two decades. It is therefore one of the most recent, consistent interpretations of the seemingly paradox behavior of quantum mechanical systems, when considering the transition from the microscopic (quantum) scale to the macroscopic (classical) world of our everyday experience. This interpretation does not require any sudden changes in the state of the quantum system under consideration, as it is the case with the Copenhagen interpretation (Bohr and Heisenberg) and its consequential collapse of the wave-function. Instead, it allows to understand classicality as emergent from within the quantum formalism. Despite its achievements, this model can not explain the realization of certain final states.

We can consider possible decoherence effects caused by some arbitrary interaction of the quantum system with its environment. Plausible sources for such effects might be strong interaction scatterings of B mesons with nucleons and the experimental noise in the setup. Other more exotic explanations for those effects involve fundamental modifications of QM and can be attributed to the influence of quantum gravity or to dynamical state reduction theories, and arise on a different energy scale. A specific model of decoherence is presented in the following [13], which will allow us to quantify the strength of such possible effects with the help of existing experimental data.

2.3.1 Density matrix formalism

We use a convenient formalism to describe the phenomena which are a manifestation of decoherence theory. Since a statistical mixture of quantum states will occur, the density matrix formalism (which is a core part of quantum statistics) will be applied. A short introduction which is also summarized in [14] is presented below.

In general a quantum system is described by a state vector $|\psi\rangle$ whose

time evolution is determined by the Schrödinger equation³

$$i\frac{\partial}{\partial t}|\psi\rangle = H|\psi\rangle \quad (2.21)$$

The expectation value of an observable A in the state $|\psi\rangle$ is calculated by its matrix element

$$\langle A \rangle = \langle \psi | A | \psi \rangle \quad (2.22)$$

We can now define a *density matrix for pure states* by

$$\rho = |\psi\rangle \langle \psi| \quad (2.23)$$

with the properties

$$\rho^2 = \rho \quad \rho^\dagger = \rho \quad \text{tr } \rho = 1 \quad (2.24)$$

The extension to a statistical mixture of states with probabilities p_i (i.e. the *density matrix for mixed states*) follows as

$$\rho = \sum_i p_i |\psi_i\rangle \langle \psi_i| \quad \text{with} \quad p_i \geq 0, \quad \sum_i p_i = 1 \quad (2.25)$$

This mixed state matrix has the properties

$$\rho^2 \neq \rho \quad \rho^\dagger = \rho \quad \text{tr } \rho = 1 \quad (2.26)$$

As we can see, the properties of unit trace and hermiticity are still preserved, only the first equality is not valid anymore.

We can also introduce some kind of a measure for the “mixedness” of a state $\delta = \text{tr } \rho^2 \leq 1$, where equality holds only for a pure state.

Consequently, the expectation value of an observable A in the mixed state

³The units are chosen such that $c \equiv 1$, $\hbar \equiv 1$. (dimensionless)

defined by ρ is given as

$$\langle A \rangle = \text{tr } \rho A \quad (2.27)$$

Regarding the Schrödinger equation, the time evolution of the density matrix ρ is determined by the *von Neumann equation*

$$\frac{\partial}{\partial t} \rho = -i [H, \rho] \quad (2.28)$$

which basically is the equivalent to the Schrödinger equation in the density matrix formalism.

2.3.2 A decoherence model master equation

We will follow the line of arguments in [13] and [15], and first study the model of decoherence in a 2-dimensional Hilbert space $\mathcal{H} = \mathbb{C}^2$. Allowing for a non-hermitian hamiltonian H will include the possibility of the decay following the approximated hamiltonian (2.6) mentioned before. As above, we assume normalized energy eigenstates $|e_j\rangle$ ($j = 1, 2$) and get

$$H |e_j\rangle = \lambda_j |e_j\rangle \quad \text{with} \quad \lambda_j = m_j - \frac{i}{2} \Gamma_j \quad (2.29)$$

where both m_j and Γ_j are real positive numbers. Also, despite the non-hermiticity of H , we make the assumption of orthogonal eigenstates, i.e. $\langle e_1 | e_2 \rangle = 0$.

Now including decoherence by adding a so called *dissipator* $D[\rho]$, the time evolution of the density matrix becomes a modified form of the von Neumann equation (2.28), and is governed by the following *master equation*

$$\frac{\partial}{\partial t} \rho = -iH\rho + i\rho H^\dagger - D[\rho] \quad (2.30)$$

The investigated model of decoherence [13] consists in assuming that⁴

$$D[\rho] = \lambda(P_1\rho P_2 + P_2\rho P_1), \quad \text{where} \quad P_j = |e_j\rangle\langle e_j| \quad (2.31)$$

are projection operators and λ being a positive constant. The ansatz (2.31) ensures the conservation of energy in case of a Hermitian Hamiltonian since $[P_j, H] = 0$.

With the choice in (2.31) the equations for the elements of ρ decouple. Thus, we split up the density matrix into its components

$$\rho = \sum_{j,k=1}^2 \rho_{jk} |e_j\rangle\langle e_k| \quad (2.32)$$

where $\rho_{jk} = \rho_{kj}^*$. With the von Neumann equation including decoherence (2.30), one obtains (see appendix A.1) the time evolutions of the density matrix elements

$$\begin{aligned} \rho_{11}(t) &= \rho_{11}(0) e^{-\Gamma_1 t} \\ \rho_{22}(t) &= \rho_{22}(0) e^{-\Gamma_2 t} \\ \rho_{12}(t) &= \rho_{12}(0) e^{-i\Delta m t - \Gamma t} e^{-\lambda t} \end{aligned} \quad (2.33)$$

with $\Delta m \equiv m_1 - m_2$, and $\Gamma \equiv (\Gamma_1 + \Gamma_2)/2$.

2.3.3 Entangled B mesons

If one considers two noninteracting systems with Hilbert spaces \mathcal{H}_1 and \mathcal{H}_2 , the Hilbert space of the composite system is given by the tensor product

$$\mathcal{H}_1 \otimes \mathcal{H}_2$$

⁴This decoherence term is of the Lindblad type [16, 17] and generates a completely positive map.

When the first system is in state $|i\rangle_1$ and the second system in state $|j\rangle_2$, the state of the composite system is written as

$$|i\rangle_1 \otimes |j\rangle_2 = |i\rangle_1 |j\rangle_2 = |i \otimes j\rangle = |ij\rangle$$

States of the composite system which can be represented in this form are called *separable states*, or *product states*. If a state is not separable it is called an *entangled state*. For fixed basis sets $\{|k\rangle_1\}$ and $\{|l\rangle_2\}$ a pure state of the composite system $\mathcal{H}_1 \otimes \mathcal{H}_2$ can be written as:

$$|\Psi\rangle = \sum_{k,l} c_{kl} |k\rangle_1 \otimes |l\rangle_2 \quad (2.34)$$

Determining the separability of a system in general is a complex task. More on the various criteria of separability can be found in [18].

We now want to apply our model of decoherence to the case of the 2-particle $B^0 \bar{B}^0$ state, which is generated in the decay of the $\Upsilon(4S)$ resonance. Considering t as the eigentime of B^0 and \bar{B}^0 , we make the following identification for our eigenstate basis:

$$|e_1\rangle = |B_H \otimes B_L\rangle \quad \text{and} \quad |e_2\rangle = |B_L \otimes B_H\rangle \quad (2.35)$$

This choice now defines states where one subsystem (1) is in a certain mass eigenstate, while the other subsystem (2) is in the “opposite” mass eigenstate. For the sake of clarity one can identify those two subsystems with the two sides (left and right) in figure 2.3. The heavy and light states (B_H and B_L , respectively) are defined in eqn. (2.4), with their respective mass eigenvalues of the 1-particle Hamiltonian H_{single} as found in eqn. (2.8).

Now, for the 2-particle system one can transfer the 1-particle Hamiltonian H_{single} to the tensor product of the 1-particle Hilbert spaces, using $H = H_{single} \otimes \mathbf{1}_2 + \mathbf{1}_1 \otimes H_{single}$. The operators $\mathbf{1}_1$ and $\mathbf{1}_2$ are identity operators on the respective subsystem. As visualised in figure 2.3, the first term now shall correspond to the particle on the left, whereas the second term of the tensor product corresponds to the particle on the right.

Again assuming CP conservation in the mixing of $B^0 - \bar{B}^0$ implies $|p/q| = 1$, and we have $\langle B_H | B_L \rangle = 0$, therefore $\langle e_1 | e_2 \rangle = 0$, thus we may set $p = q = 1/\sqrt{2}$.

After having chosen a basis to describe the problem at hand, we start with the state that is generated in the experimental setup. At $t = 0$, an entangled state (which is called “Bell singlet state” for historical reasons) is produced

$$|\psi\rangle = \frac{1}{\sqrt{2}}(|e_1\rangle - |e_2\rangle) \quad (2.36)$$

In the picture of eqn. (2.34) with basis states $\{|k\rangle_1\} = \{|l\rangle_2\} = \{B_L, B_H\}$ this is corresponding to a coefficient matrix of

$$(c_{kl}) = \begin{pmatrix} 0 & -1 \\ 1 & 0 \end{pmatrix}$$

The entangled state is equivalently described by the density matrix

$$\rho(0) = \frac{1}{2}\{|e_1\rangle\langle e_1| + |e_2\rangle\langle e_2| - |e_1\rangle\langle e_2| - |e_2\rangle\langle e_1|\} \quad (2.37)$$

Which in our compact basis choice $\{|e_1\rangle, |e_2\rangle\}$ has the form

$$\rho(0) = \frac{1}{2} \begin{pmatrix} 1 & -1 \\ -1 & 1 \end{pmatrix}$$

Applying the 2-particle Hamiltonian to the chosen eigenstates of the system (2.35) will lead to the same eigenvalue for both solutions $\lambda_1 = \lambda_2 = m - i\Gamma$, where $\Gamma \equiv (\Gamma_H + \Gamma_L)/2$ and $m \equiv m_H + m_L$. Using the same approach and a very similar derivation as for (2.33) (see appn. A.2), gives the resulting time dependent density matrix

$$\rho(t) = \frac{1}{2}e^{-2\Gamma t}\{|e_1\rangle\langle e_1| + |e_2\rangle\langle e_2| - e^{-\lambda t}(|e_1\rangle\langle e_2| + |e_2\rangle\langle e_1|)\} \quad (2.38)$$

which can again be written in the matrix form

$$\rho(t) = \frac{1}{2}e^{-2\Gamma t} \begin{pmatrix} 1 & -e^{-\lambda t} \\ -e^{-\lambda t} & 1 \end{pmatrix}$$

The exponential factor $e^{-\lambda t}$ in the density matrix (2.38) introduces decoherence in consequence of the dissipative term in the extended time evolution of (2.30). Then, for $t > 0$ and $\lambda > 0$, (2.38) is not the density matrix of a pure state anymore. Note, that the choice (2.35) of the energy eigenstates confines the Hilbert space to a 2-dimensional one.⁵

2.3.4 Measuring decoherence

We will now again look at a composite system made up of systems A and B , with their Hilbert space being defined by $\mathcal{H}_A \otimes \mathcal{H}_B$.

Given the density matrix of the whole system to be defined by

$$\rho^{AB} = \rho^A \otimes \rho^B \quad (2.39)$$

and we are to describe the state of the subsystem A , we have to use the so called *reduced density operator* for subsystem A :

$$\rho^A \equiv \text{tr}_B(\rho^{AB}) = \text{tr}_B(\rho^A \otimes \rho^B) = \rho^A \text{tr}(\rho^B)$$

where tr_B is known as the *partial trace* over the subsystem B . The partial trace is defined by

$$\text{tr}_B(|a_1\rangle \langle a_2| \otimes |b_1\rangle \langle b_2|) \equiv |a_1\rangle \langle a_2| \text{tr}(|b_1\rangle \langle b_2|)$$

Here $|a_1\rangle$ and $|a_2\rangle$ are any two vectors in the state space of A , and $|b_1\rangle$ and $|b_2\rangle$ are any two vectors in the state space of B . The trace operation above has the usual meaning of $\text{tr}(|b_1\rangle \langle b_2|) = \langle b_2|b_1\rangle$.

Although it is not obvious that the reduced density operator for system

⁵Using projector states that are not linear combinations of (2.35) in general requires time evolution into the full 4-dimensional Hilbert space of states.

A is a description for the state of system A , it fulfills certain requirements: It provides correct measurement statistics for measurements on system A , and it contains all the physical information available to us. Also, it can be shown, that the partial trace function is the unique function to have the required properties [19].

In order to obtain information about the decoherence parameter λ (which modifies the $B^0\bar{B}^0$ system's time evolution), some assumptions are required. Starting with the density matrix (2.37), this 2-particle state follows the time evolution given in eqn. (2.38). Consequently some decoherence will occur. Referring to fig. 2.3 a measurement of the B quantum number at the time t_1 for the left moving particle, and at the time t_2 for the right moving particle is assumed. In the time window $\min(t_1, t_2) < t < \max(t_1, t_2)$ (i.e. outside the dashed box) only a 1-particle state remains, which is expected to evolve according to QM, as it is given by H_{single} alone. For the sake of definiteness, and without loss of generality we will assume $t_1 \leq t_2$.

Mathematically, we use the projectors $|n\rangle\langle n|$ with $n = \{1, 2\}$ and the definitions $|1\rangle = |B^0\rangle$, $|2\rangle = |\bar{B}^0\rangle$, in the partial trace over the 2-particle system to derive the density matrix for the system at the time of the first decay, i.e. at $t = t_1$:

$$\text{Tr}_1\{|n\rangle\langle n| \otimes \mathbf{1}_2\} \rho(t_1) \equiv \rho_2(t_1|t_1) \quad (2.40)$$

Here we define $\rho_2(t_1|t_1)$ as the 1-particle density matrix for the right moving particle B_2 , after the measurement of the beauty content of the left moving particle B_1 just decayed. For $t > t_1$, which is denoted by $\rho_2(t|t_1)$ it follows the 1-particle time evolution.

At the time of the second decay $t = t_2$, we measure the B quantum number of the second subsystem particle (right moving), and using a new projector $|n'\rangle\langle n'|$ get for $n' = \{1, 2\}$ the expression for the probability

$$P(n, t_1; n', t_2) = \text{Tr}\{|n'\rangle\langle n'| \rho_2(t_2|t_1)\} \quad (2.41)$$

This results in the following terms for the same flavor (SF) and opposite

flavor (OF) probabilities:

$$SF : \quad P(B^0, t_1; B^0, t_2) = P(\bar{B}^0, t_1; \bar{B}^0, t_2) = \quad (2.42)$$

$$\frac{1}{4} \{ e^{-\Gamma_L t_1 - \Gamma_H t_2} + e^{-\Gamma_H t_1 - \Gamma_L t_2} - e^{-\lambda t_1} 2 \cos(\Delta m \Delta t) e^{-\Gamma(t_1 + t_2)} \}$$

$$OF : \quad P(B^0, t_1; \bar{B}^0, t_2) = P(\bar{B}^0, t_1; B^0, t_2) = \quad (2.43)$$

$$\frac{1}{4} \{ e^{-\Gamma_L t_1 - \Gamma_H t_2} + e^{-\Gamma_H t_1 - \Gamma_L t_2} + e^{-\lambda t_1} 2 \cos(\Delta m \Delta t) e^{-\Gamma(t_1 + t_2)} \}$$

Consequently the asymmetry term now yields (compare with eqn. (2.19))

$$A^\lambda(t_1, t_2) = \frac{\cos(\Delta m \Delta t)}{\cosh(\frac{\Delta \Gamma}{2} \Delta t)} \cdot e^{-\lambda t_1} \quad (2.44)$$

with $\Delta t = t_2 - t_1$. We now relax the assumption $t_1 \leq t_2$. Since the decoherence term depends only on the first decay time, and because of time symmetry considerations for the case that $t_2 < t_1$ we can use the minimum function in eqn. (2.44), thus writing

$$A^\lambda(t_1, t_2) = A^{QM}(\Delta t) \cdot e^{-\lambda \cdot \min(t_1, t_2)} \quad (2.45)$$

Also we can see that the parameter dependent asymmetry becomes the standard QM expression for a parameter of $\lambda \rightarrow 0$.

For the case of the two meson system the asymmetry term is defined by

$$A^{QM}(\Delta t) \equiv \frac{OF - SF}{OF + SF} = P_{OF}(t_1, t_2) - P_{SF}(t_1, t_2) = \cos(\Delta m \Delta t) \quad (2.46)$$

where we split the asymmetry for the complete set of events into the sum of probabilities for same and opposite flavor events. The difference $\Delta \Gamma$ has been measured compatible with zero, therefore $\cosh(\frac{\Delta \Gamma}{2} \Delta t) \approx 1$.

Deriving probabilities for the extended decoherence model leads to the

following expressions ($P_{OF} + P_{SF} = 1$):

$$\begin{aligned} P_{OF}(t_1, t_2, \lambda) &= \frac{1}{2}(1 + \cos(\Delta m \Delta t) \cdot e^{-\lambda \cdot \min(t_1, t_2)}) \\ P_{SF}(t_1, t_2, \lambda) &= \frac{1}{2}(1 - \cos(\Delta m \Delta t) \cdot e^{-\lambda \cdot \min(t_1, t_2)}) \end{aligned} \quad (2.47)$$

These probability distributions are also visualized in figure 2.5.

When correcting for the decay of the particles under consideration by multiplying the probabilities with exponential decay terms for both time parameters, one arrives at the following expressions for the probabilities to be expected:

$$\begin{aligned} p_{OF}(t_1, t_2, \lambda) &= \frac{1}{2}(1 + \cos(\Delta m \Delta t) \cdot e^{-\lambda \cdot \min(t_1, t_2)}) \cdot e^{-\Gamma(t_1 + t_2)} \\ p_{SF}(t_1, t_2, \lambda) &= \frac{1}{2}(1 - \cos(\Delta m \Delta t) \cdot e^{-\lambda \cdot \min(t_1, t_2)}) \cdot e^{-\Gamma(t_1 + t_2)} \end{aligned} \quad (2.48)$$

Due to the additional exponential terms the probability distribution functions are restricted to an even smaller range around $(t_1, t_2) = (0, 0)$, so that the features of those distributions become even harder to discriminate. Defining $\Delta t \equiv t_2 - t_1$ allows us to reparametrize these equations in $(t_1, \Delta t)$, since they will be needed later on.

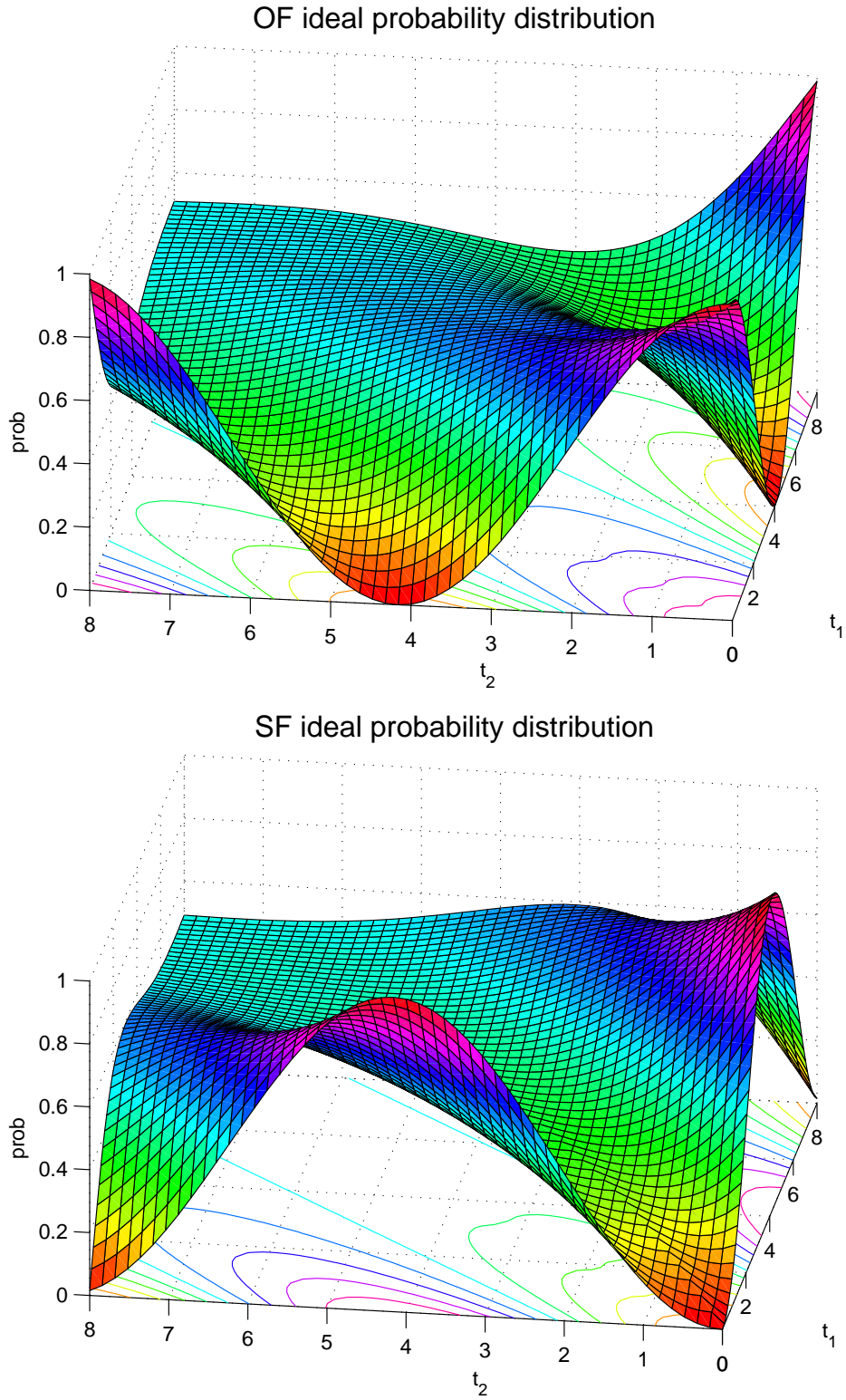


Figure 2.5: Ideal probability densities for non-decaying particles in parametrization (t_1, t_2) . The decoherence model parameter is set to $\lambda = 0.5$.

Chapter 3

The Belle experiment

The overall design of the Belle experiment was made with the specific aim of searching for and studying CP violation in systems of $B\bar{B}$ meson pairs. Therefore the detector is positioned around the collision point of electron and positron beams of the “B-factory” KEKB in Tsukuba, Japan, which features a high luminosity $\mathcal{L} \geq 10^{34} \text{ cm}^{-2} \text{ s}^{-1}$. The physics potential of the experiment strongly depends upon the amount of data collected. While CP violation investigations were successful already at integrated luminosities of about 10 fb^{-1} , other experimental challenges require a large number of B -meson decays ($\sim 10^8$), equalling an integrated luminosity of about 100 fb^{-1} . The current value of this integrated luminosity is about 800 fb^{-1} , as of June 2008.

B_d^0 -mesons are rather heavy particles with a mass of $5.28 \text{ GeV}/c^2$, about five times the mass of the proton. KEKB operates at the center-of-mass energy of the $\Upsilon(4S)$ resonance, which allows production of a $B^0\bar{B}^0$ pair at threshold. This is advantageous for physics analysis because no additional tracks are produced at the primary interaction point, thus causing a very low background from the primary interaction. This background would be disturbing especially for the task of flavor tagging, which most physics analyses rely on.

The Υ mesons are bound states of $b\bar{b}$ quarks with spin, parity and charge conjugation quantum numbers $J^{PC} = 1^{--}$. In figure 3.1 the annihilation cross section over the center-of-mass energy (\sqrt{s}) in the region of the Υ

resonances (ground state 1S, and radial excitations 2S, 3S, 4S, ...) can be seen. The mass of the $\Upsilon(4S)$ meson (10.58 GeV) is just above the threshold for decays into $B_d^0 \bar{B}_d^0$ or $B^+ B^-$ meson pairs. The branching fraction for those $B\bar{B}$ pairs is about 96%. At the $\Upsilon(4S)$, about 1/4 of the hadronic cross-section are $e^+ e^- \rightarrow \Upsilon(4S) \rightarrow B\bar{B}$. All other hadronic production ($e^+ e^- \rightarrow q\bar{q}$ ($q = u, d, s, c$)) is referred to as “continuum”. This continuum, although produced with a significant boost factor due to the low invariant mass, constitutes a major source of background to B physics. In contrast, the $B\bar{B}$ pair is generated nearly at rest in the center of mass system, and has a more spherical event structure. This can be used to suppress continuum events with so called “shape variables”. To be able to study the continuum contributions in “clean” conditions, about 10% of the data are taken 60 MeV below the $\Upsilon(4S)$ resonance energy. That data is labeled as “off-resonance” in contrast to “on-resonance”. Measurements of the production rates of $\Upsilon(4S) \rightarrow B^+ B^-$ vs. $\Upsilon(4S) \rightarrow B_d^0 \bar{B}_d^0$ show equality within the errors.

3.1 The KEKB Ring Collider

Figure 3.2 shows the layout of the collider facility and its rings, with an overall circumference of about 3 km. The energies for the beams were chosen asymmetrically, with the e^- beam at $E_1 = 8$ GeV (high energy ring – HER), and the e^+ beam at $E_2 = 3.5$ GeV (low energy ring – LER), obeying $\sqrt{s} \approx 2\sqrt{E_1 E_2} = m_{\Upsilon(4S)} = 10.58$ GeV in the high relativistic limit, where the rest mass is neglected. This has the advantage of causing a Lorentz boost $\beta\gamma = 0.425$ w.r.t. the laboratory system. Therefore, the reaction products ($B\bar{B}$) have a resulting momentum along the beam direction, thus making it possible to distinguish their decay vertices. The crossing angle of the electron and positron beams in the interaction region is 22 mrad w.r.t. the z -axis.

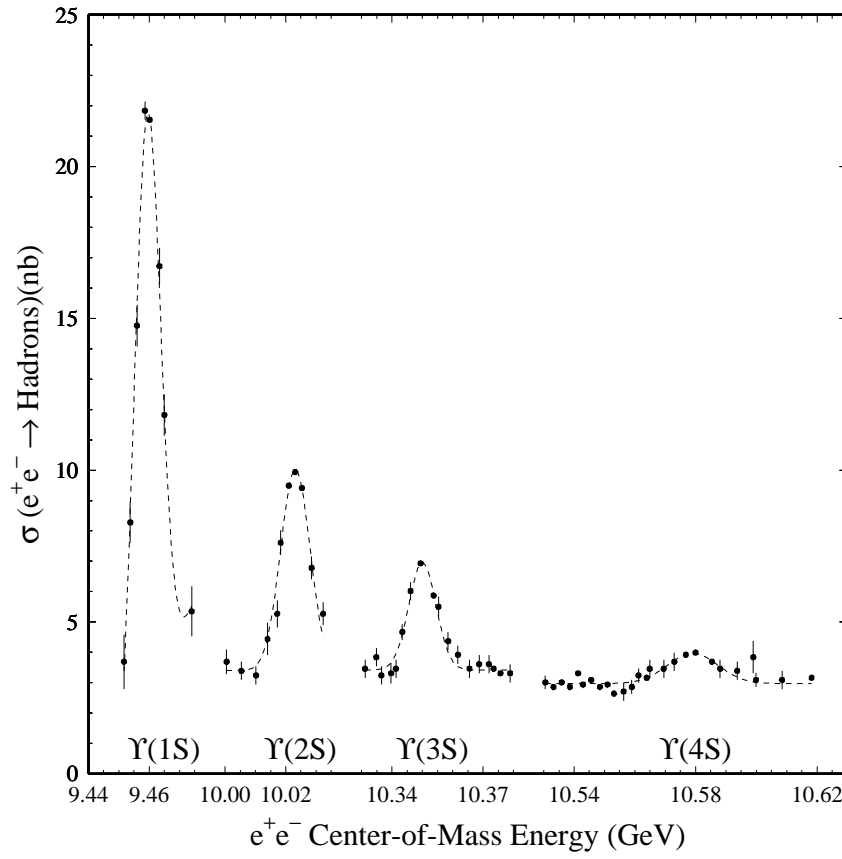


Figure 3.1: Electron positron total hadronic cross-section as measured by the CLEO collaboration [20]. Mind the discontinuous x -axis in the plot, where only the resonance areas are shown.

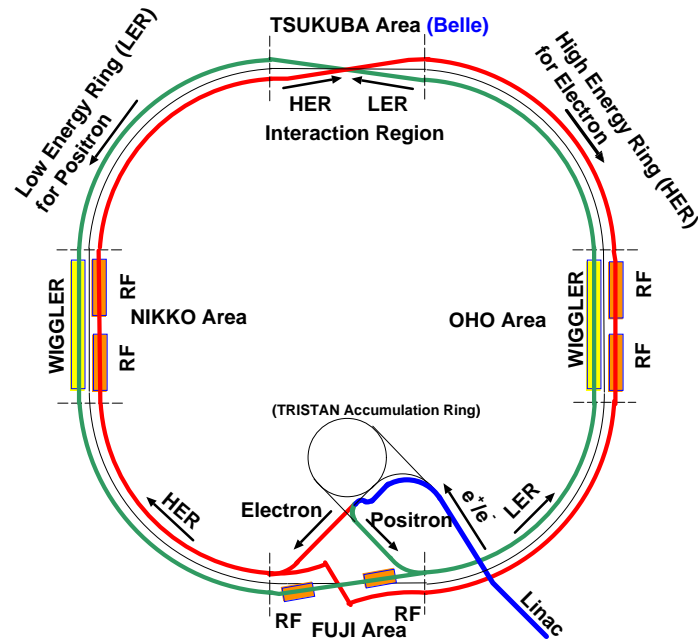


Figure 3.2: The two storage rings for the high and low energy beam with the detector location at the beam crossing at Tsukuba area.

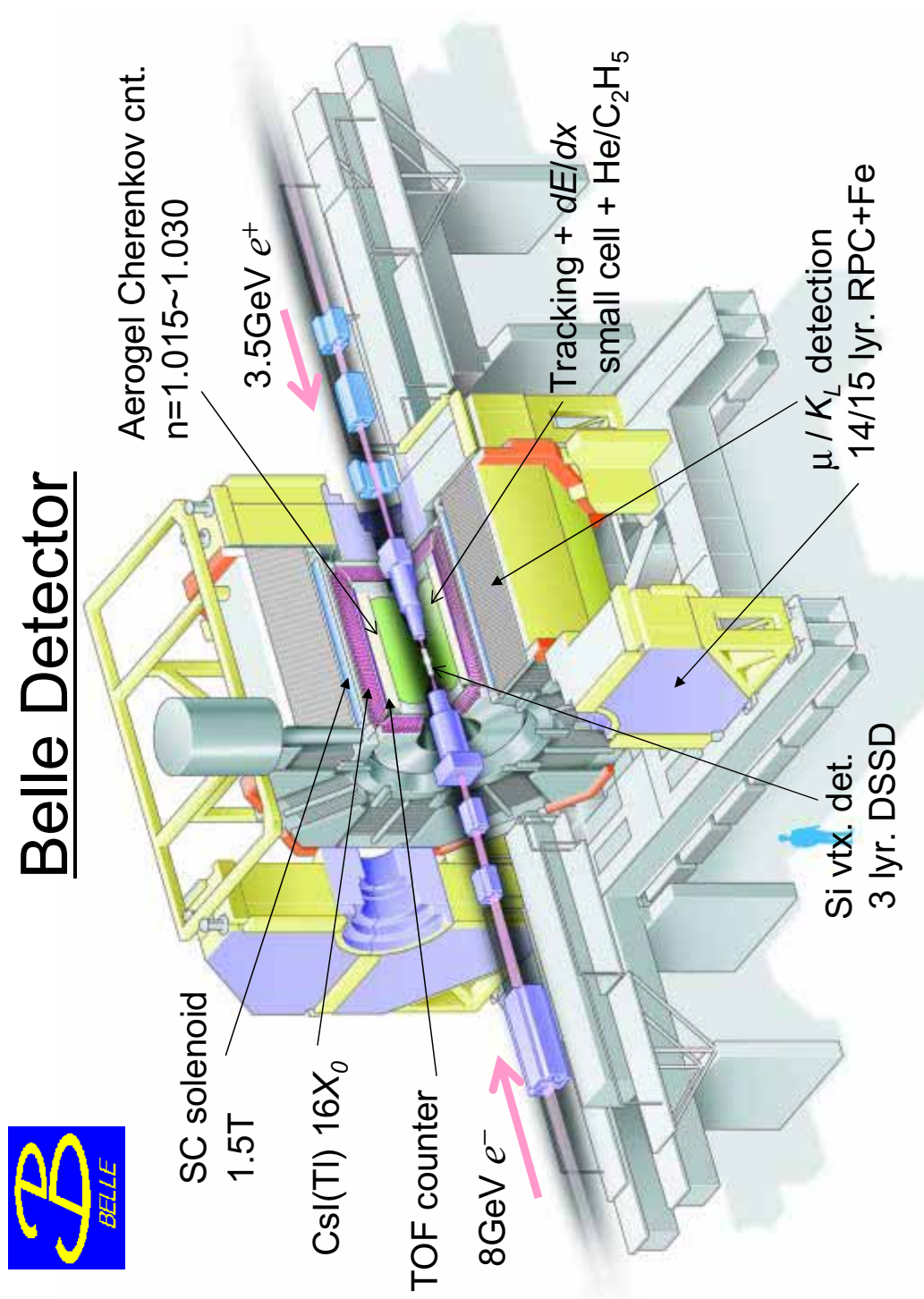


Figure 3.3: An overview of the Belle detector and its subcomponents.

3.2 Description of the Belle Detector

The Belle detector at KEKB has the typical architecture of a cylinder-symmetric setup, characteristic for collider experiments. It is a general purpose detector surrounding the interaction point (IP) to detect particles from the e^+e^- collisions. It can be split into several functional hardware components, listed by increasing radial distance from the center (compare with figure 3.3):

- A double walled cylindrical beryllium beam pipe around the interaction region, cooled with helium gas.
- EFC: “Extreme Forward Calorimeter” in the otherwise uncovered small angle regions, exposed to highest radiation-levels.
- Tracking detectors:
 - SVD: “Silicon Vertex Detector” for the precise tracking of charged particles near to the decay vertices.
 - CDC: “Central Drift Chamber” for the tracking of charged particles and energy loss measurements for particle identification.
- ACC: “Aerogel Cerenkov Counter” for particle identification.
- TOF: “Time-Of-Flight” scintillator counter.
- ECL: “Electromagnetic Calorimeter” for the detection of electromagnetic showers, based on $CsI(Tl)$.
- 1.5 T superconducting solenoid, generating the spectrometer’s magnetic field.
- Iron yoke of the solenoid with integrated KLM: Hadron calorimeter and identification of Muons and K_L^0 mesons by interspersed resistive plate counters.
- DAQ: The trigger and data acquisition system.

- Off-line software and computing.

Explicit details of the detector layout can be found in [21, 22].

The right handed coordinate system of Belle aligns the positive z -axis with the opposite direction of motion of the positron beam. The y -axis points upwards and the x -axis, perpendicular to both, points away from the center of the KEKB rings. In order to cope with the boost of the center-of-mass system w.r.t. the laboratory system, the components of Belle are asymmetrical in z . This can be seen exemplarily in the design of the CDC as shown in the side view of fig. 3.5. Three main regions can be identified in the detector: the barrel section parallel to the beam axis, and the two endcaps, extending radially from the beam axis at the forward and backward ends of the detector. Table 3.1 shows the polar angle coverages of the sections, where θ is the polar angle relative to the z -axis.

All physics analyses rely heavily on a precise spatial reconstruction of the decay vertices. This is supported by the hardware (Si microstrip vertex detector, SVD), as well as sophisticated methods for track and ultimately vertex reconstruction. Thus the tracking detector systems are of utmost importance for the overall performance of such an experiment.

Region	Polar angle coverage
Forward endcap	$17^\circ < \theta < 34^\circ$
Barrel	$34^\circ < \theta < 127^\circ$
Backward endcap	$127^\circ < \theta < 150^\circ$

Table 3.1: Angular coverage of the different detector components

3.2.1 Beam pipe

As the only significant layer of material between the IP and the innermost detector layers, it should be minimizing multiple scattering and energy loss of charged particles. It was therefore designed as two cylinders of beryllium, with the gap filled by helium gas as a cooling medium. The pipe is heated by ohmic currents and so-called high order mode losses in the material as the

bunches of beams circulate. A 20 μm thick gold film on the outer cylinder absorbs low energy X-rays from the HER. The material thickness of the beam pipe corresponds to 0.9% of a radiation length.

3.2.2 Extreme Forward Calorimeter

The EFC extends the polar angle coverage of the overall detector. It detects photons and electrons in an area uncovered by the ECL and is important as a luminosity monitor by detecting Bhabha scattering at low polar angles. Being placed around the beam pipe, close to the IP, it is exposed to very high radiation levels. Therefore radiation-hard bismuth germanate (BGO) crystals are used as scintillator material. Photodiodes read out the signal. The polar angle coverage is in the range of $6.4^\circ < \theta < 11.5^\circ$ for the forward, and $163.3^\circ < \theta < 171.2^\circ$ for the backward EFC. In terms of material budget, they correspond to 12 and 11 radiation lengths, respectively. The EFC is exclusively used for luminosity measurement, which is done by monitoring Bhabha scattering processes.

3.2.3 Silicon vertex detector

For time dependent CP analyses it is of major importance to determine the z -axis position of the B meson decay vertices. The original silicon vertex detector (SVD) configuration can be seen in figure 3.4. With its three layers of double-sided silicon strip detectors (DSSD), it covers a region of $23^\circ < \theta < 139^\circ$, which amounts to 86% of the total solid angle.

The SVD is composed of so-called ladders, on which the DSSDs are mounted. The three layers consist of 8, 10 and 14 of such ladders, accounting for the increasing circumference to be covered. Each ladder is made of two half-ladders, which contain one or two DSSDs, supported by boron-nitride ribs and carbon-fiber reinforced plastic. All in all, the SVD is composed of 32 ladders and 102 DSSDs.

The DSSDs are reverse-biased diode-strip detectors, and were originally designed for the micro-vertex detector of the DELPHI experiment at

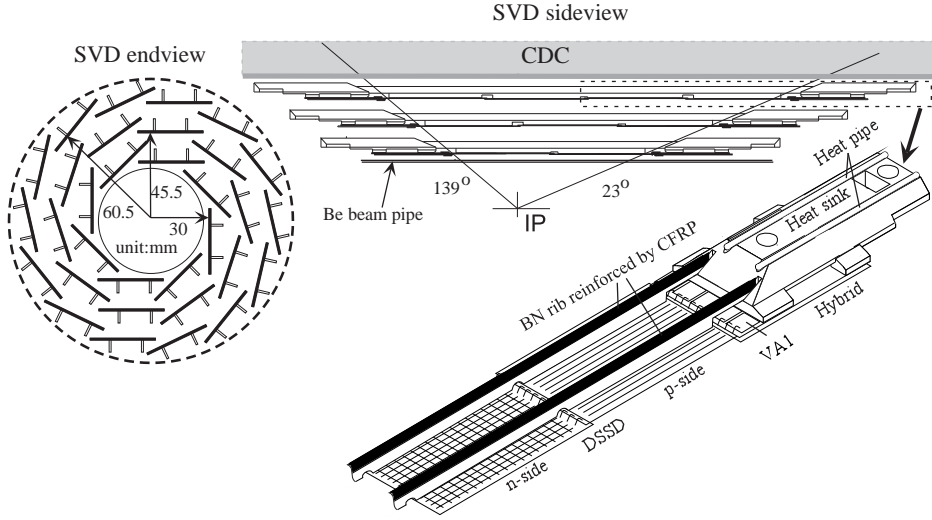


Figure 3.4: SVD1 configuration.

LEP [23]. Each is $300\ \mu\text{m}$ thick and contains 1280 sensor strips and 640 read-out pads. The side with strips parallel to the beam measures the azimuthal arc $R\phi$ and is made of p-doped silicon with p^+ readout strips, which have a pitch of $24\ \mu\text{m}$. The other side, with strips oriented perpendicular to the beam and measuring the z coordinate, carries n^+ readout strips with a $42\ \mu\text{m}$ pitch. When a charged particle penetrates a DSSD, it creates electron-hole pairs, which drift to the appropriate side of the DSSD, due to the bias voltage. The charge deposition is measured and read out.

Signals from the DSSDs are read out by VA1 chips ($1.2\ \mu\text{m}$ CMOS fabrication), which tolerate radiation levels of up to 200 kRad. The VA1 chips' signals are digitized by FADCs located in the electronics hut. There, common mode noise subtraction, data sparsification and formatting is carried out.

The precision requirement for the aforementioned time dependent CP asymmetries studies is $100\ \mu\text{m}$ in the z -axis direction. For a charged particle with momentum $1\ \text{GeV}/c$ an impact parameter resolution of about $55\ \mu\text{m}$ is achieved.

In Summer 2004, an upgrade of the silicon tracker system was made, and

a four-layer vertex detector (SVD2) was installed. It covers a larger angular range ($17^\circ < \theta < 150^\circ$), and utilizes the benefits of a smaller beam pipe diameter, thus bringing the innermost layer closer to the primary interaction point (from 3 to 2 cm). The fourth outermost layer made necessary some changes to the CDC inner wall. SVD2 now contains 6, 12, 18 and 18 full ladders in each layer (from inside to outside), and a half ladder consists of 1, 2 or 3 DSSDs.

The SVD2 DSSDs have 512 readout channels in both (Rz) and $(R\phi)$, with a total of 110592 channels. Limited radiation tolerance levels of SVD1's VA1 front-end readout chips was circumvented by replacing them with VA1TA chips, which is of $0.25\ \mu\text{m}$ CMOS fabrication, with an expected stable performance of up to 20 MRad. Extensive information on the silicon tracker systems can be found in [24, 25, 26].

3.2.4 Central Drift Chamber

The central drift chamber (CDC) provides detailed information on the particle position, momenta and their specific energy loss dE/dx . Energy loss data is used to provide information for particle identification (PID), i.e. distinguishing kaons, pions, protons and electrons. All components in the Belle detector out to the ECL are contained in a 1.5 T nearly uniform magnetic field, provided by a solenoid magnet. The field is oriented in the positive z direction and causes the charged particle to follow a helical path, the helix axis being in the field direction. This helix can be decoupled into a circular motion in the (x, y) -plane, defined by three parameters, and a straight motion in the (R, z) -plane, defined by two more parameters. From these five parameters it is possible to determine the closest approach of the helix to the interaction point (IP) and the momentum components perpendicular and parallel to the magnetic field. These measurements are the primary purpose of the CDC.

Since the physics goals of the Belle experiment require a transversal momentum resolution of $\sigma_{p_t}/p_t \sim 0.5\% \sqrt{1 + [p_t/(\text{GeV}/c)]^2}$ for charged particles with $p_t \geq 0.1\ \text{GeV}/c$, the setup has been fine tuned to yield a reso-

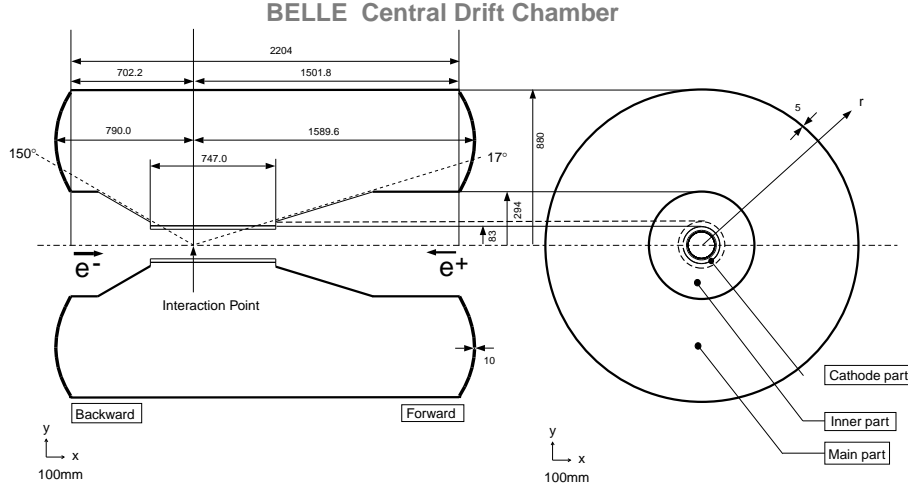


Figure 3.5: The CDC in front and side view, showing the three major parts: main long wire region, inner short wire region and cathode electrodes for the innermost wires.

lution of $\sigma_{p_t}/p_t \approx 0.35\%$. The spatial resolutions are $\sigma_{r\phi} = 130 \mu m$ and $\sigma_z = 200 \dots 1400 \mu m$ (depending on θ).

The CDC consists of three parts (see figure 3.5):

- Main: long wire region.
- Inner: short wire region.
- Cathode: readout electrodes for the innermost wires.

For the main part curved aluminum endplates support the mechanical forces for a total of 3.5 tons of wire-tension. 50 layers of Au-W sense wires of $30 \mu m$ diameter and a maximum of $2400 mm$ in length fill the active detector volume. Each sense wire is surrounded by eight $126 \mu m$ Al field-shaping wires, together forming a drift cell of about $16 mm$ in radial direction by about $18 mm$ in $R\phi$ direction. A total of 8400 adjacent drift cells provide a sensitive volume of radii from $88 mm$ to $863 mm$; the polar angle of this volume ranges over $17^\circ \leq \theta \leq 150^\circ$.

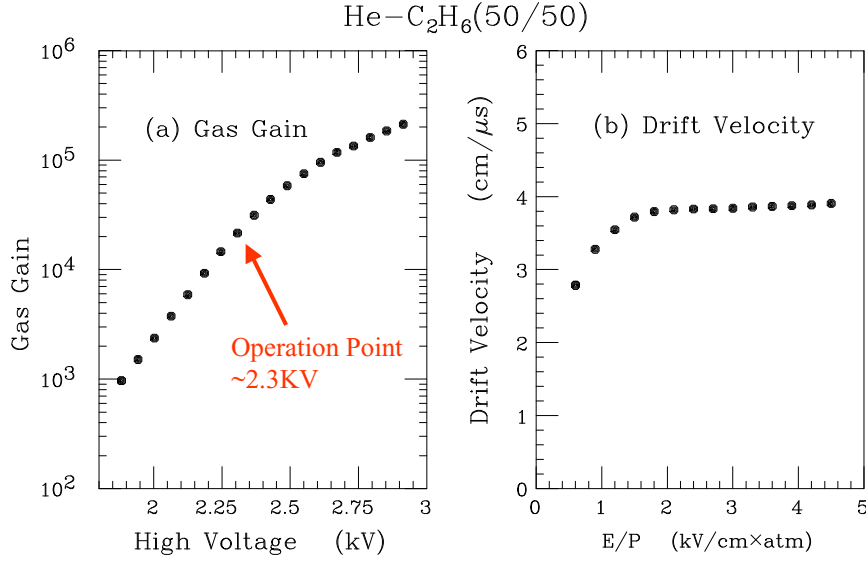


Figure 3.6: The gas mixture used in the CDC, its drift velocity and gain behaviour depending on the applied voltage on the sense wires.

The layers are grouped in batches of so called ‘super-layers’ of 3 to 5 ordinary layers. There are 2 types of layers: so-called *axial layers*, whose wires are aligned parallel to the beamline axis, and so-called *stereo layers* which are mounted on the supporting structure with a “slant” in order to provide, by their stereo angle, additional z -coordinate information in the measurements.

At the inner part of the CDC, the endplates have conical shapes to make room for accelerator components right next to the interaction point.

Because many of the decay products of B mesons have momenta below 1 GeV/ c , the minimization of multiple Coulomb scattering effects is a necessity. Therefore a gas with low atomic number Z , (a mixture of 50% He and 50 % C₂H₆) has been used, with a long radiation length of 640 m. In figure 3.6 the properties of the gas used w.r.t. the wire voltage can be seen; the drift velocity saturates at 4 cm/μs at a relatively low field intensity.

Additional z -coordinate information from cathode strips was never used (in a more than experimental way), which is due to a bad signal-to-noise ratio of the electronic output.

The CDC measurements are the starting point for track reconstruction, since in the outer regions of the CDC the track density is rather low, which allows for less ambiguous initial conditions for the reconstruction algorithms.

Though the explicit z-coordinate cathode strips information is never used in the track fitting for the CDC, it is introduced implicitly by using the measurements of the stereo-wires with their slightly slanted alignment. This results in a position estimate along the z-coordinate, though with big errors. The final results of the track fit include additional information of the SVD, which provides more precise positional data in both $R\phi$ and z .

3.2.5 Aerogel Čerenkov Counter

Designed for K^\pm and π^\pm separation in the momentum range of 1.2 GeV/ c to 3.5 GeV/ c , the ACC detects Čerenkov light which is emitted when a particle travels through a medium at a higher velocity than the signal speed of light in that medium. For a refractive index n , Čerenkov light is emitted if the velocity $\beta = v/c$ of the particle satisfies:

$$n > 1/\beta = \sqrt{1 + (mc^2/p)^2}$$

with m and p being the mass and momentum of the particle, in units of GeV/ c^2 and GeV/ c , respectively. Therefore, depending on the refractive index, there will be a range of momenta for which e.g. pions will emit Čerenkov radiation, but kaons will not.

The barrel part of ACC consists of 960 counter modules, which are grouped into 60 cells in the azimuthal direction ϕ . In the forward and backward endcaps, the ACC consists of 228 modules, arranged in 5 concentric layers. Five different types of aerogel, with varying refractive indices, are used. A sideview of the layout is shown in fig. 3.7.

Each counter module is made of silica aerogel, filled into 0.2 mm thick aluminum boxes, and viewed by fine mesh-type photomultiplier tubes. In total there are 1560 and 228 readout channels in the barrel and end-cap parts, respectively. For further information see [27].

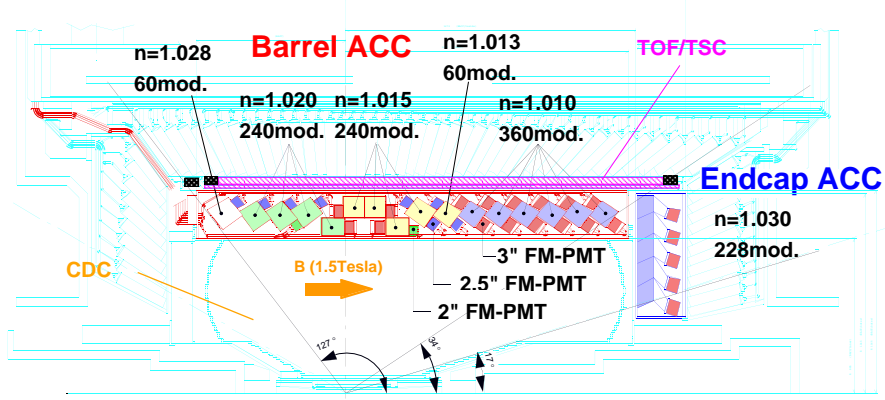


Figure 3.7: ACC setup.

3.2.6 Time-of-Flight and Trigger Scintillation Counters

For complementary information to the ACC, regarding particle identification, the TOF distinguishes K^\pm and π^\pm mesons up to 1.2 GeV/c, where the K/π separation power of the ACC and CDC (by dE/dx) is less effective.

The TOF system also is responsible for providing fast timing information for the trigger system, with time resolutions of around 100 ps. The time of flight T of a particle with mass m traversing a length L is given as:

$$T = \frac{L}{c\beta} = \frac{L}{c} \sqrt{1 + (mc^2/pc)^2}$$

The time between the collision at the IP, and the passage of a particle through the barrel TOF is being measured. This way, a particle's mass can be calculated once its momentum is known. Thus, a quite clear separation of particle species can be achieved by their time-of-flight information.

Both the TOF and the trigger scintillation counter (TSC) are made of fast scintillators and fine mesh-type photomultiplier tubes mounted directly on the scintillator. Two TOF counters and one TSC form one module. 64 TOF modules are located in the barrel region right outside the ACC, and the covered angular region is $33^\circ \leq \theta \leq 121^\circ$. The achieved time resolution of

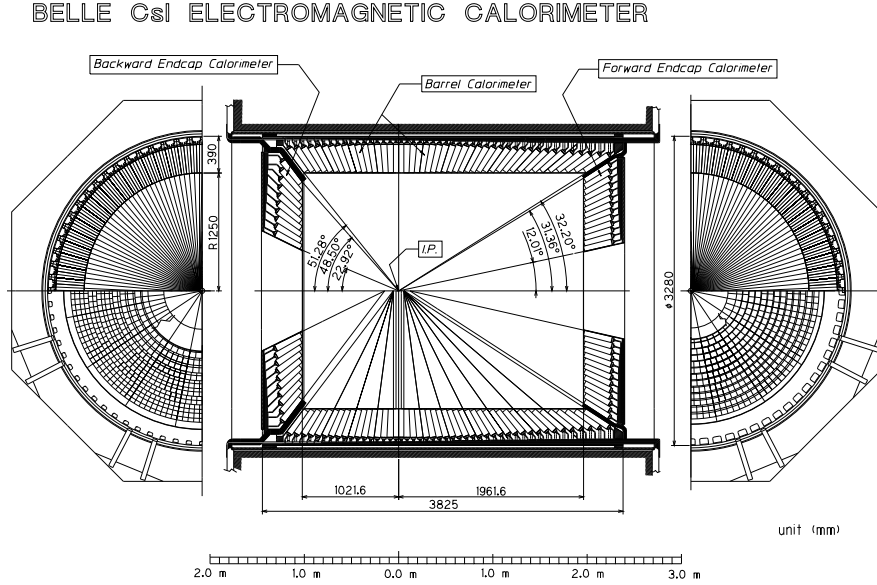


Figure 3.8: ECL configuration.

the TOF scintillators is $\sigma_t = 100$ ps. Combining the information from TOF, ACC and the dE/dx measurement from the CDC results in a better than 3σ separation between charged kaons and pions over the whole momentum range up to 3.5 GeV/ c .

More information on the TOF system can be found in [28, 24].

3.2.7 Electromagnetic Calorimeter

The purpose of the ECL is to measure the energy and position of photons from π^0 and radiative B decays with high efficiency and good resolution in energy and position. The ECL is also used for electron and positron identification. The building blocks of the ECL are tower-shaped CsI(Tl) crystals, which point to the primary interaction region with a small tilt angle in order to avoid photons passing undetected through the gaps between the crystals. Each crystal is 30 cm long, corresponding to 16.2 radiation lengths, and read out by a pair of silicon PIN photodiodes.

The configuration of the ECL is shown in fig. 3.8. Reference [29] indicates

the measured energy resolution to be

$$\frac{\Delta E}{E} = \frac{0.0066(\%)}{E} \oplus \frac{1.53(\%)}{E^{1/4}} \oplus 1.18(\%),$$

with the energy E given in GeV. The first term is from the contribution of electronic noise, while the second and part of the third term come from incomplete electromagnetic shower containment. Also, the third term accounts for systematic effects (uncertainty of light output calibration of the crystals).

For the spatial resolution the following expression is given:

$$\sigma = 0.27 \oplus 3.4/\sqrt{E} \oplus 1.8/E^{1/4} \text{ mm.}$$

In addition to the measurement of photon and electron energy, the ECL plays a major role in electron identification: a charged track pointing to an ECL cluster is identified as an electron or positron if, among other criteria, the energy and momentum are consistent. Trigger information and luminosity information are also provided. (See trigger system description in 3.3).

3.2.8 Solenoid magnet

A 1.5 T magnetic field, oriented parallel to the beam pipe, is provided by a superconducting solenoid for charged particle momentum measurements. The coil consists of a single niobium-titanium-copper alloy layer, which is embedded in a high-purity aluminum support cylinder, measuring 3.4 m in diameter and 4.4 m in length. Liquid helium circulation through a tube on the inner surface of the aluminum cylinder provides for indirect cooling. The solenoid layout is shown in figure 3.9.

3.2.9 K_L and Muon Detector

The KLM was designed for the detection of K_L^0 mesons and muons with momentum larger than 600 MeV/c. Placed outside the solenoid, it consists of 15 layers of Resistive Plate counters (RPC) with 14 layers of 4.7 cm thick iron plates for the barrel region, and 14 RPC layers in the endcap region.

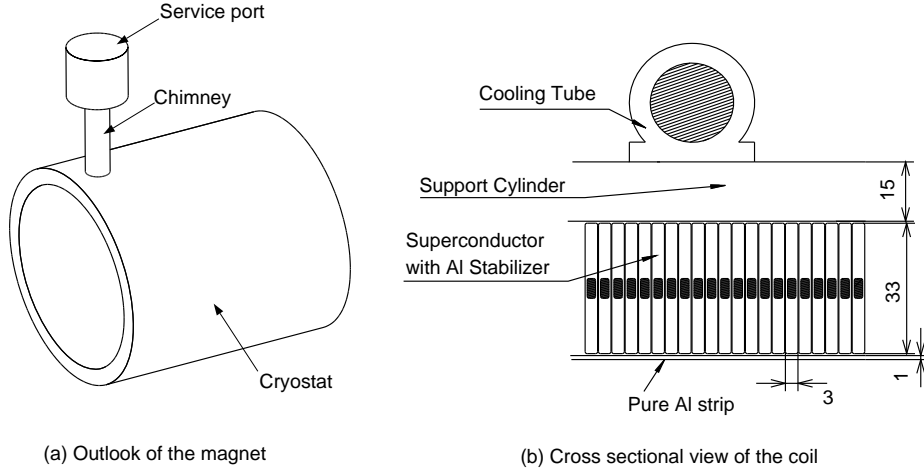


Figure 3.9: Superconducting solenoid layout.

An RPC super-layer consists of two RPC planes providing both polar and azimuthal angle information. The iron plates also serve as return yoke for the solenoid's magnetic field. The polar angle region covered by the KLM is $20^\circ \leq \theta \leq 155^\circ$. Signals are read out from cathode strips in both directions. There are a total of 21856 and 16126 readout channels for the barrel and the two endcap detectors, respectively. The resolutions for K_L mesons is 30 mrad (θ and ϕ) in direction, and a few nanoseconds in time.

Up to the KLM, all the detector material corresponds to approximately one hadronic interaction length for K_L mesons. The KLM iron plates provide further 3.9 interaction lengths of material, necessary for high efficiency detection.

A shower of hadrons is produced when the mesons interact with matter, thus leaving a cluster of hits in the KLM which is not associated with a charged track. In contrast, the muons will have such an associated charged track, and produce a “line” of KLM hits rather than a shower, and can thus be discriminated from K_L^0 . The detection efficiency for muons with momentum greater than 1 GeV/c is greater than 90%, with a fake rate of about 2%, resulting from non-interacting pions and kaons.

3.3 Data acquisition and Trigger system

The task of the trigger system is to decide when the subsystems of the Belle detector should record an event. If a collision event satisfies the trigger criteria, the subsystems are read out and data are stored for possible further use. “Event” is interchangeably used for both the actual particle collision, and the stored data representing the collision. Removing background events while retaining events of interest with high efficiency is the aim of carefully chosen trigger criteria. Once an event is triggered, the DAQ system transfers the raw data from the detector to the data storage system.

There are several main sources for background events:

- Undesired interactions between the e^+ and e^- beams, such as Bhabha scattering,
- Collisions of a beam particle with residual gas molecules or the beam pipe,
- Synchrotron radiation from the beams.

Interesting events are mainly hadronic and QED events, which are used for physics analyses, detector calibration, and luminosity measurements.

Overall event rates for physics and background events at the design luminosity of $10^{34} \text{ cm}^{-2} \text{ s}^{-1}$ are approximately 100 Hz each. To allow for higher background levels, the design specifications of the trigger will permit an operation of up to 500 Hz. A scheme of the trigger system is shown in fig. 3.10.

Its components are the level 1 (L1) hardware trigger, the level 3 (L3) software trigger implemented by the online computing facilities, and the level 4 (L4) trigger in the off-line Belle computing farm¹. The level 4 trigger achieves very efficient background event detection by carrying out a full event reconstruction.

¹There is no L2 trigger; the numbering follows a historical design

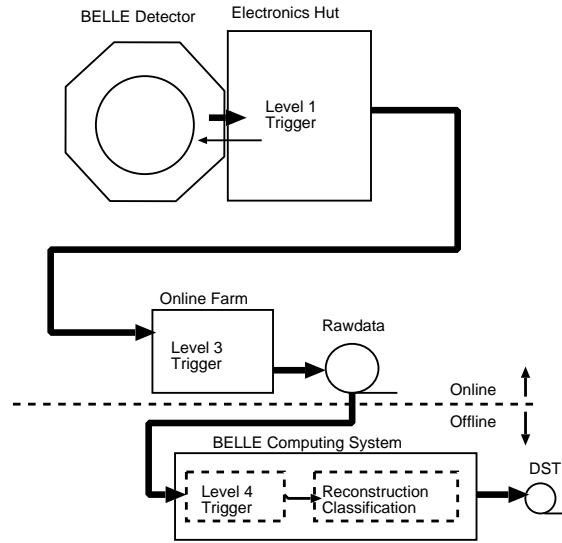


Figure 3.10: Overall Belle trigger scheme.

3.3.1 The L1 trigger

The L1 trigger consists of the sub-trigger systems (implemented in subdetectors), and the central trigger (also called global decision logic, GDL). All subtrigger signals must arrive at the GDL within $1.85 \mu\text{s}$ after the physical event has occurred, and the final L1 signal is issued $2.2 \mu\text{s}$ after the event. The trigger signal also determines the readout timing. For the final signal, the TOF trigger or the ECL subtriggers are used.

Sub-trigger systems

The CDC provides two different types of triggers: the $r - \phi$ trigger and the z trigger [30]. The TOF produces trigger signals based on the hit multiplicity and back-to-back topology. The ECL trigger is based on trigger cells formed of combinations of 4×4 crystals, providing also trigger information based on the $\theta - \phi$ segmentation by utilizing the number of isolated clusters. The KLM detects muons using four (two) layers in the barrel (endcap) parts. The EFC provides a Bhabha trigger (forward-backward coincidence), and a two-photon trigger.

There also is a “random trigger” to allow studies of the background noise in the overall detector.

Global Decision Logic

Up to 48 subtrigger signals arrive at the GDL, coming from the CDC, TOF, ECL, KLM and EFC systems. More information can be found in [31]. The GDL properly aligns the subtrigger signals by adjusting their timing, adding an appropriate delay to each channel. It performs some trigger logic operations, and again generates 48 types of triggers (since experiment 21 this number increased to 64)². The final trigger decision is issued $2.2 \mu\text{s}$ after the e^+e^- collision. Four main triggers constitute the hadronic trigger:

- Two-track trigger: Requires two CDC tracks with $r - \phi$ triggers and at least one track with z trigger, and an opening angle greater 135° . It also requires TOF hits and ECL clusters.
- Three-track trigger: Similar to the two-track trigger, with CDC $r - \phi$ information for three or more tracks. Different trigger types are defined depending on track multiplicity, opening angle, TOF, and ECL cluster hits.
- Isolated cluster counting trigger: Four or more isolated ECL clusters (suppressing Bhabha events).
- Total energy trigger: The analogue sum of deposited energy in the ECL to be greater than 1 GeV. Vetoed by ECL Bhabha and cosmic ray triggers.
- Combined trigger: Combination of track, energy and cluster trigger.

The efficiency for each individual trigger ranges from 90% to 97% for $B\bar{B}$ events. Using the overlap of the combined triggers allows for a total efficiency of more than 99%. The L1 trigger rates are correlated to the beam current, the luminosity and the beam background condition.

²In the Belle experiment the data samples are segmented into so called “experiments” which signify different periods of operation where the overall setup of the data acquisition process remains unchanged.

3.3.2 The L3 and L4 triggers

In order to reduce the number of events stored, the L3 trigger checks L1 trigger information, and also passes some special event categories such as Bhabha and random trigger events. For the other events, the L3 trigger performs a fast data reconstruction, discarding an event if there is no track with $|z| < 5$ cm at the primary interaction point, thus efficiently discarding a large portion of the beam background. Being online since experiment 11, the L3 trigger reduces the number of events stored by a factor of 2. It also retains an efficiency of more than 99% for hadronic and τ -pair events. Only the L1 and L3 triggers reduce the recorded data size on-line.

The L4 trigger filters events right before the complete off-line event reconstruction takes place. It uses a fast algorithm which reconstructs tracks in order to reject them if they are originating too far from the IP. The rejected events are still kept in the raw data, but no full reconstruction is performed in the later steps. Therefor the L4 trigger helps saving CPU time in the production chain. About 78% of all events are rejected by the L4 trigger, while nearly 100% of B meson events are kept.

3.3.3 Data Acquisition

The DAQ system records the events specified by the trigger up to the defined limits of 500 Hz. A distributed-parallel system which is segmented into 7 subsystems is used to process data from each subdetector. An overview of the Belle DAQ system can be seen in fig. 3.11 [32].

For most subdetectors the signals first go through a charge-to-time (Q-to-T) converter and subsequently are processed by a time-to-digital converter (TDC). A pulse with a width proportional to the input charge is produced by the Q-to-T conversion, and the TDCs digitize the timings of the leading and trailing edges of the pulses. Only the SVD uses FADCs, and the KLM has no Q-to-T converter, because the pulse height contains no useful information.

When the sequence controller receives the final trigger from the GDL, the readout process begins by a common stop signal to all TDCs of the subsystems. The event-builder combines all subdetector data into a single

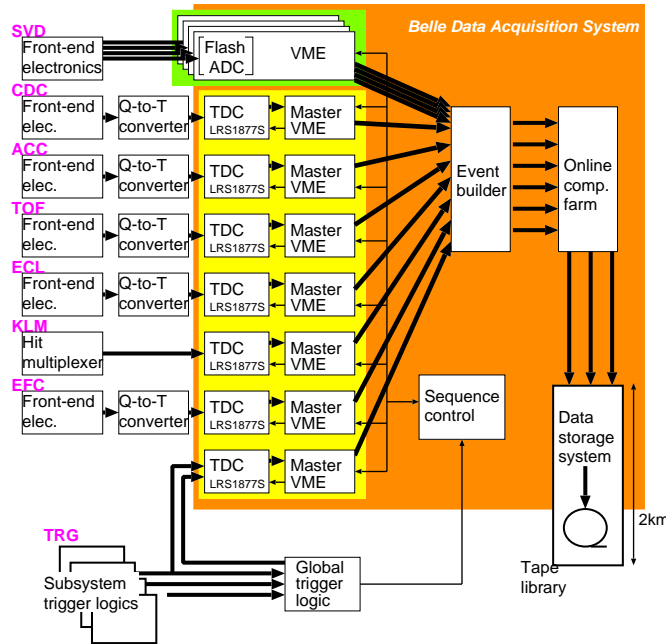


Figure 3.11: The Belle DAQ system.

event. After passing the data through the L3 trigger, they arrive at the online computing farm, where the quality is monitored by the online data quality monitor (DQM).

In the last step the data is sent to the mass storage system via optical fiber. It is stored permanently at the KEK computing center. A typical hadronic event is 30kB in size, corresponding to a maximum transfer rate of 15 MB/s at 500 Hz trigger rate.

3.3.4 Data Processing

L4 trigger accepted events are reconstructed and subsequently stored on data summary tapes (DSTs). The raw data of the detector devices are converted into physics information of momentum 3-vectors, IP proximity, and particle identification (PID) information. The reconstruction procedure roughly goes as follows:

CDC information allows the reconstruction of charged tracks. The tracks

are extrapolated inwards to the SVD and outwards to the ACC, TOF, ECL and KLM, and a search for associated signals is performed. Hits in ECL and KLM with no associated track in CDC are assumed to be neutral particles (photons, K_L mesons). Four-vectors are assigned to the charged tracks and neutral particles. PID likelihoods are calculated. Other flags and variables are determined, and the summary information is written to DST. An event classification according to several categories and selection criteria is carried out, which results in so called “skimmed data”.

3.4 Software

The large pool of software, which has been developed by the Belle collaboration is composed of several parts running the DAQ and data reconstruction, the physics analysis, and the simulation of data. The last two parts are known as the Belle analysis framework (BASF). BASF consists of a kernel, a user interface, and modules which are dynamically loaded into the kernel at run time. A user-specific physics analysis is implemented as such a dynamic module. Monte carlo (MC) simulation and generation of MC events is also done using the BASF.

3.4.1 Monte Carlo Event Generation

Comparing distributions of real data to expectations from theoretical models is an important part of high energy physics analysis. A straight-forward analytic approach to this problem is impossible due to the complexity of the various subsystems involved, such as the detector response and the various physics processes mimicking the signal to be studied. Because of this, all involved processes are modelled using MC simulation. Real data distributions are then compared to corresponding distributions from simulation, which consist of significantly more events in order to reduce the statistical fluctuations. Such a simulation has to be aware of the detailed detector geometry, the response and all deficiencies of the whole detector system.

The production of MC data takes two major steps. First the underlying

physics processes are simulated, which occur in and after the collision of an e^+e^- pair. Primary particles which decay inside the beam tube are generated. In a second step, the detector response of their decay products, which are longer-lived, is simulated. In the first stage, the QQ [33] event generator (for newer analyses the EvtGen [34] event generator) is used to model the particle physics processes. It models most accurately the underlying physics processes by employing compiled production rates data from many different experiments, while also accounting for the relevant information of the KEKB accelerator.

The PYTHIA program [35] is used for the generation of background continuum events, which utilizes the Lund string fragmentation model to calculate the hadronization processes. The amount of continuum events generated is about three times the luminosity in actual data.

After the generation of the underlying physics processes, either from QQ, EvtGen, or PYTHIA, the data is processed in the BASF module GSIM. This module simulates the complete detector response, and is based on the CERN detector simulation package GEANT3 [36]. After simulation of the interactions between the final state particles and the detector, the data is reconstructed in the same way as real data, with the final DSTs containing additional “MC truth” event generator information. The accuracy of all those simulation processes is of vital importance. Some noise hits are added to the MC events by taking random trigger events and inserting them into the data. The variations in the primary interaction profile, the evolutions in the subdetectors, and the (dis)appearance of dead channels are also accounted for.

Chapter 4

Event reconstruction

This chapter is a summary of the data sample used including all necessary cuts applied for background suppression. We describe the base events, skimmed by a module initially written for B tagging, with the investigated decay channels. This is followed by details of the reconstruction of the not fully reconstructible second B meson by using criteria to select semi-leptonic decays with a high momentum lepton.

4.1 Data selection

The present analysis uses Belle datasets comprising experiments 7 through 27, which have been recorded until summer 2003. Amounting to a total of 140 fb^{-1} of $\Upsilon(4S)$ resonance data, this corresponds to approximately 7.6×10^7 $B^0\bar{B}^0$ events. For the non- $B^0\bar{B}^0$ background estimation 15 fb^{-1} have been taken 60 MeV below the resonance.

Three different Monte Carlo sets of varying sizes have been used to test the fit procedure. All of the MC sets were produced using the **EvtGen** event generator [34]. A complete **GEANT**-based detector simulation [36] was applied to the MC events.

The first set is a generic MC simulation that has a size of about three times the resonance data. It was produced as part of the standard procedure allowing detailed MC studies with sufficient statistical reliability.

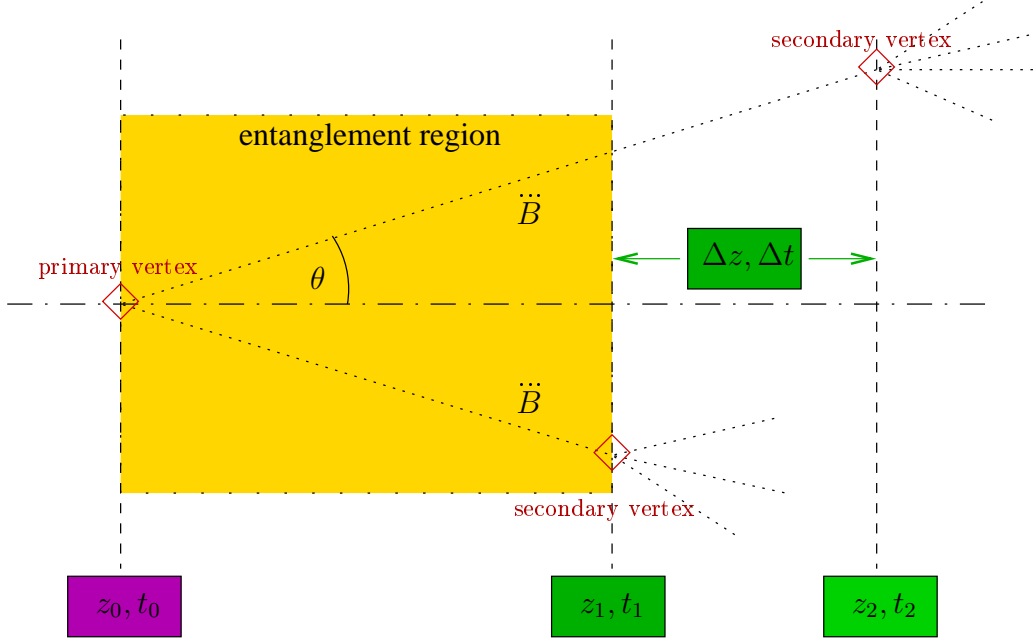


Figure 4.1: Exemplary decay at the primary vertex of an $\Upsilon(4S)$ resonance into an entangled flavor oscillating $B^0\bar{B}^0 \leftrightarrow \bar{B}^0 B^0$ meson pair (indicated by $\bar{B}\bar{B}$). This entangled state propagates oscillating until the first B meson decays at time t_1 , while the second B meson still oscillates in flavor until it decays at time t_2 . The angle θ is rather small, so that $\tan(\theta) \approx 0.1$.

The MC sets 2 and 3 have been produced by using a modified version of the **EvtGen** $B^0\bar{B}^0$ decay model. The size of those sets is about two times the resonance data. Their purpose is to test the sensitivity of the presented method w.r.t. the deviation of the entangled B -meson pairs behavior from standard quantum mechanics.

4.2 Particle selection

Low-momentum particles will loop in the CDC detector and therefore pass close to the interaction point more than once. This results in duplicate tracks in the reconstruction, which will be so-called “ghosts”. Selecting pairs of charged tracks following certain criteria (see table 4.1) will allow removal of such tracks with good efficiency.

$p_t < 275 \text{ MeV}/c$ $\Delta p = \vec{p}_1 - \vec{p}_2 < 100 \text{ MeV}/c$ $\text{angle}(\vec{p}_1, \vec{p}_2) < 15^\circ$ $\text{angle}(\vec{p}_1, \vec{p}_2) > 165^\circ$	transversal momentum momentum difference for same charge sign for opposite charge sign
--	---

Table 4.1: Criteria for identifying duplicate track pairs. MC simulation shows that only 81% of the identified pairs are in fact duplicates, i.e. belong to the same physical particle. The efficiency for identifying a duplicate pair is 51%.

When a duplicate track pair has been identified in this manner, the track with the larger value of $(5|dr|)^2 + |dz|^2$ is rejected, where $|dr|$ and $|dz|$ are the unsigned impact parameters (w.r.t. to the true interaction point) in R and z , respectively.

The remaining tracks must satisfy momentum-dependent impact parameter selections as shown in table 4.2.

	$p_t < 250 \text{ MeV}/c$	$250 < p_t < 500 \text{ MeV}/c$	$p_t > 500 \text{ MeV}/c$
$ dr $	$< 20 \text{ cm}$	$< 15 \text{ cm}$	$< 10 \text{ cm}$
$ dz $	$< 100 \text{ cm}$	$< 50 \text{ cm}$	$< 20 \text{ cm}$

Table 4.2: Selection of charged tracks based on transverse momentum and impact parameters in R and z .

Gammas are selected by using the “good_gamma() flag”. This flag selects photons by requiring unmatched clusters in the electromagnetic calorimeter, thus excluding a charged particle calorimeter hit. A polar angle acceptance window is also defined, and the shape of the electromagnetic shower has to be more confined than for a charged particle. Also, minimum energy cuts which are shown in table 4.3 are applied.

	$17^\circ < \theta < 32^\circ$	$32^\circ < \theta < 130^\circ$	$130^\circ < \theta < 150^\circ$
E_γ	$> 100 \text{ MeV}$	$> 50 \text{ MeV}$	$> 150 \text{ MeV}$

Table 4.3: Neutral cluster selection by the electromagnetic calorimeter. Endcaps are more affected by background than the barrel, thus tighter cuts are used.

4.3 Full reconstruction side

Basis of the presented study is the “*full reconstruction version 1*” skim (fullrec v1, FRv1). There also is a more recent FRv3 skim available for analyses, but this skim includes more decay modes, which are not as clean as the FRv1 (more background events are included), which led to the choice of FRv1 for the study at hand. In the FRv1 sample, events are selected if at least one fully reconstructible B meson candidate is found in the decay modes $B^0 \rightarrow D^{(*)-}\{\pi^+/\rho^+/a_1^+\}$ and $B^+ \rightarrow \bar{D}^{(*)0}\{\pi^+/\rho^+/a_1^+\}$, as well as their respective charge conjugates. We will call this “side” of the B meson pair decay the “*full reconstruction side*” (FR side).

For the full reconstruction v1 skim the primary charged tracks are reconstructed with hit information from SVD and CDC. Track quality cuts based on their impact parameters relative to the measured beam interaction profile have to be satisfied. Charged kaons are identified by combining measurement information of ionization loss (dE/dx) in the CDC, Čerenkov light yields in the ACC, and time-of-flight data in the TOF. Identification efficiency is roughly 88% for kaons, and the fake rate for pions is about 8% for the typical requirement.

The reconstruction of π^0 meson candidates is done using $\gamma\gamma$ pairs with invariant mass between 117.8 and 150.2 MeV/ c^2 , while each photon is required to have a minimum energy deposit of more than 50 MeV. K_S^0 mesons are reconstructed using pairs of charged tracks that have an invariant mass within ± 30 MeV/ c^2 of the known K_S^0 mass, and a well reconstructed vertex that is displaced from the primary interaction point. ρ^+ and ρ^0 are reconstructed in the decay modes $\pi^+\pi^0$ and $\pi^+\pi^-$, while their invariant mass is required to be within ± 150 MeV/ c^2 of the nominal ρ mass. a_1^+ candidates are selected by combining a ρ^0 candidate and a π^+ if their invariant mass is between 1.0 and 1.6 GeV/ c^2 , and also requiring for the three tracks to form a good vertex.

\bar{D}^0 and D^- candidates are reconstructed in the $\bar{D}^0 \rightarrow \{K^+\pi^-, K^+\pi^-\pi^0, K^+\pi^+\pi^-\pi^-, K_S^0\pi^0, K_S^0\pi^+\pi^-\}$ and $D^- \rightarrow \{K^+\pi^-\pi^-, K_S^0\pi^-\}$ decay modes, respectively. These are required to have an invariant mass m_D within $\pm 3\sigma$

of the nominal D mass. \bar{D}^* mesons are reconstructed by combining the \bar{D} candidate and a low momentum pion, $D^{*-} \rightarrow \bar{D}^0 \pi^-$ and $\bar{D}^{*0} \rightarrow \bar{D}^0 \pi^0$; they are required to have a mass difference $\Delta m = m_{\bar{D}\pi} - m_{\bar{D}}$ within $\pm 3\sigma$ of the nominal value.

The selection of the B candidate is based on the beam-constrained mass, $m_{bc} = \sqrt{E_{\text{beam}}^{*2} - p_B^{*2}}$, and the energy difference $\Delta E = E_B^* - E_{\text{beam}}^*$ ¹. Here E_{beam}^* is the beam energy in the center-of-mass system, $E_{\text{beam}}^* = \sqrt{s}/2 \approx 5.29$ GeV, and p_B^* and E_B^* are the momentum and energy of the reconstructed B in that system. Events satisfying $m_{bc} \geq 5.2$ GeV/ c^2 and $|\Delta E| \leq 0.3$ GeV are subjected to further analysis.

The actual signal region for the B meson is defined with the cuts $m_{bc} \geq 5.27$ GeV/ c^2 and $|\Delta E| < 0.05$ GeV (see Figures 4.2 and 4.3). For an event that has multiple B meson candidates, the one with the smallest χ^2 is chosen, based on deviations from nominal values of ΔE , m_D , and Δm if applicable.

Regarding the prominence of signal and background events, we will define two regions: The “signal region” and the “sideband region”, which will later be used for the extraction of signal events and the normalization of expected background events, respectively. Figure 4.3 shows the location of those two regions in the plane of kinematic variables m_{bc} and ΔE .

4.4 Partial reconstruction side

This part of the event selection is concerned with the reconstruction of the second B meson candidate of the pair. It relies on the identification of a high momentum primary lepton coming from the decay of the B meson. That lepton allows for a precise determination of the second decay vertex which is crucial for the time difference measurements in the present study.

Some basic requirements have to be fulfilled for this second “side” of the whole event topology, which we will refer to as the “*partial reconstruction side*” (PR side), since in most cases no full information on the decay products is available. All remaining tracks of the event, i.e. those that were not used for

¹Asterisked quantities are in the overall center-of-mass frame. Units used with $c \equiv 1$.

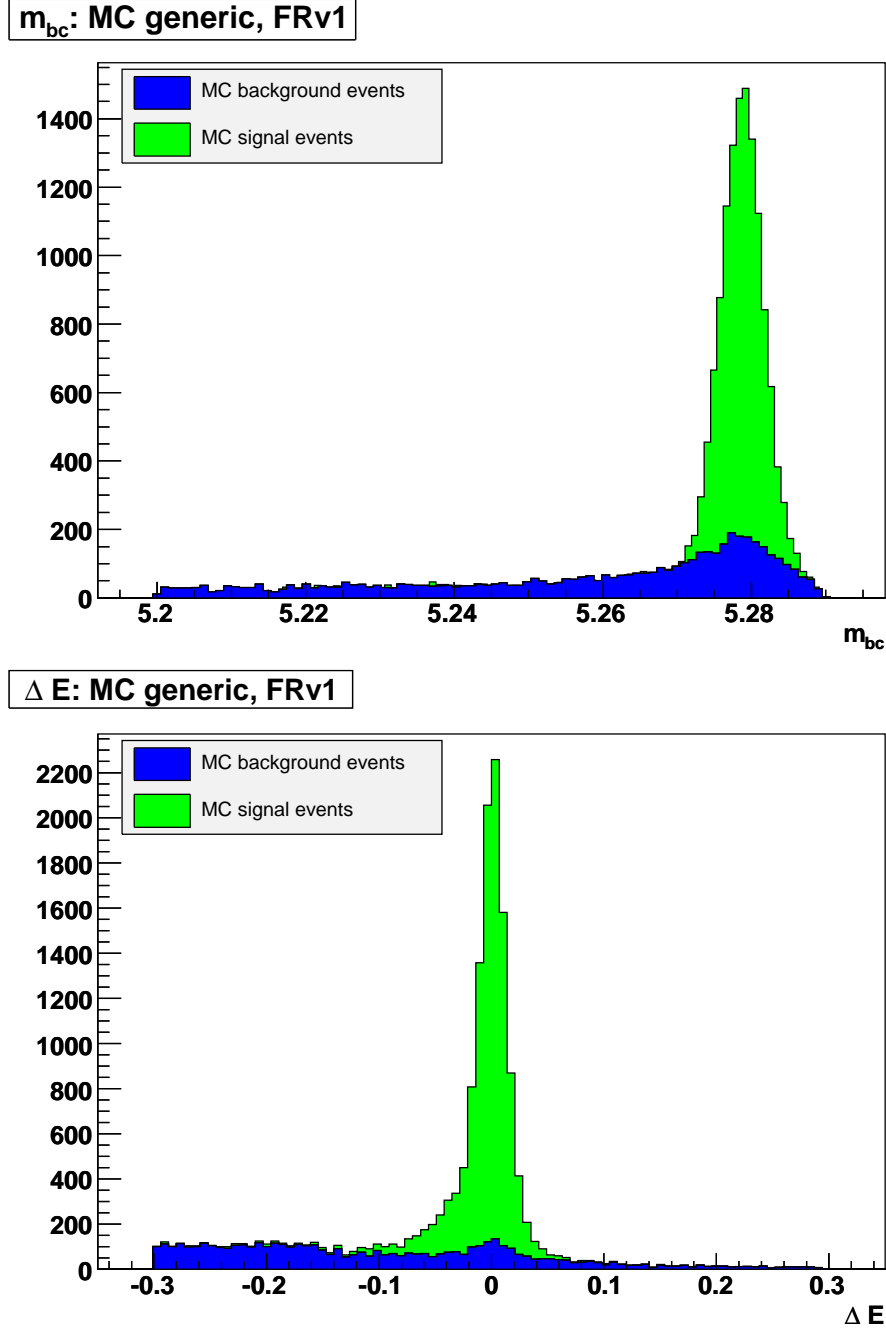


Figure 4.2: Distributions of signal and background events in the kinematic variables m_{bc} and ΔE , respectively.

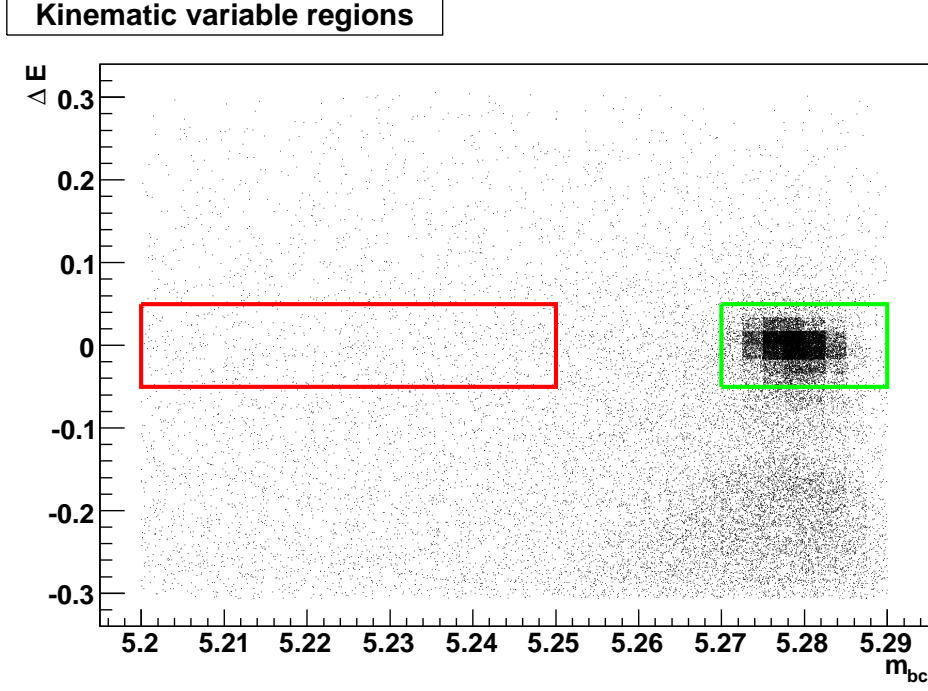


Figure 4.3: The signal region (green box) with $m_{bc} \geq 5.27 \text{ GeV}/c^2$ and $|\Delta E| < 0.05 \text{ GeV}$, and the sideband region (red box) with $m_{bc} \leq 5.25 \text{ GeV}/c^2$ and $|\Delta E| < 0.05 \text{ GeV}$.

the PR side reconstruction and not rejected by initial selection criteria, are checked for being leptons (electrons and muons). The identification criteria for an electron are given in table 4.4, those for a muon in table 4.5. For the electrons the variable `eid_prob` is used, which is a likelihood ratio that takes into account the ratio of energy detected in the ECL to the track momentum, the ECL shower shape, position matching between track and ECL cluster, the energy loss in the CDC and the response of the ACC counters. For the muons the likelihood ratio `mu_like` is used, which is based on the penetration range and the transverse scattering in the KLM detector.

The fake rate of identifying an electron as a pion is on the order of 0.1%, whereas for muons it is on the order of 1%. Both cuts ensure a particle identification probability of $> 90\%$. Furthermore, events are rejected if there is more than one remaining track identified as a lepton.

$p_{lab} > 0.3 \text{ GeV}/c$	lab frame momentum
$17^\circ < \theta < 150^\circ$	polar acceptance angle
$eid_prob > 0.5$	electron identification likelihood

Table 4.4: Electron identification criteria.

$p > 0.6 \text{ GeV}/c$	momentum cut
$25^\circ < \theta < 145^\circ$	polar acceptance angle
$mu_like > 0.9$	muon identification likelihood

Table 4.5: Muon identification criteria.

In order to achieve further significant background suppression, a cut is made on the center-of-mass momentum of the PR side primary lepton. Figure 4.4 shows the unrestrained range of the momentum, with its signal and background components stacked.

The cut has been fixed to the acceptance range of $|p_{lep}^*| > 1.1 \text{ GeV}/c$, which reduces the background events by 90.53%, while retaining 72.38% of good signal events. This is equivalent to an improvement of the signal to background ratio from 0.72 to 5.48.

4.5 Decay time reconstruction

As an ultimate goal of the whole event reconstruction process, the decay times of the two B^0 mesons have to be determined with the best possible accuracy. To visualise the situation more clearly, see figure 4.1. The B meson pair is generated from the $\Upsilon(4S)$ resonance at the primary vertex. From there the two flavor oscillating B mesons propagate in an entangled state (i.e. $B^0\bar{B}^0 \leftrightarrow \bar{B}^0B^0$), until the first one decays. Then, the remaining B meson still oscillates in flavor until it eventually also decays. If the perfect entanglement were somehow disturbed by a decoherence process, this flavor oscillation behavior would also be disturbed, thus allowing a measurement of the deviations from known quantum mechanical behavior.

The actual decay times are determined from the reconstructed vertex

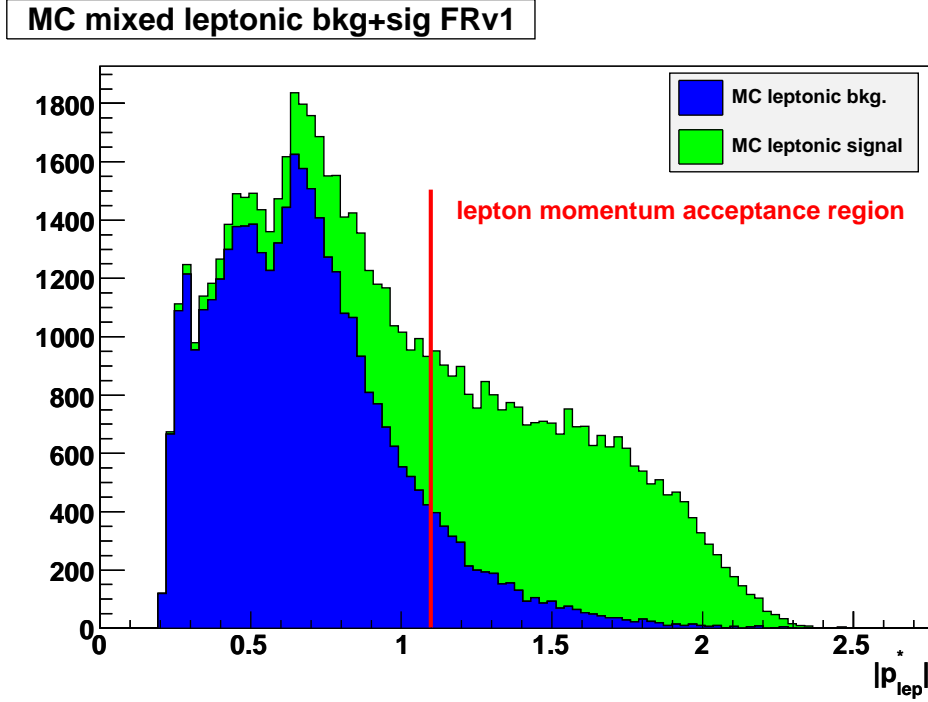


Figure 4.4: The background suppression cut on the PR side lepton in the center-of-mass system.

positions. Since the boost in the z -axis is rather big, resulting in a small opening angle of the B meson trajectories w.r.t. the z -axis, a time parameter measurement Δt can be approximated by

$$\Delta t \simeq \frac{\Delta z}{\beta \gamma c} \quad (4.1)$$

where Δz is the spatial separation between the two B decay vertices along the boost direction.

4.5.1 Vertex reconstruction

Reconstruction method

The specific event topology of the presented work made it necessary to resort to a non-standard method of vertex reconstruction. While the standard method in the Belle environment is the package `KFitter`, another package

written by K. F. Chen, **ExKFitter** [37, 38] was used.

Remembering the decay topology given in figure 4.1, the particles of special interest are the B^0 and \bar{B}^0 , together with their decay vertices. Both lack precisely measurable particle information, so that their state in a vertex fitting algorithm for the originating primary vertex (PV) is not fully defined, making them only indirectly detectable by their decay products. The package **ExKFitter** provides for such a case, and therefore was the method of choice.

Full reconstruction side vertex, and primary vertex

Since the full reconstruction module provides for a decay topology that is in most cases completely defined without any missing decay products, we call this vertex the full reconstruction vertex. The reconstruction of these two vertices is done in a co-dependent sequence. Since the positional and momentum information of the full reconstruction (FR) vertex is far better than that on the other B meson candidate, this superior information is used to effectively extrapolate backwards along the momentum vector of the FR B meson to the position of the primary vertex (PV), by intersecting this vector with the beam interaction profile (IP), at the position of the PV.

Of course this backward propagation is done not simply geometrically, but in a fitting procedure, which will be given in detail in the following steps:

1. Collect all the B meson daughter products from the full reconstruction table.
2. Remove the daughter products of possible K_S^0 particles, only leaving the K_S^0 itself.
3. Initialize the vertex fitter for the primary vertex with the information of the IP.
4. Define a vertex constraint for the FR vertex, with all the remaining B meson daughter products.
5. Define the mother B^0 particle, and link it to the FR vertex constraint.

6. Define a PV constraint and also link the mother B^0 to it.
7. Perform the full fit on the FR vertex and the PV.

This whole procedure yields two pieces of information: The position of the PV, and that of the FR vertex. For the actual vertex reconstruction of the FR side, the daughter particles of the K_S^0 mesons are removed from the fitting procedure, since they do not directly originate from the B meson decay vertex.

Partial reconstruction side vertex

The partial reconstruction vertex (PR) is the remaining vertex resulting from the decay of the second B^0 candidate. It is not as complete as the FR vertex w.r.t. its decay products. Some undetected tracks are missing in most cases, therefore the vertex position information is less accurate.

The PR vertex is reconstructed by simply using the standard reconstruction package:

1. Collect all the remaining charged particles.
2. Make a vertex constrained fit for the PR vertex with those particles.

This procedure yields the position of the PR vertex.

In order to get an impression of the spatial precision of the reconstruction process, z -axis resolutions were determined for the “core” events (i.e. events that are found in the core resolution distributions, without regarding the resolution tails). The values found are: $\approx 50\mu\text{m}$ for the z_1 position resolution of the full reconstruction vertex, and $\approx 135\mu\text{m}$ for the Δz resolution of the z -coordinate difference between the full reconstruction vertex and the partial reconstruction vertex.

4.6 Resolution functions

In order to account for the spatial (and implicitly for the time) measurement errors correctly, the MC simulation information is used, allowing to

determine the resolution functions of the model parameters t_1 and t_2 . As the whole reconstruction process is carried out, the resulting quantities are the “measured” vertex positions and therefore life times of the B mesons. Using the information of the MC generation process allows to obtain the “truth” on the involved vertices, and life times. The resolution function δt of a parameter t is then defined as $\delta t = t^{\text{MEASURED}} - t^{\text{TRUE}}$.

Since two time parameters are involved, the resulting resolution function is a two dimensional distribution of deviations of the measurements from the MC truth.

4.6.1 Problem parametrisation

The parametrization in the variables t_1 and Δt was chosen because, due to the reconstruction process, the correlation between these variables is less strong than it is for a parametrization in the “natural” decay times t_1 and t_2 . Figure 4.5 shows the corresponding plots. Strong correlations arise from the fact that in the parametrization (t_1, t_2) both times rely on the measurement of t_0 , whereas the parametrization $(t_1, \Delta t)$ is not influenced by this effect.

4.6.2 Model cuts

In order to provide for a good description of the resolution function as derived from the reconstructed spatial information, the tails in those distributions have to be very precisely accounted for. Since the tails in the resolution functions are very long, cuts on the maximum times measured were chosen as follows:

Parameter	Range
Δt	$\pm 36 \cdot \tau_{B^0}$
t_1	$\pm 18 \cdot \tau_{B^0}$

The tail suppression cuts are visualized in figure 4.6. These cuts were chosen such that approximately 98% of the events are retained.

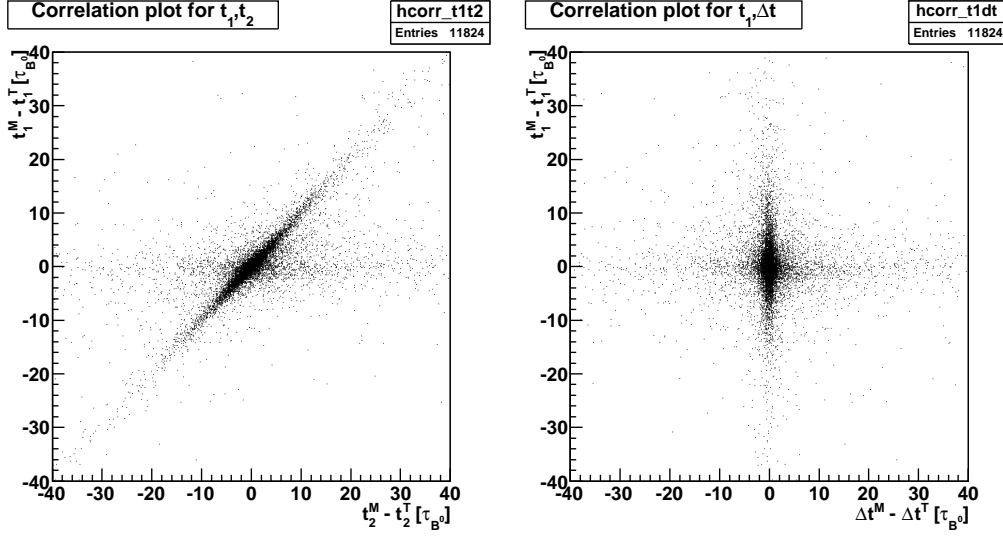


Figure 4.5: The correlations between the resolution functions in two different parametrizations. In the left plot a strong correlation between the two axes due to the dependence of both reconstructed times t_1 and t_2 on the primary vertex position can be seen, while in the right plot the correlations are very small.

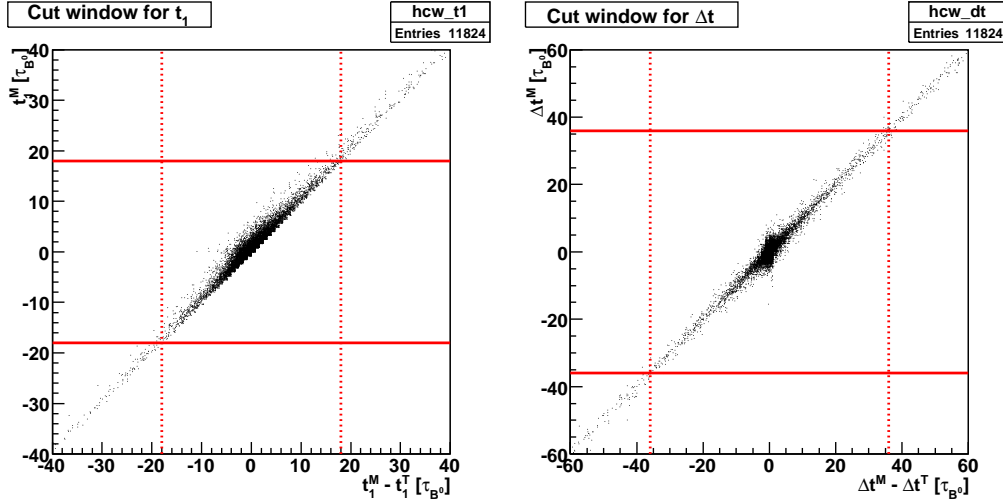


Figure 4.6: Cuts on the measured times (shown as red solid lines) result in the suppression of the very long tails in the resolution functions, and approximate to alternative cuts on the resolution parameters (shown as dashed lines).

Chapter 5

Toy Monte Carlo and fit method

For the verification of the proper function of the parameter fitting algorithm a toy Monte Carlo (toyMC) setup was created. This setup allows to study the expected resolution and correctness of the approach later used in the analysis of Belle Monte Carlo and experimental data.

5.1 Resolution functions

Because the shape of the actual p.d.f.s is dominated by an exponential shape arising from the decay of the particles under consideration (compare eqn. (2.48)), this shape is very similar to the model expression involving the exponential parameter λ (consider the two concurring exponential terms in the above equation). This circumstance made the numerical modelling of the p.d.f.s a very challenging task, requiring a lot of fine-tuning.

The expected experimental distributions were obtained by numerical convolution of the physical model with the resolution function, applying a 2-dimensional fast fourier transform convolution algorithm. This performed much better than conventional numeric convolution.

In the ToyMC the overall 2-dimensional resolution function was modeled as a product

$$R(t_1, \Delta t) = R_1(t_1) \cdot R_2(\Delta t), \quad (5.1)$$

composing the 2-dimensional resolution function out of two independent 1-dimensional resolution functions, one in each time coordinate. This seems appropriate because the choice of parameters causes a very low correlation between them. The low correlation is also visible in the correlation plots (see Figure 4.5).

Resolution function modelling

Initial attempts were made to model the resolution functions in each parameter by the sum of parametrised analytic functions, factorising the problem into two independent resolution parameters. For the purpose of testing the parameter fitting algorithm against generated toy MC events, the following parametrization of the resolution functions R in the variables t_1 and Δt has been chosen:

$$R_{2GaE}(\delta t) = C_1 \cdot e^{-\frac{1}{2}(\frac{\delta t - \mu_1}{\sigma_1})^2} + C_2 \cdot e^{-\frac{1}{2}(\frac{\delta t - \mu_2}{\sigma_2})^2} + C_3 \cdot e^{-\lambda_3 |\delta t - \mu_1|} \quad (5.2)$$

where $\delta t = t^{\text{measured}} - t^{\text{true}}$ in either t_1 or Δt . Here, the exponential term arises from the fact that the distribution that is modelled contains the difference of two exponentially distributed random variables, resulting in a “back-to-back” or double exponential shape.

The results of the fits are shown in Figure 5.1. Some deviations from the parametrized functions can be seen in the tail parts of the distributions. The agreement between this model function and the resolution function determined from signal MC is not perfect; nevertheless, it is good enough for testing the core model parameter fitting algorithm.

5.2 Event generation

The event generation for the toy MC was done by a separate event generator written in MatLab [39]. It generates data for ideal flavor correlated pairs and then adds measurement errors according to the parametrized function given in expression (5.2). In this way it is possible to test the workings of the parameter fitting algorithm under well-understood conditions.

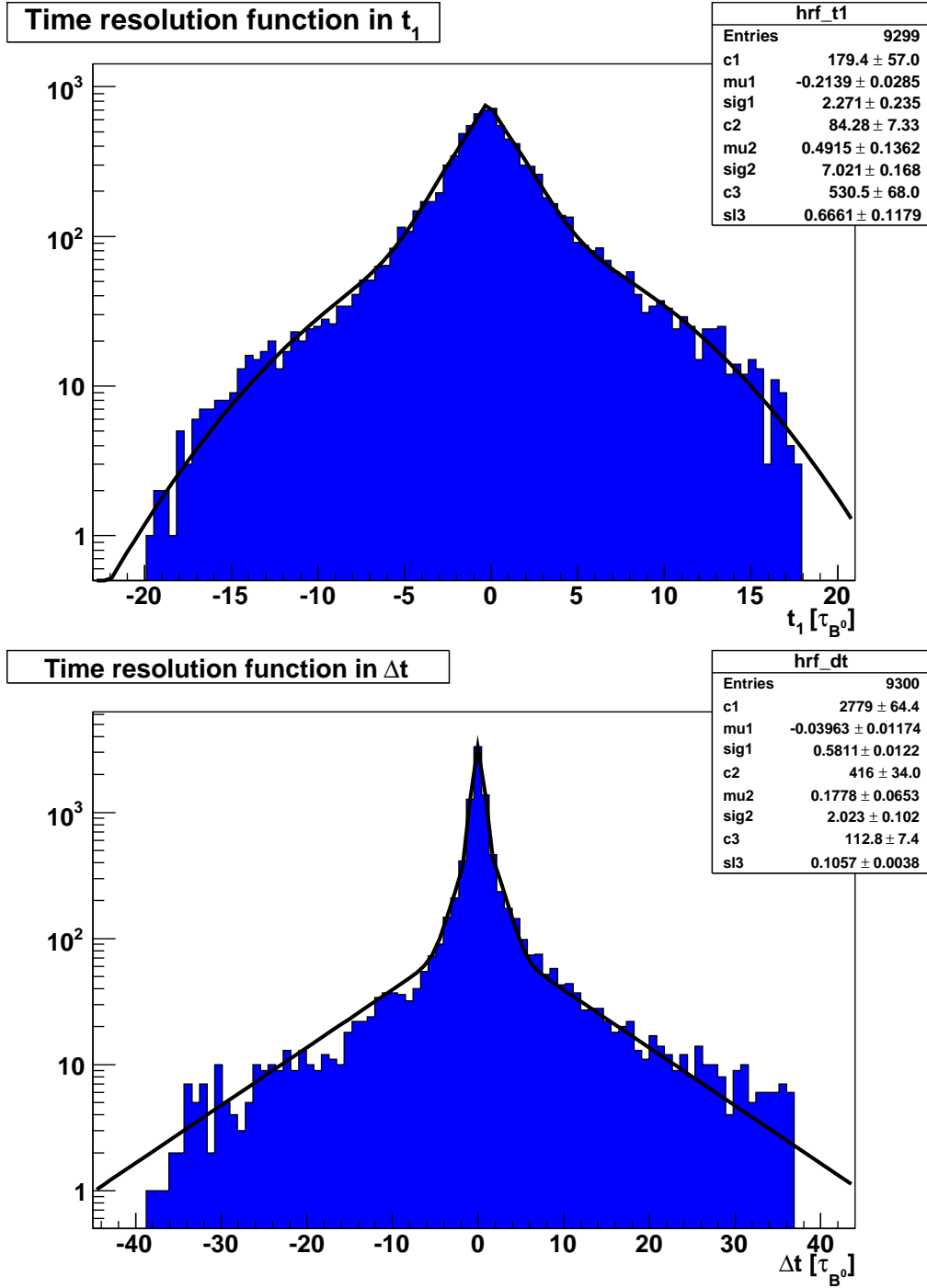


Figure 5.1: Parametrized function of eqn. (5.2) fit to the resolution functions in t_1 and Δt . The χ^2/ndf is 1.57 for t_1 and 1.72 for Δt .

The results of the tests are given later in this chapter in Section 5.4.

5.3 Maximum Likelihood estimation

To determine the actual model parameter for a given set of data, a maximum likelihood estimator is used. A short overview on the maximum likelihood method is presented in the following, as it can be found in [40].

We consider a random variable t to be distributed according to a probability density function (p.d.f.) $p(t; \lambda)$. We suppose that the functional form of $p(t; \lambda)$ is known, up to the value of the unknown parameter λ . The density $p(t; \lambda)$ represents a composite hypothesis for the distribution of t . With the method of maximum likelihood we can estimate the value of the parameter, given a finite sample of data. Supposing that the measurement of the variable t has been repeated n times, we get a set of values $\{t_1, t_2, \dots, t_n\}$. t could also represent a random vector, so that several quantities characterize an individual outcome.

The probability for a measurement to be in the interval $[t_n, t_n + dt_n]$ is $p(t_n; \lambda)dt_n$. Since the measurements are independent, the overall probability to get exactly our set of measurements $\{t_1, \dots, t_n\}$ is

$$\prod_{i=1}^n p(t_i; \lambda)dt_i$$

If the hypothesized p.d.f. and parameter value are correct, one expects a high probability for the data that were actually measured. A parameter value far away from the true value should yield a low probability for the measurements obtained. Because the dt_i do not depend on the parameter, it is reasonable to define the following function L ,

$$L(\lambda) = \prod_{i=1}^n p(t_i; \lambda) \quad (5.3)$$

which is called *likelihood function*. It is the joint p.d.f. for the t_i , but considered as a function of the parameter λ . With this motivation we define the

maximum likelihood (ML) estimator for the parameter to be the value that maximizes the likelihood function. If the likelihood function is differentiable and the maximum is not at the boundary of the admissible parameter range, the estimator is given by the solutions to

$$\frac{\partial L}{\partial \lambda} = 0.$$

The ML estimator is often obtained by maximizing the log likelihood function instead of the likelihood function:

$$\log L(\lambda) = \sum_{i=1}^n \log p(t_i; \lambda)$$

5.3.1 Properties

Under rather broad regularity conditions, the ML estimator has the following properties:

- It is asymptotically normal.
In the limit of an infinite number of measurements, the distribution of the estimator becomes a normal distribution.
- It is asymptotically unbiased.
A sequence of estimates $(\tilde{\vartheta}_n)_{n \in \mathbb{N}}$ of a quantity ϑ (n usually is the size of the sample) is called asymptotically unbiased, if:

$$\lim_{n \rightarrow \infty} E_{\vartheta}(\tilde{\vartheta}_n) = \vartheta$$

Here, E_{ϑ} is the expectation value w.r.t. to the true value ϑ .

- It is consistent.
A sequence of estimates $\tilde{\vartheta}_n$ is called consistent, if it converges in probability towards the true value ϑ

$$\tilde{\vartheta}_n \xrightarrow{P} \vartheta$$

This means: For all $\epsilon, \eta > 0$ there exists an $N(\epsilon, \eta)$ so that for all $n > N$ it is true:

$$P\left(|\tilde{\vartheta}_n - \vartheta| > \epsilon\right) < \eta$$

- It is asymptotically efficient.

We choose a random sample of size n . Then the joint probability density of all observations is:

$$g(\mathbf{x}; \vartheta) = g(x_1, \dots, x_n; \vartheta) = \prod_{i=1}^n f(x_i; \vartheta)$$

where $f(x; \vartheta)$ is the probability density of an observed feature x .

The (Fisher) information contained in a sample is defined by:

$$I_g = \mathbb{E} \left[\left(\frac{\partial \ln g}{\partial \vartheta} \right)^2 \right] = -\mathbb{E} \left[\frac{\partial^2 \ln g}{\partial \vartheta^2} \right]$$

An unbiased estimate t that satisfies the relation

$$\text{var}[t] = 1/I_g$$

is called efficient. If, for a sequence of estimators (t_n) , $\text{var}[t_n]$ converges to $1/I_{g_n}$, the sequence is called asymptotically efficient.

5.3.2 Variance

The variance of the ML estimator can be determined by different means:

1. The so called “graphical method”.

$$\log L(\lambda \pm \sigma_\lambda) = \log L_{\max} - \frac{1}{2}$$

This means that a change in the parameter λ by one standard deviation from its ML estimate leads to a decrease in the log-likelihood of 1/2 from its maximum value.

2. The derivative method.

Since asymptotic efficiency is a property of the ML estimator, we can use the Fisher-information to compute the variance of the estimator in the limit of large samples. The variance at the estimated value $\tilde{\lambda}$ then becomes:

$$\sigma_{\tilde{\lambda}}^2 \approx -1 \left/ \frac{\partial^2 \ln g}{\partial \lambda^2} \right|_{\lambda=\tilde{\lambda}}$$

5.3.3 Application

For the problem at hand we have two p.d.f.s that describe the set of experimental data. These are the p.d.f.s for same flavor (SF) and opposite flavor (OF) B meson pairs (see Eqs. (2.48)). Therefore we have two p.d.f.s, each in two time variables $(t_1, \Delta t)$: $p_{SF}(t_1, \Delta t; \lambda)$ and $p_{OF}(t_1, \Delta t; \lambda)$. Each tuple $(t_1, \Delta t)$ is accounted for in the appropriate p.d.f. (p_{SF} or p_{OF}), depending on the flavor correlation of the measurement. Note that the parameter λ is the decoherence model parameter.

Since we have to consider measurement errors in the experimental process, the resulting probability density can be given by

$$p'_i(t_1, \Delta t; \lambda) = p_i(t_1, \Delta t; \lambda) \otimes R(t_1, \Delta t) \quad (5.4)$$

where \otimes denotes the convolution operation and $i \in \{SF, OF\}$. The log-likelihood function now looks like

$$\log L(\lambda) = \sum_{k=1}^{N_{SF}} \log p'_{SF}(t_1^k, \Delta t^k; \lambda) + \sum_{k=1}^{N_{OF}} \log p'_{OF}(t_1^k, \Delta t^k; \lambda), \quad (5.5)$$

with N_{SF} and N_{OF} being the number of same and opposite flavor correlated measurements.

When adding background components, i.e. components in the measurement data that are expected not to be part of the actual signal data set, we have to modify this expression to account for these disturbing influences.

Let $p'(t_1, \Delta t; \lambda)$ be the overall p.d.f. of the measured events and $b_i(t_1, \Delta t)$

the p.d.f. of the background component i . Then the bipartite log-likelihood function is defined by

$$\begin{aligned} \log L(\lambda) = & \sum_{k=1}^{N_{SF}} \log \left\{ (1 - \sum_i w_i^{SF}) p'_{SF}(t_1^k, \Delta t^k; \lambda) + \sum_i w_i^{SF} b_i^{SF}(t_1^k, \Delta t^k) \right\} + \\ & \sum_{k=1}^{N_{OF}} \log \left\{ (1 - \sum_i w_i^{OF}) p'_{OF}(t_1^k, \Delta t^k; \lambda) + \sum_i w_i^{OF} b_i^{OF}(t_1^k, \Delta t^k) \right\} \end{aligned} \quad (5.6)$$

where the weights w_i define the influence of the component i . They can be interpreted as the probabilities that a certain event comes from a certain component of the overall distribution (be it from signal or one of the backgrounds). The term $1 - \sum w_i$ describes the remaining probability of the actual signal component, so that all weights (including the signal component) add up to 1.

For understanding the principles of the fitting algorithm, no disturbing background components were included in the toyMC setup. They were included later in the full Belle Monte Carlo tests.

Maximizing the log-likelihood functions ((5.5) and (5.6)) is done numerically by searching for the minimum value of the negative log-likelihood. The termination criterion in this search is that the calculated log-likelihood changes less than 10^{-4} in two successive search steps. With a maximum log-likelihood on the order of 10^4 this is a relative change of 10^{-8} .

The errors on the likelihood estimate are determined using the graphical method (see above), by minimizing the following expression:

$$\log L(\lambda \pm \sigma_\lambda) = \min \left\{ \left[\log L(\lambda) - \left(\log L_{\max} - \frac{1}{2} \right) \right]^2 \right\}$$

5.4 Test set results

To verify the proper functioning of the parameter fitting algorithm, several data sets have been generated and subjected to the ML fitting procedure.

Since the number of signal events in the full generic MC is around 10^4 , the same amount of $B^0\bar{B}^0$ pairs was generated in the toyMC simulation. The results of this process are shown in Figures 5.2, 5.3, and in Table 5.1.

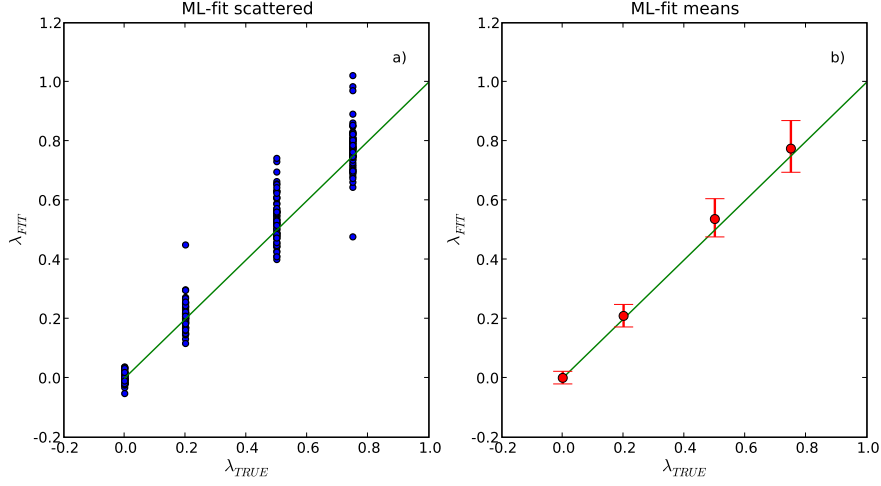


Figure 5.2: Results of multiple fits on toyMC generated data. The event sample size is 10000 $B^0\bar{B}^0$ pairs for each generated data set. The number of data sets is 64 for each given value of λ_{TRUE} . a) shows the results as scattered data. b) shows the mean values of the fitted data points with averaged asymmetric errors of all fits.

λ_{TRUE}	$\langle \lambda_{FIT} \rangle$	$\langle \sigma_- \rangle$	$\langle \sigma_+ \rangle$	σ_-^{mean}	σ_+^{mean}
0.00	0.0006	-0.0204	+0.0222	-0.0025	+0.0027
0.20	0.2099	-0.0373	+0.0388	-0.0047	+0.0049
0.50	0.5371	-0.0604	+0.0687	-0.0075	+0.0086
0.75	0.7750	-0.0800	+0.0947	-0.0100	+0.0118

Table 5.1: Results of multiple fits on toyMC generated data. The event sample size is 10000 $B^0\bar{B}^0$ pairs for each generated data set. The number of data sets is 64 for each given value of λ_{TRUE} .

Since the actual event data only consist of about 5000 $B^0\bar{B}^0$ pairs, a test toyMC test run on this sample size also has been performed. The results of this smaller sample test are shown in Figures 5.4, 5.5, and Table 5.2.

Regarding the mean measurement error, which is important when comparing a single sample estimation against its true value, both investigated

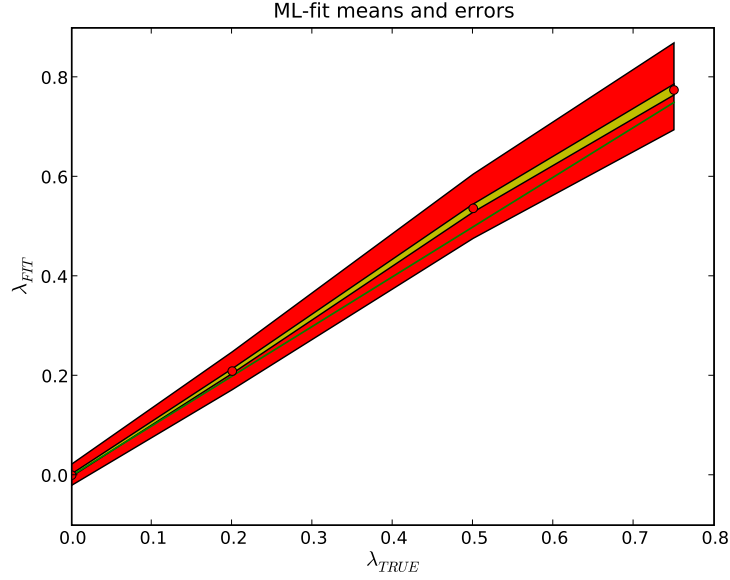


Figure 5.3: Enhanced plot of multiple fits on toyMC generated data. The event sample size is 10000 $B^0\bar{B}^0$ pairs for each generated data set. The number of data sets is 64 for each given value of λ_{TRUE} . The red band around the mean values shows the averaged errors, while the yellow band shows the errors of the mean values.

scenarios show good agreement with the statistical error margins of the fitting method.

Concerning the errors on the means of the estimates, which are shown as red bands in the figures 5.5 and 5.3, some deviations beyond the 2σ range can be seen. These deviations appear to be a bias that occurs when larger parameter values are to be estimated. It has to be stated though, that the ML estimator's property of being unbiased is only valid in the asymptotic limit, which means, that for relatively small sample sizes some biasing effects may be present.

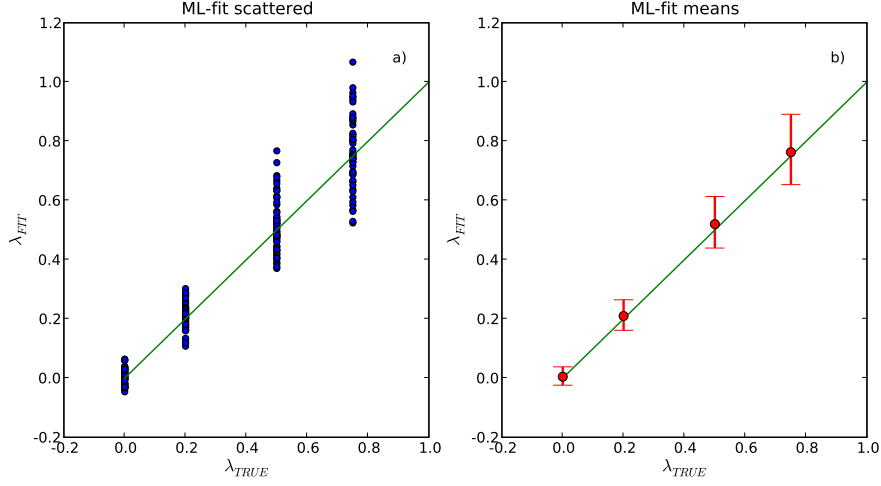


Figure 5.4: Results of multiple fits on toyMC generated data. The event sample size is 5000 $B^0\bar{B}^0$ pairs for each generated data set. The number of data sets is 50 for each given value of λ_{TRUE} . a) shows the results as scattered data. b) shows the mean values of the fitted data points with averaged asymmetric errors of all fits.

λ_{TRUE}	$\langle \lambda_{FIT} \rangle$	$\langle \sigma_- \rangle$	$\langle \sigma_+ \rangle$	σ_-^{mean}	σ_+^{mean}
0.00	0.0046	-0.0287	+0.0334	-0.0039	+0.0045
0.20	0.2097	-0.0483	+0.0548	-0.0066	+0.0075
0.50	0.5200	-0.0809	+0.0931	-0.0112	+0.0129
0.75	0.7630	-0.1097	+0.1280	-0.0158	+0.0185

Table 5.2: Results of multiple fits on toyMC generated data. The event sample size is 5000 $B^0\bar{B}^0$ pairs for each generated data set. The number of data sets is 50 for each given value of λ_{TRUE} .

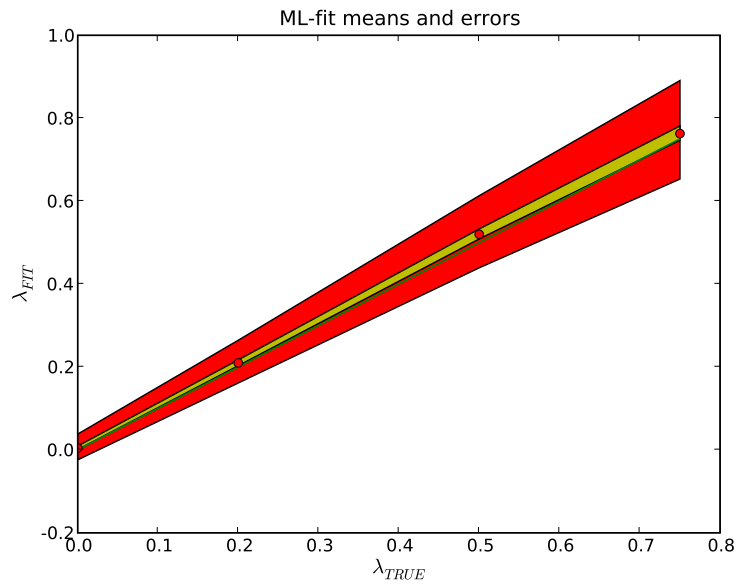


Figure 5.5: Enhanced plot of multiple fits on toyMC generated data. The event sample size is 5000 $B^0\bar{B}^0$ pairs for each generated data set. The number of data sets is 50 for each given value of λ_{TRUE} . The red band around the mean values shows the averaged errors, while the yellow band shows the errors of the mean values.

Chapter 6

Data analysis

The implementation of the decoherence model parameter fit, as it has been done for real data and full Belle-environment Monte Carlo events, will be presented in this chapter. Many different approaches to tackle this problem have been tried, which results in a number of tools that have been used.

The reconstruction of the physical events from event data was done by writing a module in the **BASF** (Belle analysis framework) [41]. Preparation of the datasets was done using the **ROOT** [42] analysis framework, which for some tasks, such as the estimation of the convolution kernel and the modelling of background components relies on the fitting package **RooFit** [43]. The toy MC verifications and the actual numerical fitting procedures were done by using the **MatLab** [39] numerical computing package.

6.1 Resolution function modelling

Since we have to include the detector response and the full setup of the Belle environment, the stochastic model of the resolution function that was used in the toy MC (see (5.2)) proved to be not sufficiently accurate for the application to signal MC and experimental data. A different approach was chosen for these cases.

Instead of using a factor model of the resolution function (see chapter 5), a total fit of the 2-dimensional resolution function was implemented. The

method that was subsequently used to smooth the complete *two-dimensional resolution function* is the KeysPDF algorithm as it is implemented in the RooFit fitting framework and documented in [44]. This non-parametric kernel estimation method models a given experimental distribution by adaptively fitting multiple Gaussian kernels to the given distribution.

The method also has a scaling parameter that allows to tune the level of detail to which its features are resolved. This parameter has been hand-tuned to a value of 0.75 and is varied later on in the process of systematic error estimation (see Section 7.3). Figure 6.1 shows the marginal distributions of the fitted two-dimensional distributions, together with the data.

The smoothed probability density is discretized on a fine grid and exported to the maximum likelihood estimator, which is implemented in MatLab. There it is used as the kernel in a numeric fast-fourier-transform convolution algorithm to derive the actual signal shape of the expected signal events.

6.2 MC event generation

The generic output of the MC physics event generator is of course a dataset that corresponds to unmodified quantum mechanics, which is equivalent to a decoherence model parameter of $\lambda = 0$.

For the sake of testing the whole decoherence model parameter estimation in the framework of the entire reconstruction chain (including the Belle framework event reconstruction), modifications had to be made to the MC event generator package **EvtGen** [34] to allow for generation of MC events that adhere to the investigated decoherence model with a parameter of $\lambda \neq 0$.

Apart from the generic MC dataset, which is produced in the course of general data processing at the Belle computing facilities, some other MC datasets have been generated with a decoherence parameter of $\lambda \neq 0$. The following Table 6.1 gives an overview on the generated sets. The large difference in the number of generated events between $\lambda = 0$ and the other two setups with $\lambda \neq 0$ arises from the following facts. First, there is quite a large number of events produced for generic MC (equal to about three times the

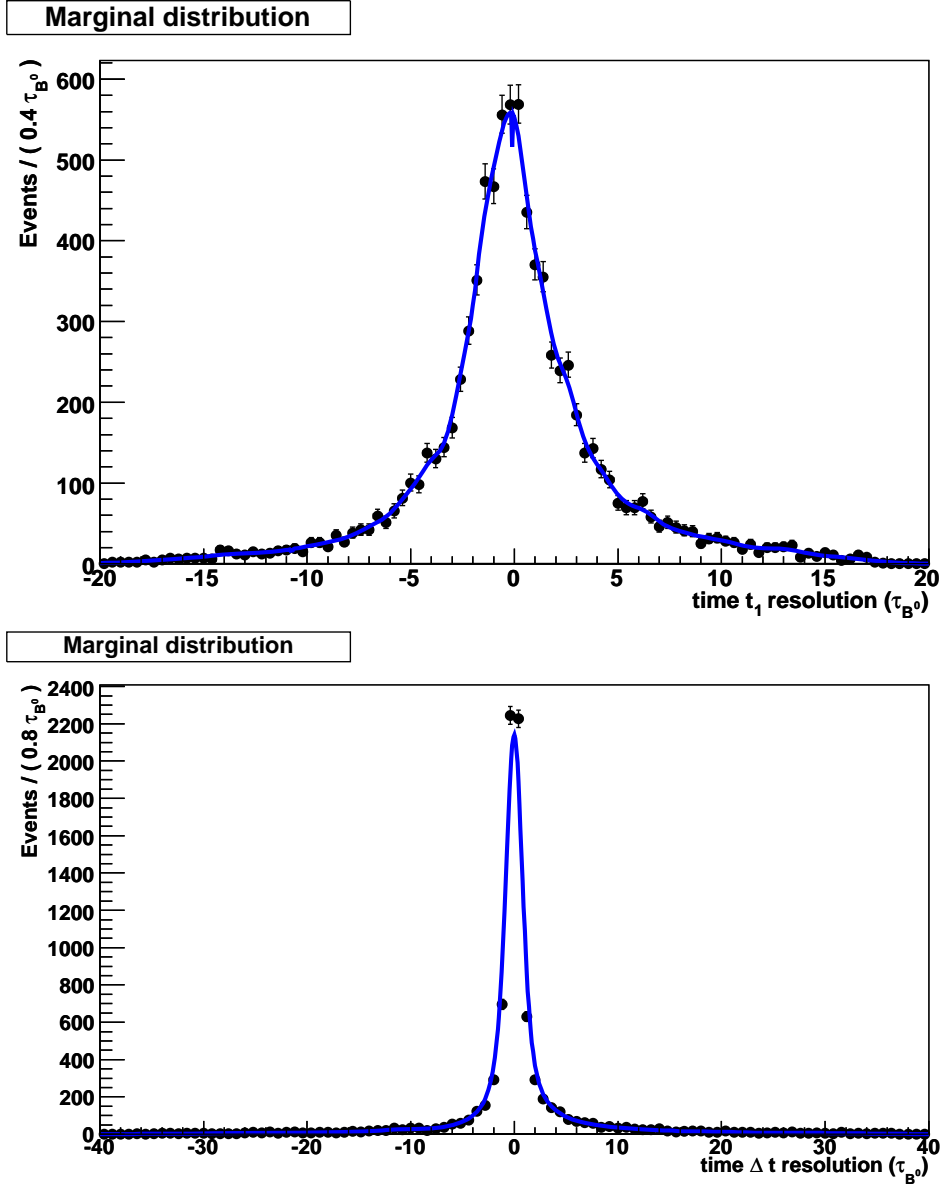


Figure 6.1: Marginal distributions of the KeysPDF fit. The data is plotted in 100 bins (= ndf). $\chi^2 = 63.626$ for the $t_1^{measured} - t_1^{true}$ distribution (upper plot) and $\chi^2 = 422.042$ for the $\Delta t^{measured} - \Delta t^{true}$ distribution (lower plot). The underestimation of the central bins in the lower plot results in the rather big χ^2 , which just causes the resolution to be estimated slightly worse than it actually is.

λ_{TRUE}	event reconstruction success	after signal cuts	source
0.00	74024	11707	generic MC
0.25	11171	4592	signal MC
0.25	21363	8801	signal MC
0.25	21492	8927	signal MC
0.25	21344	8981	signal MC
0.25	21295	8850	signal MC
0.50	10983	4562	signal MC
0.50	21314	8900	signal MC
0.50	21227	8862	signal MC
0.50	21195	8694	signal MC
0.50	21198	8688	signal MC

Table 6.1: Overview of generated signal event sets.

amount of data events). Second, the generic MC events have been generated including the B^+B^- decay channels which accounts for a factor of 2. In the smaller signal MC sets only $B^0\bar{B}^0$ events were generated, in approximately the same amount as the total expected number of data events.

6.2.1 EvtGen modifications

The concept of **EvtGen** is based on using decay amplitudes rather than probabilities for the simulation of the decays. Therefore, to understand the modifications, we have to take a closer look on the amplitudes involved in the $B^0\bar{B}^0$ decay process.

If we look at the equations (2.45) and (2.46), we have to modify the probabilities of opposite (OF') and same (SF') flavor correlation between the two B^0 mesons in such a way that our requirement of deviation from standard quantum mechanical behavior is satisfied:

$$\frac{OF' - SF'}{SF' + OF'} = A^\lambda(t_1, t_2) = A^{QM}(t_1, t_2) \cdot M(\lambda) \quad (6.1)$$

where $M(\lambda)$ can be an arbitrary modification term depending on parameter λ . For the case of the studied decoherence model we require $M(\lambda) = e^{-\lambda \cdot \min(t_1, t_2)}$. Choosing an appropriate ansatz for the underlying decay ampli-

tudes gives the desired resulting behavior for the modified asymmetry. The details on the chosen ansatz can be found in the appendix A.3.

6.3 Signal components and background influences

The set of real data as well as the generic and signal MC consists not only of signal events, but also of undesired events that result from different reconstruction mistakes and non-signal physics events. For the correct treatment of these background influences several cases have to be distinguished.

- Decay events result from the reaction $e^+e^- \rightarrow q\bar{q}$ ($q = u, d, s, c$).
No actual pair of entangled B^0 mesons has been produced. These kinds of reactions occur also below the $\Upsilon(4S)$ threshold energy, and are therefore called *off-resonance* or *continuum events* which constitute the *continuum background*.
- Decay events result from the reaction $e^+e^- \rightarrow \Upsilon(4S) \rightarrow B^0\bar{B}^0$, producing a **pair of entangled B^0 mesons**. Figure 6.2 gives an overview of the discrimination between various cases of $B^0\bar{B}^0$ background influences.
 - Everything in the reconstruction went perfect, we have an event of the *signal component*.
 - The **FR side** was **correctly reconstructed**, but the PR side has a lepton associated to it that is either wrongly identified (fake) or does not originate directly from the decay of the B meson (secondary).
 Those fake and secondary leptons result in *lepton background*.
 - The **FR side** was **not reconstructed correctly**, some tracks are missing or wrongly associated to the B decay vertex.
 This is the typical case resulting from a wrong combination of tracks for the FR vertex reconstruction. We therefore refer to such events as *combinatorial background*.

- Decay events result from the reaction $e^+e^- \rightarrow \Upsilon(4S) \rightarrow B^+B^-$.
Here also no pair of entangled B^0 mesons was produced. Only due to reconstruction mistakes on the FR-side of the decay topology has a charged B^\pm meson been identified as a B^0 . Since this is also a reconstruction mistake on the FR-side, these events are treated as *combinatorial background*.

		PR lepton	
		failure	perfect
FR tracks	failure	combinatorial	
	perfect	fake/2ndry leptons	signal

Figure 6.2: The discrimination scheme of background and signal components. The scheme discriminates between the case of a “perfect” reconstruction, where all the required tracks are found in compliance with the MC information, and the “failure” of such, meaning that some tracks were lost or associated falsely.

6.3.1 Continuum background

To determine the amount of off-resonance events, corresponding off-resonance data has been used and scaled appropriately by using the integrated luminosity, which was corrected for the difference in the $q\bar{q}$ cross section due to the continuum data being taken 60MeV below the $\Upsilon(4S)$ resonance.

The number of non-continuum events in the data sample is determined by choosing a sideband region in the beam constrained mass variable (see Figure 6.3), which is set to be the range with $m_{bc} < 5.25\text{GeV}/c^2$. Subtraction of the off resonance data events from the overall measured data events

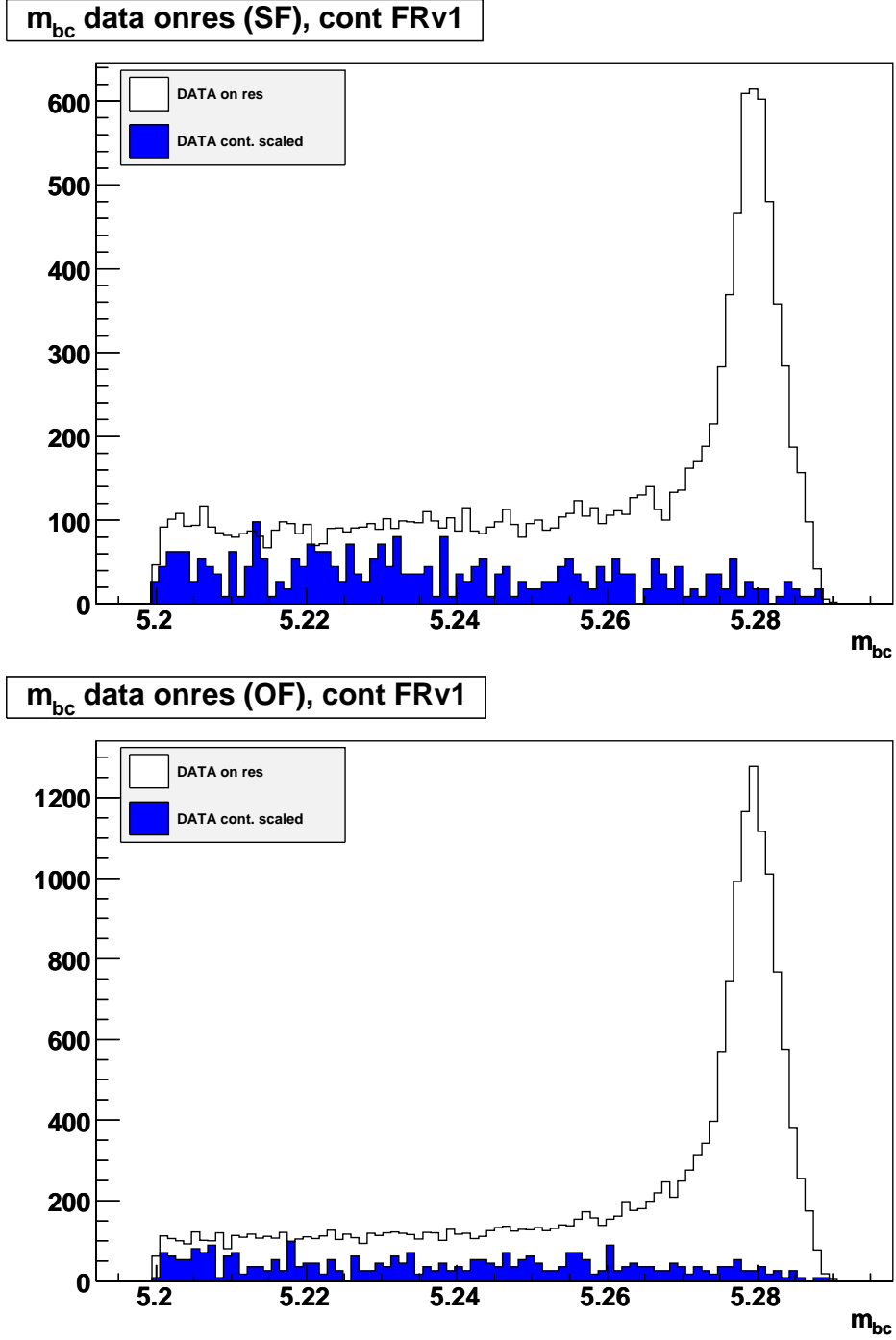


Figure 6.3: Sideband and signal region in the beam constrained mass for full reconstruction version 1 data components on-resonance and luminosity corrected continuum events. Plots are shown for same and opposite flavor correlated data. Due to the decay of the B mesons and their initial OF correlation, there are more OF correlated pairs, and the vertical axes show different scales. The sideband region used for the event counting is given by $m_{bc} < 5.25 \text{ GeV}/c^2$ (see section 4.3).

gives the number of remaining non-continuum events in the sideband region, which is subsequently used to infer further background component fractions from the MC events. This has to be done separately for each of the flavor correlations.

6.3.2 Combinatorial background

Combinatorial background is estimated from the generic MC set. It can be directly discerned from the other components by using MC generator information. Since there are much more MC events than actual data events, the proper scaling of MC relative to the amount of measurement data produced has to be accounted for. To calculate this scaling the number of non-continuum events in the data sample which has been determined before is used, because the used MC samples contain no continuum events. Figure 6.4 shows the considered MC components that correspond to the full number of expected non-continuum data events. The components are mixed ($B^0\bar{B}^0$) and charged (B^+B^-) events that have got through the whole reconstruction process. As before, the flavor correlations have to be treated separately.

6.3.3 Leptonic background and signal events

For the treatment of the leptonic and signal component an algorithm in the ROOT framework is used, which is called `TFractionFitter`. It allows fitting fractional histogram contributions to an overall histogram.

In the case at hand this method is used to fit the fractions of the various data components to the overall data distribution. This is the most direct way to relate the background and signal components derived from the different Monte Carlo sources to the actual data sample. The variable in which this fit is done is the center-of-mass momentum of the primary lepton on the partial reconstruction side. Of course the fits have to be done separately for the same and oppositely flavor correlated datasets. Figure 6.5 shows the results of the fits of four components to the data distributions.

Because the other background contributions have already been determined by other means, their fraction is fixed in the fitting process and only

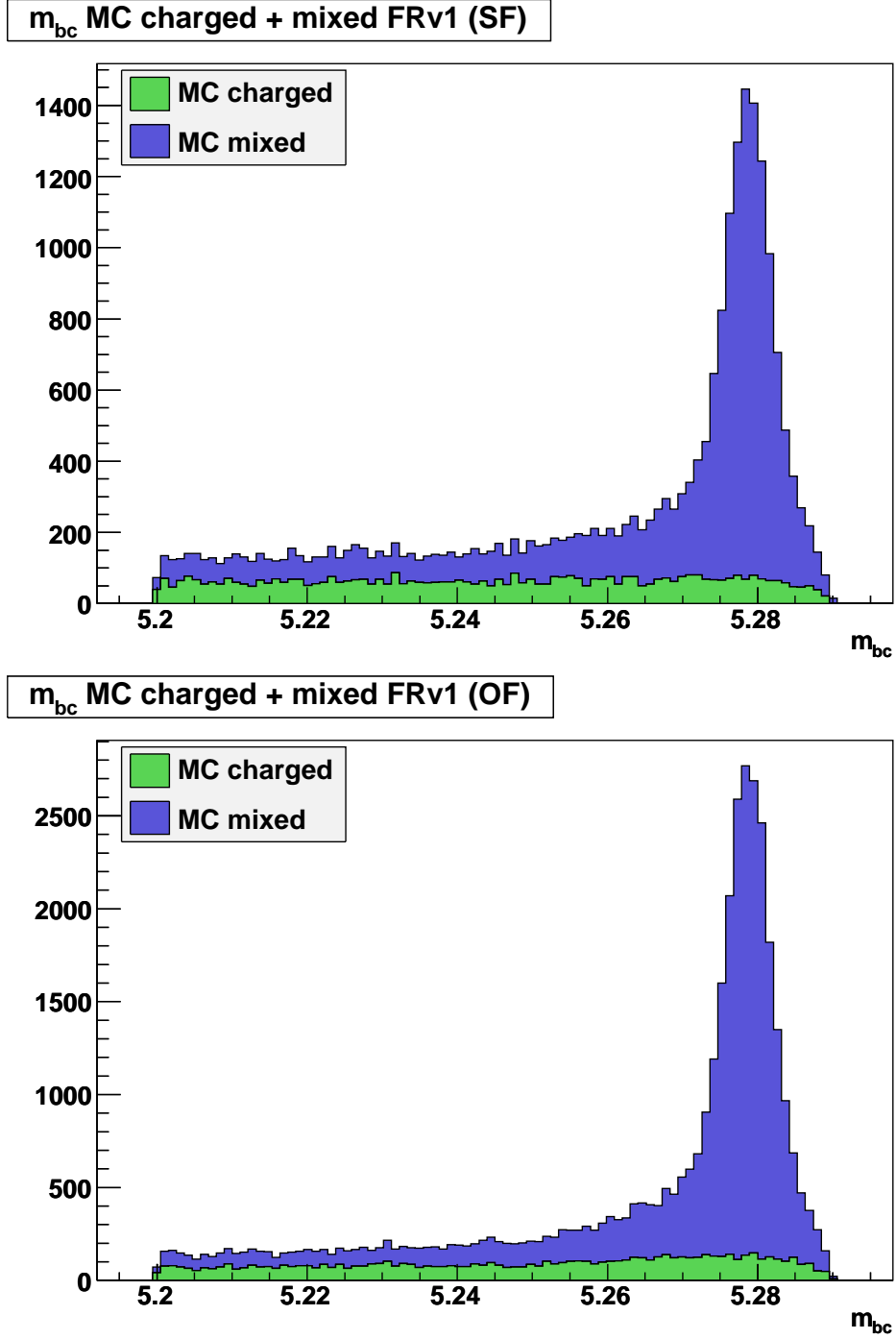


Figure 6.4: Sideband and signal region in the beam constrained mass for full reconstruction version 1 MC components. The plot shows stacked events from the mixed and charged MC set. The sideband region is used to scale the number of MC events relative to non-continuum data events. Plots are shown for same and opposite flavor correlated data. The sideband region used for the event counting is given by $m_{bc} < 5.25 \text{ GeV}/c^2$.

leptonic and signal fraction are free to be fitted.

Table 6.2 shows the results of the fraction fit. When looking at these results, it has to be mentioned that the separate sums of opposite and same flavor do not exactly add up to 100%. This is due to the fact that the fraction fitter does not include a constraint for this. Assuming independent errors for the components and adding those errors quadratically gives sufficient compatibility within statistical limits.

flavor	component	percentage	error
SF	continuum	0.752	0.005
	combinatorial	17.546	2.272
	leptonic	18.834	1.134
	signal	56.225	4.478
OF	continuum	0.456	0.003
	combinatorial	13.296	2.369
	leptonic	2.592	0.409
	signal	81.471	2.140

Table 6.2: The determined fractions of various signal components.

The two most prominent background sources, the combinatorial and leptonic background events, are fitted with the aforementioned KeysPDF algorithm, in order to calculate interpolated values for those distributions at the points of measurement. This step is required if we take a look at Eqn. (5.6), where the $b_i(t_1^k, \Delta t^k)$ correspond to the values of the background distributions at the data points.

Since the continuum background consists of very few events, it could not be treated in this way and was consequently neglected.

When looking more closely at Figure 6.5, a few remarks are to be made. The most prominent feature when comparing those two figures is the difference in the shape of the fake or secondary lepton background. While we can assume that the amount of fake lepton identifications will be approximately the same for both flavor correlations, the fraction of secondary leptons will not.

The majority of events detected will be those that exhibit an opposite

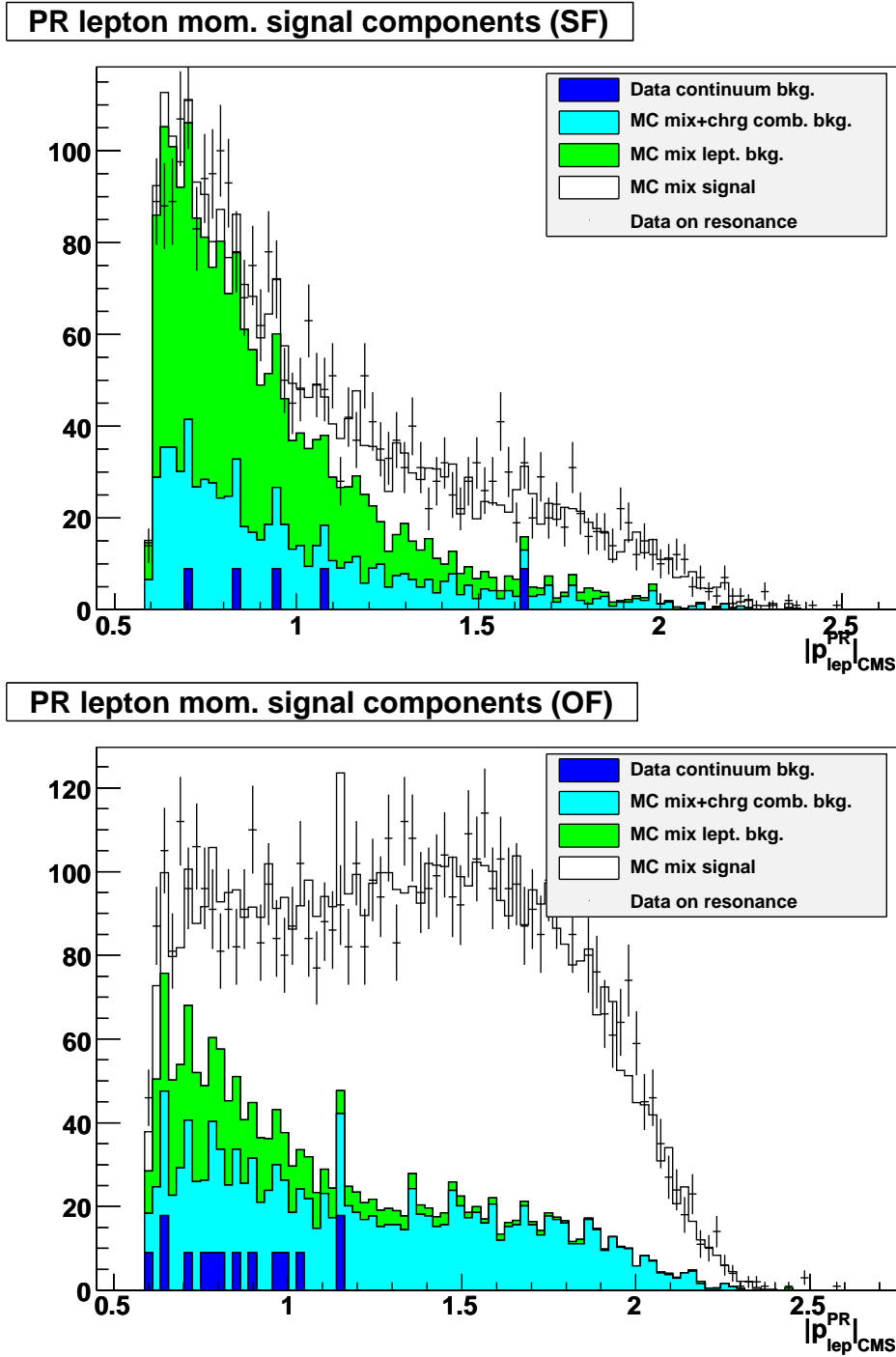


Figure 6.5: Fractional fit of signal components to the data distribution, separately done for same (SF) and opposite flavor (OF) data. The components are the continuum background taken from the off resonance data sample, the combinatorial background from MC samples of mixed ($B^0\bar{B}^0$) and charged (B^+B^-) events, the leptonic background and the true MC signal events. A feature that is apparent immediately, is the much higher leptonic background in the SF plot. The reason for this is given in the text.

flavor (OF) correlation. Only 10% of the events will have a same flavor (SF) correlation due to the lifetime limits of B^0 mesons (compare Figure 2.2).

The decay mode that is used on the partial reconstruction side to identify the flavor of the B -meson, is the prompt decay $b \rightarrow \ell^- X$ and its charge conjugate, respectively. This is how a clean signal event is being correctly identified. A corresponding decay digram is shown in Figure 6.6.

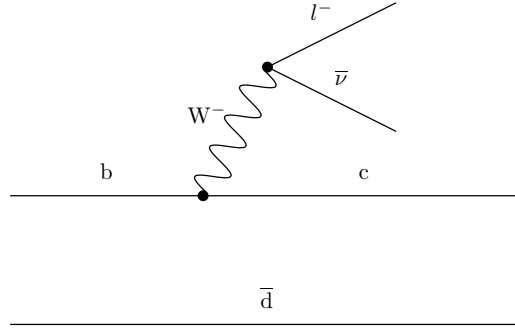


Figure 6.6: The semileptonic decay of a B^0 meson as the major mode for flavor identification on the partial reconstruction side.

Now there are mainly two things that can occur on the physical level, which will obscure the correct identification of the flavor of the partial reconstruction B^0 meson:

- A charm cascade decay occurs ($b \rightarrow cX \rightarrow \ell^+ Y$), which will flip the flavor correlation of the B -mesons (See Figure 6.7).
- An upper vertex charm cascade decay occurs ($b \rightarrow \bar{c}X \rightarrow \ell^- Y$), which will doubly flip the flavor correlations, making it correct again. Nevertheless, this case is identified as a secondary lepton on the MC level. (See Figure 6.8).

The charm cascade decay occurs about 10 times as often as the upper vertex decay, so for the case of the majority of meson pairs being OF correlated, the migration from OF to SF correlation will be 10 times as big as the double flip migration from OF to OF. Therefore a difference in the amount of secondary leptons arises.

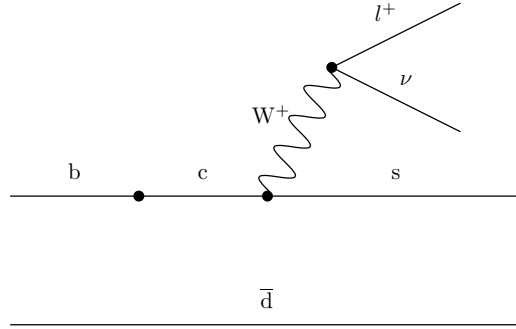


Figure 6.7: Charm cascade decay of a B^0 meson. A change in the sign of the resulting secondary lepton occurs, leading to a false flavor correlation of the B -meson pair.

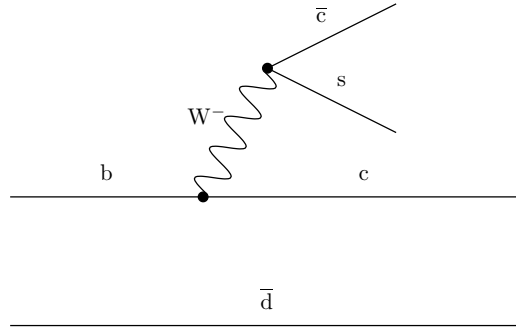


Figure 6.8: Upper vertex charm cascade decay of a B^0 meson. The sign of the lepton (resulting from $\bar{c} \rightarrow \ell^- \bar{\nu} s$) is changed twice, resulting in a secondary lepton with correct flavor correlation of the B -meson pair.

6.3.4 Other background

Investigations have shown that the only conceivable other source of background is the one that arises from the false identification of the flavor correlation between the two B mesons, which also was considered as a probable source of non-signal events. This “flavor mistagging” was examined in the MC and was found to be negligible since only 2 out of roughly 10000 events showed this deficiency.

Chapter 7

Results

7.1 Signal MC

As a first test, the ML-fitter was used to fit signal events only, without including possible background events. These fit results proved to be mostly consistent with the decoherence model parameter values used in the generation of those events. The signal sets generated can be found in the previously shown Table 6.1. Figures 7.1, 7.2 and Table 7.1 show the fit results of the generated MC sets without background components included. Looking at the errors of the mean values in Figure 7.2 and Table 7.1 suggests that there might be a biasing effect with increasing λ values.

λ_{TRUE}	$\langle \lambda_{FIT} \rangle$	$\langle \sigma_- \rangle$	$\langle \sigma_+ \rangle$	σ_-^{mean}	σ_+^{mean}
0.00	-0.0339	-0.0292	+0.0326	-0.0292	+0.0326
0.25	0.2207	-0.0558	+0.0636	-0.0250	+0.0285
0.50	0.5824	-0.0957	+0.1113	-0.0428	+0.0498

Table 7.1: Results of multiple fits on the signal-event-only MC data sets.

Regrettably, the inclusion of background components in the fit introduces a definite problem. When the maximum likelihood fitter is run with the included treatment of background components, a bias appears in the fit results. Despite extended testing and efforts to find the cause of the bias, the effect persisted. Similar effects were observed under simplified circumstances, when the normalisation of the involved probability densities was not

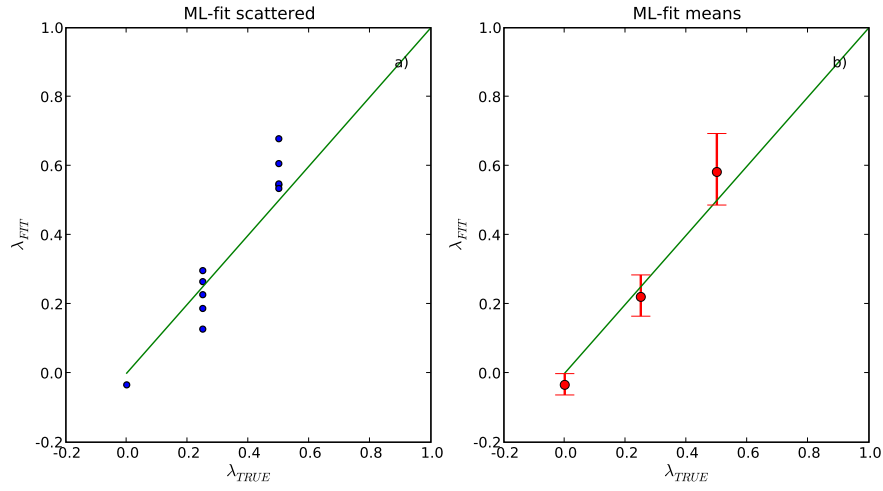


Figure 7.1: Fit results of the signal-event-only ML fit of the generated MC data sets, a) results as scattered data. b) mean values of the fitted data points with averaged asymmetric errors of all fits.

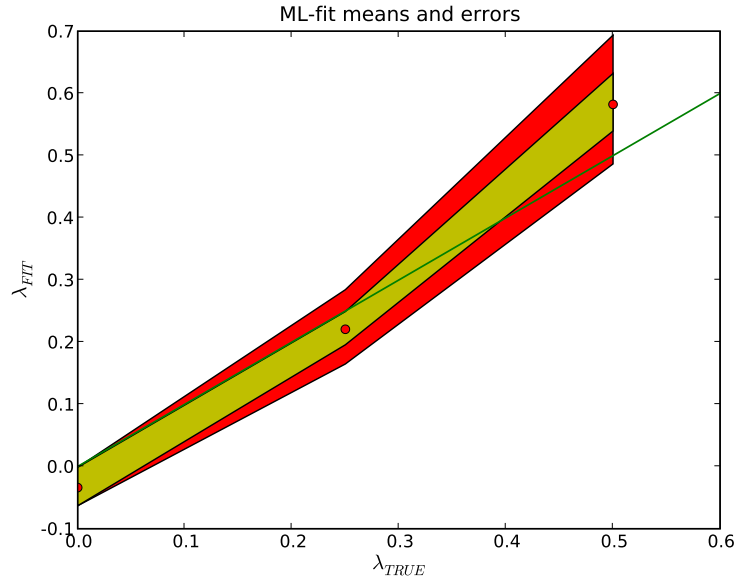


Figure 7.2: Fit results of the signal-event-only ML fit of the generated MC data sets. The red band around the mean values shows the averaged errors, while the yellow band shows the errors of the mean values.

correct. However, this has been taken care of and tested for thoroughly in the algorithm. The results of the ML-fit against the MC data samples with included background is shown in Figures 7.3, 7.4 and Table 7.2.

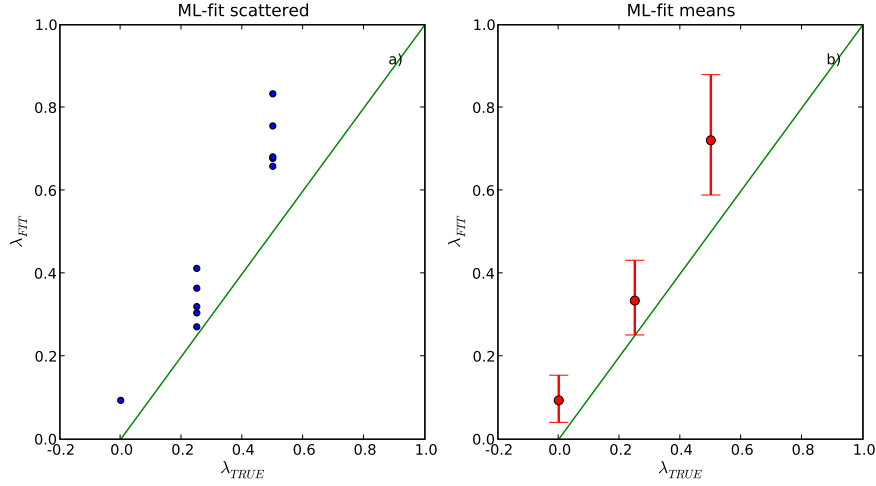


Figure 7.3: Fit results of the ML fit of the generated MC data sets, with background components included a) results as scattered data. b) mean values of the fitted data points with averaged asymmetric errors of all fits.

λ_{TRUE}	$\langle \lambda_{FIT} \rangle$	$\langle \sigma_- \rangle$	$\langle \sigma_+ \rangle$	σ_-^{mean}	σ_+^{mean}
0.00	0.0938	-0.0531	+0.0606	-0.0531	+0.0606
0.25	0.3345	-0.0829	+0.0973	-0.0371	+0.0435
0.50	0.7212	-0.1321	+0.1583	-0.0591	+0.0708

Table 7.2: Results of multiple fits on the MC data sets, with background components included.

To correct for the aforementioned bias, a line of the form

$$\lambda_{FIT} = p_1 \lambda_{TRUE} + p_0 \quad (7.1)$$

has been fitted to the data points. The fit accounts for the asymmetric errors of the individual data points. The fitted parameters are given in Table 7.3.

The fitted line is used to correct the fit results on the subsequent model parameter fit on experimental data. Figure 7.5 shows the results of the ML-fit with the bias correction.

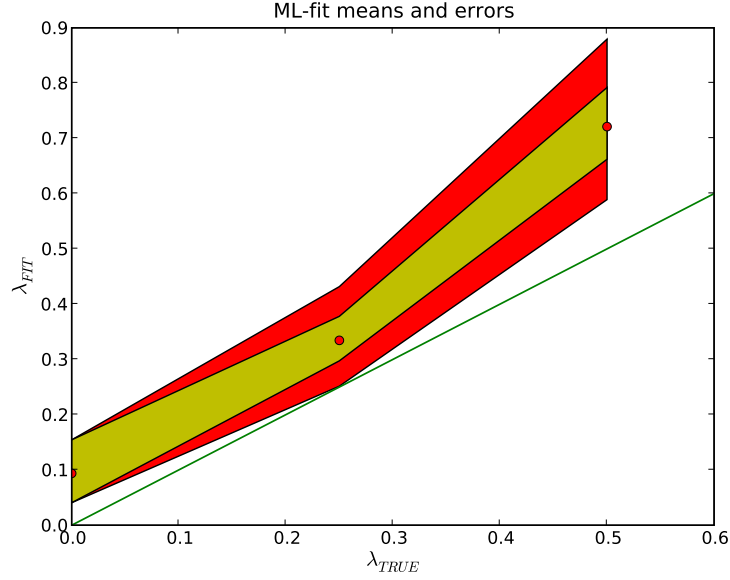


Figure 7.4: Fit results of the ML fit of the generated MC data sets, with background components included. The red band around the mean values shows the averaged errors, while the yellow band shows the errors of the mean values.

parameter	value	σ
p_0	0.06	0.05
p_1	1.23	0.17
χ^2	3.706	

Table 7.3: Line fit parameters for the bias correction.

7.2 Data fit result

Using the ML-fitter on the full data sample, with the inclusion of background component treatment, yields the following non-bias-corrected result:

$$\lambda_{FIT} = -0.006^{+0.07}_{-0.058}$$

Subsequently correcting for the bias effects leaves the final result:

$$\lambda_{FIT}^{BC} = -0.044^{+0.057}_{-0.048}$$

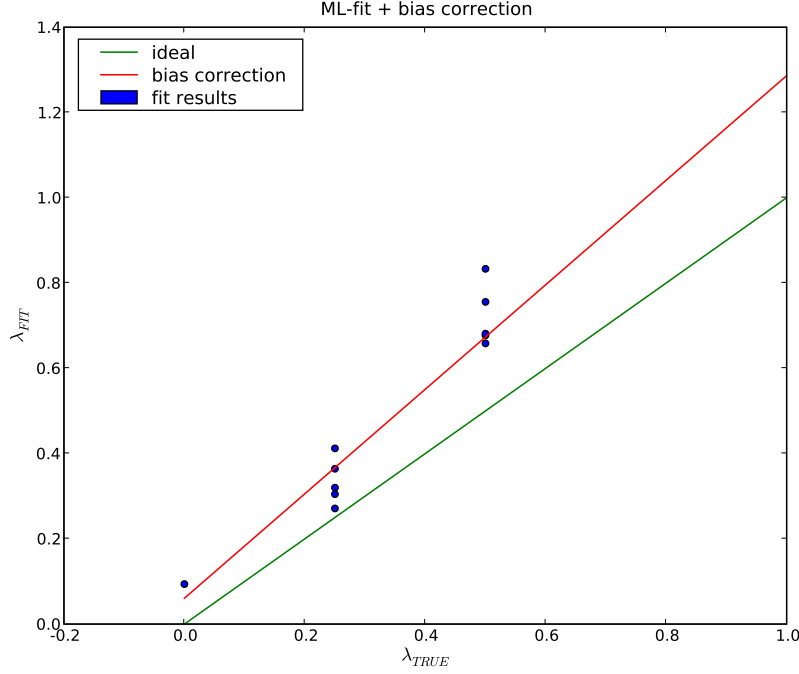


Figure 7.5: Fit results of the ML fit of the generated MC data sets, with background components included. The fit line to correct for the bias is shown in red.

7.3 Systematic errors

7.3.1 Fractional component fit

For the study of systematic errors we refer back to Table 6.2. All the given fractions except for the continuum contributions have been varied within the error margins, giving a total of 12 fit results. The following Table 7.4 shows the fit results of fraction variations.

The error for an individual component i is calculated by:

$$\sigma_{SYS}^i = (\lambda_{+\sigma}^{BC} - \lambda_{-\sigma}^{BC})/2.$$

In Table 7.5 the component-wise errors are summarised.

An estimation of the resulting systematic error has been made, by adding

flavor	component	variation	λ_{FIT}^{BC}
SF	combinatorial	-1σ	-0.0403
	combinatorial	$+1\sigma$	-0.0487
	leptonic	-1σ	-0.0355
	leptonic	$+1\sigma$	-0.0532
	signal	-1σ	-0.0596
	signal	$+1\sigma$	-0.0309
OF	combinatorial	-1σ	-0.0413
	combinatorial	$+1\sigma$	-0.0457
	leptonic	-1σ	-0.0443
	leptonic	$+1\sigma$	-0.0448
	signal	-1σ	-0.0448
	signal	$+1\sigma$	-0.0443

Table 7.4: Fit results for the variation of data fractions within the determined error margins. The last column shows the bias-corrected fit results.

flavor	component	σ_{SYS}^i
SF	combinatorial	0.0042
	leptonic	0.0088
	signal	0.0143
OF	combinatorial	0.0013
	leptonic	0.0002
	signal	0.0002

Table 7.5: Component errors of the data fractions.

the resulting component-wise errors σ_{SYS}^i quadratically, yielding

$$\sigma_{SYS}^{FFC} = 0.0174,$$

the systematic error of the fractional components fit.

7.3.2 Resolution function variation

The resolution function scaling parameter for the generation of the smoothed 2-dimensional resolution function has been varied within the reasonable range for a useful fit of its absolute value 0.75, thus yielding scaling parameters of 0.5 and 1.0. The following Table 7.6 shows the fit results.

scaling parameter	λ_{FIT}^{BC}
0.5	-0.025
1.0	-0.06

Table 7.6: Fit results for the variation of the scaling parameter for the smoothing of the resolution function. The last column shows the bias-corrected fit results.

Again assuming the difference of those two fit values to be equal to $2\sigma_{SYS}^{RF}$ gives the result:

$$\sigma_{SYS}^{RF} = 0.0175$$

7.3.3 Bias correction

To account for the errors introduced by the bias correction we consider the following. Looking at the bias correction polynomial fit coefficients, found in Table 7.3, we can see, that the correction can be roughly approximated by a tilted straight line. Because of the significant errors on those coefficients, and the errors shown in Figure 7.3, a precise calculation of error propagation will be of no real use.

Instead we will conservatively estimate the systematic contribution from the bias correction in the vicinity of the fit result ($\lambda_{FIT}^{BC} \approx 0.0$) on the event data, by setting

$$\sigma_{SYS}^{BIAS} = 0.1$$

We admit, that the procedure is not perfect, but since the biasing effects seem to get smaller towards a λ of 0, this estimation should be justified.

7.3.4 Overall systematic error

Although the systematic error is dominated by the last component, we are adding all the contributions σ_{SYS}^{FFC} , σ_{SYS}^{RF} and σ_{SYS}^{BIAS} quadratically, which yields an overall systematic error of:

$$\sigma_{SYS}^{TOT} = 0.103$$

Chapter 8

Conclusions

While a similar study [5] has only chosen a simplified model in one time parameter Δt by integrating over the other, and thus effectively averaging over one of the two axes in the two-dimensional probability density function that describes the problem correctly, the presented study was determined to employ the full mathematically correct model.

Also the estimations given for the decoherence parameter are not founded on the linear combination of the model under study and the unaltered quantum mechanical description of the problem. Instead, the full theoretical model is implemented and its decoherence parameter is estimated.

8.1 Final results

As a result for the decoherence model parameter in units of B_d^0 lifetimes we get:

$$\lambda = -0.044_{-0.048}^{+0.057} \pm 0.103$$

where the former pair of errors is of statistical and the latter is of systematic origin. For an assumed B_d^0 lifetime of $\tau_{B^0} = 1.536$ ps this corresponds to the following value in conventional units:

$$\lambda = -0.029_{-0.031}^{+0.037} \pm 0.067 \text{ ps}^{-1}$$

The result confirms, within the given errors, the hitherto existing quantum mechanical assumption of no decoherence occurring in the composite, entangled, heavy-particle B -meson system up until the point of decay of one of the mesons.

8.2 Outlook

The presented result is of course subject to possible improvements. It is the hope of the author that future studies on this topic will overcome the limitations of the work at hand.

These improvements should concentrate on future experiments with a higher spatial and consequently higher time resolution. This will result in narrower resolution functions, which provides less signal disturbance, effectively making the likelihood maximum a more distinctive feature.

Also, a new approach to the investigated matter should carefully design the fitting algorithm, thus excluding any biasing effects that regrettably occurred in the presented work. An unbiased parameter estimator will also not suffer from a rather big systematical error, since all the systematic error components are quite small except for the one resulting from the bias estimation.

Appendix A

Mathematical details

A.1 Decoherence model master equation

Starting from equation 2.30, one can insert the definition of the density matrix

$$\rho = \sum_{j,k=1}^2 \rho_{jk} |e_j\rangle \langle e_k|$$

thus getting

$$\begin{aligned} \frac{\partial}{\partial t} \sum_{j,k} \rho_{jk} |e_j\rangle \langle e_k| = & - iH \sum_{j,k} \rho_{jk} |e_j\rangle \langle e_k| + i \sum_{j,k} \rho_{jk} |e_j\rangle \langle e_k| H^\dagger - \\ & - \lambda \left[|e_1\rangle \langle e_1| \sum_{j,k} \rho_{jk} |e_j\rangle \langle e_k| e_2 \rangle \langle e_2| + \right. \\ & \left. + |e_2\rangle \langle e_2| \sum_{j,k} \rho_{jk} |e_j\rangle \langle e_k| e_1 \rangle \langle e_1| \right] \end{aligned}$$

Now going for a component-wise expression of this matrix equation yields:

$$\begin{aligned}
\dot{\rho}_{11} |e_1\rangle \langle e_1| &= -i\rho_{11}H |e_1\rangle \langle e_1| + i\rho_{11} |e_1\rangle \langle e_1| H^\dagger \\
\dot{\rho}_{22} |e_2\rangle \langle e_2| &= -i\rho_{22}H |e_2\rangle \langle e_2| + i\rho_{22} |e_2\rangle \langle e_2| H^\dagger \\
\dot{\rho}_{12} |e_1\rangle \langle e_2| &= -i\rho_{12}H |e_1\rangle \langle e_2| + i\rho_{12} |e_1\rangle \langle e_2| H^\dagger - \\
&\quad -\lambda (\rho_{12} |e_1\rangle \langle e_1| e_1\rangle \langle e_2| e_2\rangle \langle e_2|) \\
\dot{\rho}_{21} |e_2\rangle \langle e_1| &= -i\rho_{21}H |e_2\rangle \langle e_1| + i\rho_{21} |e_2\rangle \langle e_1| H^\dagger - \\
&\quad -\lambda (\rho_{21} |e_2\rangle \langle e_2| e_2\rangle \langle e_1| e_1\rangle \langle e_1|)
\end{aligned}$$

Here we can insert the Schrödinger equation of formula 2.29 and its complex conjugate to get

$$\begin{aligned}
\dot{\rho}_{11} &= -i\rho_{11}\lambda_1 + i\rho_{11}\lambda_1^* = i\rho_{11}(\lambda_1^* - \lambda_1) \\
&= i\rho_{11}(m_1 + \frac{i}{2}\Gamma_1 - m_1 + \frac{i}{2}\Gamma_1) \\
&= \rho_{11}(-\Gamma_1) \\
\dot{\rho}_{22} &= \rho_{22}(-\Gamma_2) \\
\dot{\rho}_{12} &= \rho_{12}[i(\lambda_2^* - \lambda_1) - \lambda] \\
&= \rho_{12}[-i(m_1 - m_2) - \frac{1}{2}(\Gamma_1 + \Gamma_2) - \lambda] \\
\dot{\rho}_{21} &= \rho_{21}[i(m_1 - m_2) - \frac{1}{2}(\Gamma_1 + \Gamma_2) - \lambda]
\end{aligned}$$

Solving these simple differential equations brings us to expressions 2.33.

A.2 Entangled B mesons

Eqns. 2.35 define our basis states. Applying the Hamilton operator for the bi-partite system yields:

$$\begin{aligned}
H |e_1\rangle &= H_s \otimes \mathbf{1}_2 + \mathbf{1}_1 \otimes H_s |B_H \otimes B_L\rangle = \\
&= (\lambda_H + \lambda_L) |B_H \otimes B_L\rangle = \lambda_1 |e_1\rangle \\
H |e_2\rangle &= (\lambda_L + \lambda_H) |B_L \otimes B_H\rangle = \lambda_2 |e_2\rangle
\end{aligned}$$

It is straightforward to see that we can define

$$\lambda_1 = \lambda_2 = (m_L + m_H) + \frac{i}{2}(\Gamma_L + \Gamma_H) \equiv m + i\Gamma$$

As in section A.1 we use the component-wise expression of eqn. 2.30 to get

$$\begin{aligned} \dot{\rho}_{11} &= -i\rho_{11}H|e_1\rangle\langle e_1| + i\rho_{11}|e_1\rangle\langle e_1|H^\dagger = \\ &= i\rho_{11}(\lambda_1^* - \lambda_1)|e_1\rangle\langle e_1| = \\ &= \rho_{11}(-2\Gamma) \\ \dot{\rho}_{22} &= \rho_{22}(-2\Gamma) \\ \dot{\rho}_{12} &= -i\rho_{12}H|e_1\rangle\langle e_2| + i\rho_{12}|e_1\rangle\langle e_2|H^\dagger - \lambda\rho_{12}|e_1\rangle\langle e_2| = \\ &= i\rho_{12}(\lambda_2^* - \lambda_1 - \lambda)|e_1\rangle\langle e_2| = \\ &= \rho_{12}(-2\Gamma - \lambda) \\ \dot{\rho}_{21} &= \rho_{21}(-2\Gamma - \lambda) \end{aligned}$$

Again, solving the differential equations and summarizing the expressions in one equation leads to solution 2.38.

A.3 EvtGen modifications

As mentioned before, $\Upsilon(4S)$ decays into the $B^0\bar{B}^0$ system, with the B 's being produced in a coherent state. This state evolves independently, with the oscillation frequency given by $\Delta m/2$ (Δm being $m_2 - m_1$, the mass difference between the two B mass eigenstates – see eqn. 2.4). Assuming for the physical state $|B_0^{phys}(t=0)\rangle = |B^0\rangle$, its time evolution is given by:

$$|B_0^{phys}(t)\rangle = e^{-\Gamma t/2} e^{i\bar{m}t} \left[|B^0\rangle \cos\left(\frac{\Delta mt}{2}\right) + i\frac{q}{p} |\bar{B}^0\rangle \sin\left(\frac{\Delta mt}{2}\right) \right], \quad (\text{A.1})$$

where $\bar{m} \equiv (m_1 + m_2)/2$, $q = e^{i\Phi_M}/\sqrt{2}$, and $p = e^{-i\Phi_M}/\sqrt{2}$ (Φ_M is the mixing angle).

Projecting $|B_0^{phys}(t)\rangle$ into a pure B^0 or \bar{B}^0 state, lets one obtain the amplitudes for the B decay with a given flavor. In turn, squaring them gives

the probabilities:

$$P(B_{phys}^0 \rightarrow B^0) = P(\bar{B}_{phys}^0 \rightarrow \bar{B}^0) = e^{-\Gamma t} \cos^2\left(\frac{\Delta m t}{2}\right) \quad (\text{A.2})$$

$$P(B_{phys}^0 \rightarrow \bar{B}^0) = P(\bar{B}_{phys}^0 \rightarrow B^0) = e^{-\Gamma t} \sin^2\left(\frac{\Delta m t}{2}\right) \quad (\text{A.3})$$

Now we choose a modification ansatz for the time evolution:

$$\left| B_0^{phys}(t) \right\rangle = e^{-\Gamma t/2} e^{i\bar{m}t} \left[|B^0\rangle \cos\left(\frac{\Delta m t}{2}\right)x + i\frac{q}{p} |\bar{B}^0\rangle \sin\left(\frac{\Delta m t}{2}\right)y \right], \quad (\text{A.4})$$

Calculating the resulting probabilities with this ansatz yields

$$P(B_{phys}^0 \rightarrow B^0) + P(\bar{B}_{phys}^0 \rightarrow \bar{B}^0) = 2e^{-\Gamma t} x^2 \cos^2\left(\frac{\Delta m t}{2}\right) \equiv SF' \quad (\text{A.5})$$

$$P(B_{phys}^0 \rightarrow \bar{B}^0) + P(\bar{B}_{phys}^0 \rightarrow B^0) = 2e^{-\Gamma t} y^2 \sin^2\left(\frac{\Delta m t}{2}\right) \equiv OF' \quad (\text{A.6})$$

with the sum of the appropriate probabilities defining OF' and SF' , the modified opposite and same flavor probabilities. Now looking at the asymmetry term, we get

$$\frac{OF' - SF'}{SF' + OF'} = \frac{y^2 \sin^2(\alpha) - x^2 \cos^2(\alpha)}{y^2 \sin^2(\alpha) + x^2 \cos^2(\alpha)} = \cos(2\alpha)M(\lambda), \quad (\text{A.7})$$

with $\alpha = \frac{\Delta m t}{2}$. Requiring the normalisation $y^2 \sin^2(\alpha) + x^2 \cos^2(\alpha) = 1$ gives

$$y^2 \sin^2(\alpha) - x^2 \cos^2(\alpha) = (\cos^2(\alpha) - \sin^2(\alpha))M(\lambda) \quad (\text{A.8})$$

Solving this equation by using the normalisation condition yields for the modification terms:

$$x^2 = \frac{1}{2} \left[\frac{1}{\cos^2(\alpha)} + (\tan^2(\alpha) - 1)M(\lambda) \right]$$

$$y^2 = \frac{1}{2} \left[\frac{1}{\sin^2(\alpha)} + (\tan^{-2}(\alpha) - 1)M(\lambda) \right]$$

Bibliography

- [1] J. Audretsch. *Verschränkte Systeme*. Wiley-VCH, 2005.
- [2] J. Baggott. *The meaning of quantum theory*. Oxford university press, 1992.
- [3] A. Apostolakis et al. (CPLEAR Collaboration). *Phys. Lett. A*, 119:3, 1986.
- [4] R. A. Bertlmann, W. Grimus, and B. C. Hiesmayr. Quantum mechanics, furry's hypothesis and a measure of decoherence in the \bar{K}^0 system. *Physical Review D*, 60:114032, 1999.
- [5] Apollo Go. EPR entanglement and decoherence in Upsilon(4S) decays to B^0 anti- B^0 . *Phys.Rev.Lett.*, 99:131802, 2007.
- [6] A. Go. *Journal of modern optics*, 51:991, 2004.
- [7] A. Garbarino R.A. Bertlmann, A. Bramon and B.C. Hiesmayr. *Phys. Lett A*, 332:355, 2004.
- [8] BABAR collaboration. The BABAR physics book. Technical report, Stanford linear accelerator center, Stanford university, 1998.
- [9] I. Bigi and A. Sanda. *CP violation*. Cambridge University Press, 2000.
- [10] W. Grimus G.V. Dass. Testing the Wigner - Weisskopf approximation by using neutral-meson - antimeson correlated states. *Phys.Lett. B*, 521:267–272, 2001.

- [11] W.H. Furry. Note on the quantum mechanical theory of measurement. *Phys. Rev.*, 49:393, 1936.
- [12] E. Schrödinger. Die gegenwärtige Situation der Quantenmechanik. *Naturw.*, 23:807,823,844, 1935.
- [13] W. Grimus R. A. Bertlmann. A model of decoherence of entangled beauty. *Phys. Rev. D*, 64:056004, 2001.
- [14] Reinhold A. Bertlmann. Entanglement, bell inequalities and decoherence in particle physics. *Lect. Notes Phys.*, 689:1–45, 2006.
- [15] Beatrix C. Hiesmayr. *The puzzling story of the neutral kaon system*. PhD thesis, University of Vienna, 2002.
- [16] G. Lindblad. *Comm. Math. Phys.*, 48:119, 1976.
- [17] S.L. Adler. *Phys. Lett. A*, 265:58, 2000.
- [18] Dagmar Bruß. *J. Math. Phys.*, 43:4237, 2002.
- [19] I.L. Chuang M.A. Nielsen. *Quantum computation and quantum information*. Cambridge university press, 2000.
- [20] J. P. Alexander et al. CLEO Collaboration. *Phys. Rev. Lett.*, 86:2737–2741, 2001.
- [21] The Belle Collaboration. The BELLE detector. Technical report, High Energy Accelerator Research Org. (KEK), December 2000.
- [22] A.Abashian et al. The Belle detector. *Nucl. Instrum. Meth. A*, 479:117, 2002.
- [23] V. Chabaud et al. DELPHI Collaboration. The DELPHI silicon strip microvertex detector with double sided readout. *Nucl. Instrum. Meth. A*, 368:314, 1996.
- [24] A. Abashian et al. Belle Collaboration. *Nucl. Instrum. Meth. A*, 479:117, 2002.

- [25] G. Alimonti et al. Belle Collaboration. *Nucl. Instrum. Meth. A*, 453:71, 2000.
- [26] Y. Ushiroda. *Nucl. Instrum. Meth. A*, 511:6, 2003.
- [27] T. Iijima et al. Aerogel cherenkov counter for the BELLE detector. *Nucl. Instrum. Meth. A*, 453:321, 2000.
- [28] H. Kichimi et al. The BELLE TOF system. *Nucl. Instrum. Meth. A*, 453:315, 2000.
- [29] H. Ikeda et al. A detailed test of the CsI(Tl) calorimeter for BELLE with photon beams of energy between 20-MeV and 5.4-GeV. *Nucl. Instrum. Meth. A*, 441:401, 2000.
- [30] M. Tomoto et al. Z-trigger system with the BELLE central drift chamber. *Nucl. Instrum. Meth. A*, 447:416, 2000.
- [31] S.Nishida Belle Collaboration. Trigger efficiency. Belle Note 350, 381, 423, 459, 504, 520, 548, 584, High Energy Accelerator Research Org. (KEK), 2000-2002.
- [32] M. Yamauchi S. Y. Suzuki R. Itoh BELLE Collaboration, M. Nakao and H. Fujii. Data acquisition system for the BELLE experiment. *IEEE Trans. Nucl. Sci.*, 47:5660, 2000.
- [33] <http://www.lns.cornell.edu/public/CLEO/soft/qq/>.
- [34] <http://www.slac.stanford.edu/~lange/EvtGen/>.
- [35] Torbjorn Sjostrand et al. High-energy-physics event generation with PYTHIA 6.1. *Comput. Phys. Commun.*, 135:238–259, 2001.
- [36] R. Brun, F. Bruyant, M. Maire, A. C. McPherson, and P. Zancarini. GEANT3. CERN-DD/EE/84-1.
- [37] K.F.Chen. Usage of extend kinematic fitter. Belle Note #706, High Energy Accelerator Research Org. (KEK), 2004.

- [38] K.F.Chen. The ExKFitter homepage.
<http://belle.kek.jp/~kfchen/private/ExKFitter/>.
- [39] The MathWorks Inc. MATLAB® - The Language of Technical Computing. <http://www.mathworks.com/products/matlab/>.
- [40] Glen Cowan. *Statistical Data Analysis*. Oxford University Press, 1998.
- [41] Ryosuke Itoh. Basf users's manual. Technical report, High Energy Accelerator Research Org. (KEK), 1996.
- [42] Fons Rademakers Rene Brun. ROOT, an object oriented data analysis framework. <http://root.cern.ch/>.
- [43] David Kirkby Wouter Verkerke. The RooFit toolkit for data modelling.
<http://roofit.sourceforge.net/>.
- [44] K. Cranmer. Kernel estimation in high-energy physics. *Computer Physics Communications*, 136:198–207, 2001.

Curriculum Vitae

Persönliche Daten

Dipl.-Ing. Gerald Richter

Mollardgasse 21, 1060 Wien

Geboren am 22. Oktober 1971 in Wien

Ausbildung

1978 – 1982 Volksschule der Schulbrüder Wien XV

1982 – 1990 AHS am BRG Wien VI, Marchettigasse

1993 – 2003 Diplomstudium der Technischen Physik, TU Wien

Sommer 1998 CERN Summer Student, Experimentbetreuung

2003 – 2008 Doktoratsstudium der technischen Wissenschaften, TU Wien

Sommer 2003 CERN School of Computing

Berufliche Erfahrung

1991 – 1992 datamed Informationssysteme GmbH. (nunmehr SynerGIS): Applikationserstellung in GIS "ARC-info"

1992 – 1993 ehem. Fa. Telekabel Wien: Projektfortführung

1996 ehem. Schrack-Aerospace: Programmierarbeiten

1996 – 1998 Kuffner Sternwarte Wien: Arbeit im Führungsbetrieb

1998 – 1999 Institut f. allgemeine Physik d. TU-Wien: wissenschaftliche DB-Entwicklung

1999 – 2001 tripleQ new media GmbH: CMS-Entwickler

2001 – 2002 Zivildienst; ÖHTB: EDV-Administration

2003 IT Solution GmbH: Machbarkeitsstudie im Bereich digitaler Signaturen